Institute of Physics, Polish Academy of Sciences

DOCTORAL THESIS

Influence of transition metal content on structure and thermal expansion of $Ca_{10.5-x}TM_x(VO_4)_7$ (TM=Co, Ni, Cu) orthovanadates

---

Author:
Houri Sadat RAHIMI
MOSAFER

Supervisor:
Prof. Wojciech PASZKOWICZ
Co-Supervisor:
Dr. Roman MINIKAYEV

June 2023

Abstract

This thesis presents an investigation of the structure and thermal expansion of multi-component oxides crystallizing in the whitlockite-β-$Ca_3(PO_4)_2$ structure type. Nature of these compounds offers an opportunity for wide modification of chemical compositions, allowing for the tuning of their properties through suitable substitution. Specifically, the present study focuses on three series of novel closely related compounds, $Ca_{10.5-x}TM_x(VO_4)_7$ ($0 \leq x \leq x_{lim}$), where divalent transition metals (TM = Co, Ni, Cu) are substituted into $Ca_3(VO_4)_2$. These compounds were synthesized using solid state reaction method.

Upon substituting the transition metals, a clear decrease in lattice parameters a and c as well as the unit cell volume is found, consistent with previous studies on the effect of Co, Ni, Zn, and Cu ions on the crystal structure of β-$Ca_3(PO_4)_2$. The solubility limit (x_{lim}) was determined from the $V(x)$ dependence. It is found that the M5 site is the preferred site for TMs ions, as indicated by the refined occupancy.

The structures of these compounds remain stable over a wide temperature range (4-1150 K), showing no signs of either phase transition or decomposition.

Occurrence of the axial ratio fluctuations with temperature shows that the lattice expands anisotropically. The inflection temperature (the temperature at which the slope of the axial ratio changes) at high temperature tends to decrease as the content of transition metal increases. As the content of the given transition metals increases in each series of compounds, there is a corresponding decrease in volumetric thermal expansion at room temperature, while an increase is observed at the highest studied temperature. For all the investigated $Ca_{10.5-x}TM_x(VO_4)_7$ materials, significant changes in volumetric thermal expansion occur in the vicinity of the above mentioned inflection temperature, i.e. they correlate with the change of the anisotropy character. Thermal expansion anisotropy in the studied TM substituted crystals is markedly smaller as compared to rare earth substitutions.

Optoelectronics applications can benefit from the favorable characteristic of low thermal expansion anisotropy in studied crystals. The current findings indicate a potential for reducing the expansion in crystals that have been doubly substituted with both rare earth and transition metal elements, compared to crystals containing only rare earth elements.

Streszczenie

Niniejsza rozprawa opisuje badania struktury i rozszerzalności termicznej wieloskładnikowych tlenków krystalizujących w strukturze typu whitlockite-β-Ca$_3$(PO$_4$)$_2$. Natura tych związków daje możliwość szerokiej modyfikacji składu chemicznego, co pozwala na dopasowanie ich właściwości poprzez odpowiednie podstawienie. W szczególności, obecne badania koncentrują się na trzech seriach nowych, blisko spokrewnionych związków, Ca$_{10.5-x}$TM$_x$(VO$_4$)$_7$ ($0 \leq x \leq x_{lim}$) , w których dwuwartościowe metale przejściowe (TM = Co, Ni, Cu) są podstawione do Ca$_3$(VO$_4$)$_2$. Związki te zsyntetyzowano metodą reakcji w stanie stałym. Po podstawieniu metali przejściowych zaobserwowano wyraźną redukcję parametrów sieci a i c, a także objętość komórki elementarnej. Wyniki te są spójne z wcześniejszymi badaniami nad wpływem Co, Ni, Zn i Cu na strukturę krystaliczną β-Ca$_3$(PO$_4$)$_2$. Granica rozpuszczalności (x_{lim}) została określona na podstawie zależności $V(x)$. Stwierdzono, że pozycja M5 jest preferowana dla podstawionego jonu metalu przejściowego, na co wskazuje udokładniona wartość obsadzenia. Struktury tych związków pozostają stabilne w szerokim zakresie temperatur (4-1150 K), nie wykazując oznak przejścia fazowego ani dekompozycji. Występowanie fluktuacji stosunku osiowego w funkcji temperatury pokazują, że sieć krystaliczna rozszerza się anizotropowo. Temperatura przegięcia (temperatura, w której zmienia się znak nachylenia stosunku osiowego komórki elementarnej) w wysokich temperaturach ma tendencję do zmniejszania się wraz ze wzrostem zawartości metalu przejściowego. W każdej serii związków zwiększenie zawartości metali przejściowych powoduje zmniejszenie objętościowej rozszerzalności cieplnej w temperaturze pokojowej i wzrost w najwyższej zmierzonej temperaturze. Dla wszystkich badanych materiałów Ca$_{10.5-x}$TM$_x$(VO$_4$)$_7$ znaczące zmiany objętościowej rozszerzalności cieplnej występują w pobliżu temperatury przegięcia, tzn. koreluje ona z ze zmianą kierunku anizotropii. Anizotropia rozszerzalności termicznej jest mniejsza dla przypadku podstawienia metalami przejściowymi w porównaniu do podstawienia metalami ziem rzadkich. Zastosowania optoelektroniczne mogą zyskać z powodu stwierdzonej niskiej anizotropii rozszerzalności zbadanych kryształów. Opisane wyniki sugerują możliwość zmniejszenia anizotropii poprzez podwójne podstawienie metalu ziem rzadkich i metalu przejściowego w stosunku do kryształu zawierającego jedynie metal ziem rzadkich.

Acknowledgements

I would like to express my deepest gratitude and extend my sincere appreciation to the individuals who have provided precious support and guidance throughout the course of this research project:

My supervisor, **Prof. Dr hab. Wojciech Paszkowicz** (Institute of Physics PAS, Poland) and co-supervisor, **Dr Roman Minikayev** (Institute of Physics PAS, Poland) for Their thorough guidance, valuable advice, helpful suggestions, insightful discussions, and meticulous attention to detail have significantly contributed to the success and quality of this research;

Prof. Dr hab. Marek Berkowski (Institute of Physics PAS, Poland), and **Prof. Christine Martin** (Laboratoire CRISMAT, Normandie Universite, Cean, France) for synthesizing the materials for my studies;

Dr. Mirosław Kozłowski (Tele and Radio Research Institute, Warsaw, Poland) for SEM (scanning electron microscopy) measurement and analysis;

Dr hab. Andy Fitch (European Synchrotron Radiation Facility, France) for his help in X-ray diffraction experiments at ID22 beamline;

I acknowledge the grant of the Ministry of Education and Science No. 2021/WK/11 for access to do measurement at ESRF.

Last but not least, I would like to express my heartfelt thanks to my dear Parents for their unwavering support throughout my life's journey. Your constant encouragement, belief in my abilities, and unconditional love have been the driving forces behind my achievements. I consider myself incredibly fortunate to have you both by my side.

List of Publications

[P1]   **H. S. Rahimi Mosafer**, W. Paszkowicz, R. Minikayev, M. Kozłowski, R. Diduszko, and M. Berkowski, "The crystal structure and thermal expansion of novel substitutionally disordered $Ca_{10}TM_{0.5}(VO_4)_7$ (TM= Co, Cu) orthovanadates", *Dalton Transactions* **50**, *14762-14773 (2021)* .

[P2]   J. Sánchez-Martin, D. Errandonea, **H. S. Rahimi Mosafer**, W. Paszkowicz, R. Minikayev, R. Turnbull, M. Berkowski,J. Ibáñez-Insa, C. Popescu, A. Fitch, P. Rodríguez-Hernández, "The pressure and temperature evolution of the $Ca_3V_2O_8$ crystal structure using powder X-ray diffraction", *CrystEngComm* **25**, *1240-1251 (2023)* .

[P3]   **H. S. Rahimi Mosafer**, W. Paszkowicz, R. Minikayev, C. Martin, M. Kozłowski, O. Chukova, Y. Zhydachevskyy, and S. Nedilko, "Crystal Structure, Thermal Expansion and Luminescence of $Ca_{10.5-x}Ni_x(VO_4)_7$", *Crystals* **13**, *853 (2023)* .

Contents

List of Figures

List of Tables

List of abbreviations

TCV	tricalcium vanadate - $Ca_3(VO_4)_2$
TCP	tricalcium phosphate - β-$Ca_3(PO_4)_2$
M	Cationic site
CN	Coordination number
TM	Transition metal
T	Temperature
RT	Room temperature
HT	High temperature
LT	Low temperature
T_{inf}	Inflection temperature
PXRD	Powder X-ray diffraction
SEM	Scanning electron microscopy
TEC	Thermal expansion coefficient
wt%	Weight percentage
a. u.	Arbitrary unit

Chapter 1

Introduction to $Ca_3(VO_4)_2$ family

1.1 Crystal structure

Calcium orthovanadate ($Ca_3(VO_4)_2$ - TCV[1]) is a compound that was first reported in 1965 by L. H. Brixner and P. A. Flournoy [1]. They discovered that calcium orthovanadate had a high thermal conductivity and good optical quality, making it a suitable material for use in solid-state lasers. The crystal structure of calcium orthovanadate was first described in 1973 by Gopal and Calvo. The crystal structure of $Ca_3(VO_4)_2$ is rhombohedral, Z = 21 and space group $R3c$ with unit-cell parameters $a = 10.809(1)$ Å and $c = 38.028(9)$ Å [2]. TCV has whitlockite-β-$Ca_3(PO_4)_2$ structure type. Whitlockite ($Ca_{18}(Mg, Fe)_2(PO_4)_{12}(PO_3OH)_2$) is named after an American mineralogist, Herbert Percy Whitlock.

In $Ca_3(XO_4)_2$ crystals, where X represents either P or V, a small percentage of Ca atoms can be replaced by other cations with valences ranging from +1 to +4 without affecting the overall crystal structure [3–5]. The chemical formula of the substituted compound is specific to the type of substituting cations present in the crystal. For instance, for a trivalent substituent, the formula is often written as $Ca_{10.5-1.5x}M_x(XO_4)_7$, where x can vary from 0 to 1. For a divalent substituent, the formula can be written as $Ca_{10.5-x}M_x(XO_4)_7$ or as $Ca_{3-0.286y}M_{0.286y}(XO_4)_2$; here, the solubility limit is limited , e.g. for some substituent in β-$Ca_3(PO_4)_2$ (TCP [2]), x_{lim} has been reported to be equal to one or higher [6–8].

It is worth noting that by substitutional doping in TCV crystals, the resulting structural modification involves the replacement of Ca atoms at one or more M sites with the substituting atom. This process (sharing of one site by two atoms) gives rise to the formation of a substitutionally disordered compound. This disorder can also result from the presence of structural vacancies within the crystal lattice [9].

---

[1]named also as tricalcium vanadate
[2]named also as tricalcium phosphate

In the TCV, and other whitlockite type materials, there exist five unique calcium sites, namely M1-M5. These calcium sites exhibit distinct coordination numbers (CN) with oxygen atoms, indicating their structural differences. Specifically, M1, M2, and M3 have CN of 7, 8, and 9, respectively, while M5 has a CN of 6, exhibiting a regular octahedral geometry (see Fig. 1.1). In contrast, the M4 site (CN = 3+3) has a peculiar triangular co-ordination with three identical Ca-O distances and notably longer distances to the three adjacent neighboring oxygen atoms. Furthermore, vanadium atoms occupy three crys-tallographic sites, V1-V3, with tetrahedral coordination. All vanadium atoms coordinate with four oxygen atoms [2] (similar structure reported for TCP family [10, 11]).
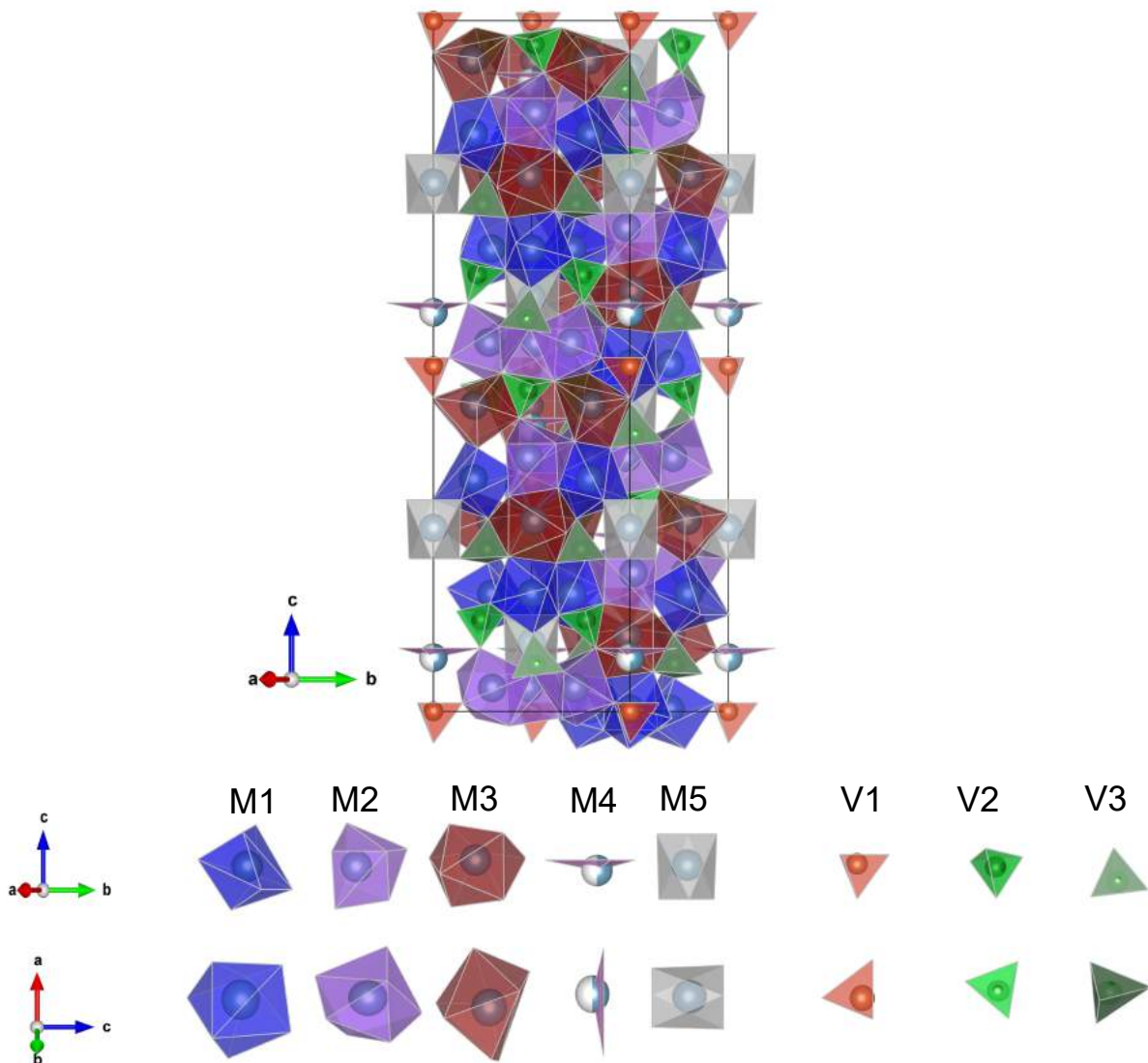
Figure 1.1: Ca-based polyhedra in the Ca$_3$(VO$_4$)$_2$ structure, presented along different axes of a unit cell. In the corners of each polyhedron, oxygen ions are present.

The intricate arrangement of this structure can be explained by its composition of only two fundamental building units - columns A and B. Each A column is positioned within a cluster of six B columns [7]. The A column has a specific sequence of sites: $V1O_4 - M4O_6 - M5O_6 - V1O_4$. On the other hand, the corresponding sequence for column B is $V3O_4 - M1O_7 - M3O_8 - M2O_8 - V2O_4$ (see Fig. 1.2). Within the A column, the atomic coordinates of M4, M5, and V1 sites have zero values for both x and y. On the contrary, in the B column, the x and y atomic coordinates of M1, M2, M3, V2, and V3 sites reveal a more distorted path.
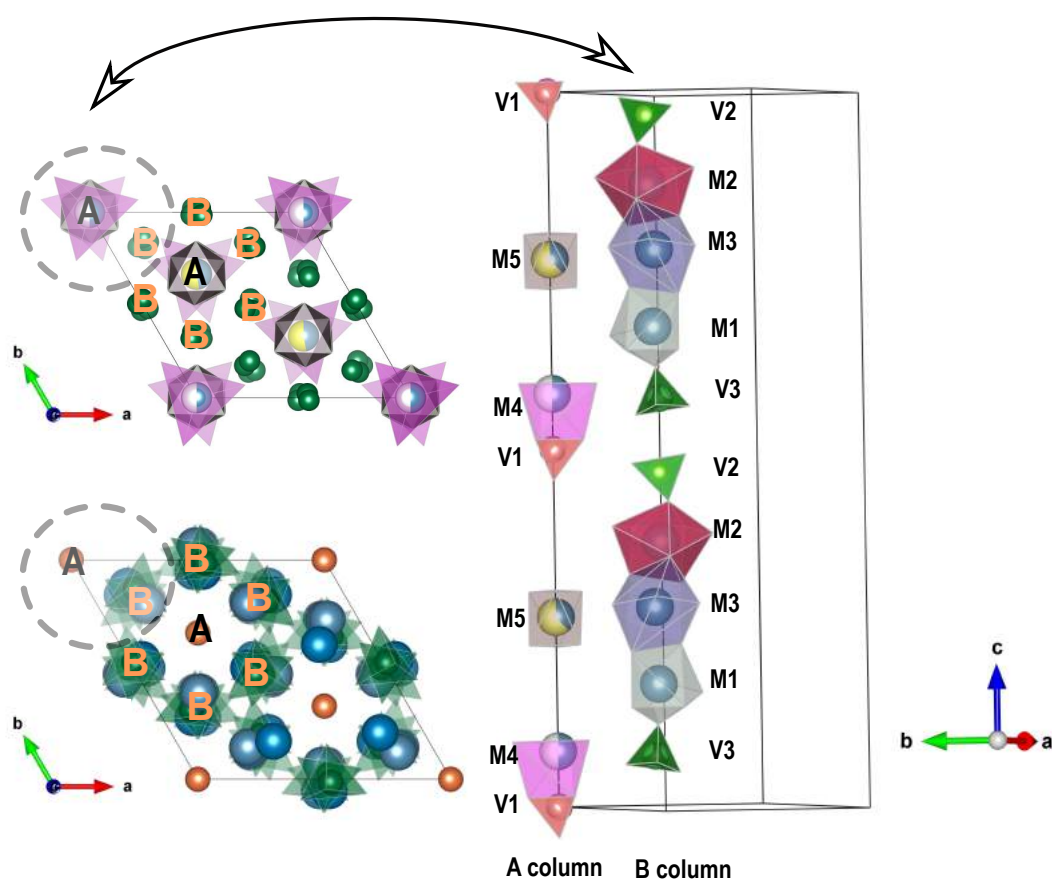
Figure 1.2: Two *ab*-projections of the TCV unit cell (left) highlighting the A and B columns along *c* axis that are shown on the right. The orange circles represent the vanadium centered V1, and the green circles represent V2, and V3 sites, and the blue circles show the calcium-centered polyhedra located at the M1-M5 sites. The M4 site is half empty (so represented by half empty symbol), and the blue colored half of it represents occupation by Ca ions. The blue and yellow colors represent Ni, respectively, at the fully occupied M5 site.[P3]

1.2 Application

$Ca_3(VO_4)_7$ is a material that has been found to be potentially useful for various applications when substituted with transition metals and rare earth elements. In 1965, a breakthrough was achieved when $Ca_3(VO_4)_7 : Nd^{3+}, Sm^{3+}, Eu^{3+}, Tb^{3+}, Dy^{3+}$ was synthesized using the Czochralski method, and subsequently named as a new laser host crystal [1]. The nonlinear optical behavior of this material and its second harmonic generation features have received significant attention due to their potential applications in various laser apparatus. A comprehensive study on the nonlinear behavior of $Ca_3(VO_4)_7$ was conducted by Bechthold et al., who considered *R3c* as the appropriate space group [12]. This discovery contrasted with the earlier belief that the material exhibited monoclinic symmetry [1].

Recent research has explored into a group of whitlockite type orthovanadates that can be substituted with rare earth ions, specifically $Ca_9RE(VO_4)_7$. These materials have attracted interest due to their strong nonlinear frequency doubling effect and unique crystal structure, which is listed below:

- Nd^{3+} doped:
    - $Ca_3(VO_4)_2 : Nd^{3+}$ [13]
    - $Ca_{9.03}Na_{1.08}La_{0.62}(VO_4)_7 : Nd^{3+}$ [14]
    - $Ca_9Gd(VO_4)_7 : Nd^{3+}$ [15]
    - $Ca_{2.85}Gd_{0.1}(VO_4)_7 : Nd^{3+}$ [16]
    - $Ca_9Y(VO_4)_7 : Nd^{3+}$ [17]
    - $Ca_{10}(Li/K)(VO_4)_7 : Nd^{3+}$ [18]
    - $Ca_9Y_{0.5}La_{0.5}(VO_4)_7 : Nd^{3+}$ [19]
    - $Ca_9La(VO_4)_7 : Nd^{3+}$ [20]
    - $Ca_{10}Li(VO_4)_7 : Nd^{3+}$ [21]
- Tm^{3+} doped:
    - $Ca_9La(VO_4)_7 : Tm^{3+}$ [22]
    - $Ca_3(VO4)_2 : Tm^{3+}$ [23]
    - $Ca_3(VO4)_2 : Tm^{3+}/Ho^{3+}$ [24]

- Er^{3+}

    - $Ca_9La(VO_4)_7 : Er^{3+}$ [25]
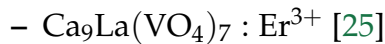
White light-emitting diodes (wLEDs) are a promising lighting technology of the new generation, characterized by exceptional performance features such as high luminescent efficiency, extended operational lifetime, and environmental sustainability. In recent years, considerable research efforts have been focused on exploring the use of novel materials for wLEDs, and among them, calcium orthovandates $(Ca_3(VO_4)_7)$ doped with rare earth or codoped with rare earth and divalent ions have emerged as a promising class of materials for this purpose; some examples are listed below:

- $Ca_9Y_{0.95}Ln_{0.05}(VO_4)_7(Ln^{3+} = Eu^{3+}, Sm^{3+}, Pr^{3+})$ [26]

- $Ca_9Dy(VO_4)_7$ [27]

- $Ca_9Y(VO_4)_7 : Eu^{3+}, Bi^{3+}$ [28]

- $Ca_9R(VO_4)_7 : Eu^{3+}(R = Bi, La, Gd, Y)$ [29]

- $Ca_9Eu_{1-x}Ln_x(VO_4)_7(Ln = Y, La, Gd, Lu)$ [30]

- $Ca_9La(VO_4)_7 : 0.01Eu^{3+}, 0.02Mg^{2+}$ [31]

- $Ca_9La(VO_4)_7 : 0.02Sm^{3+}, 0.02Li^{+}$ [32]

- $Ca_9Eu(VO_4)_7$ [33] [34]

Pogosova et al. [35] have published a unique paper on the application of transition metals in calcium orthovanadates. The authors explored the potential of $Ca_{3-1.5x-y}Eu_xCu_y(VO_4)_2$ materials doped with Europium and copper as inorganic yellow pigments. These findings demonstrate the versatility of calcium orthovanadates in meeting diverse industrial needs, particularly in the field of pigments.

Calcium orthovanadates and orthophosphates have closely related structure and properties.The Reader can find information about the structure and application of TCP substituted by trivalent ions in Refs. [36–41].

1.3   Non-ambient condition

The physical and chemical properties of materials are not only influenced by their chemical composition and crystalline architecture, but also by external factors such as temperature changes. Understanding the mechanisms that contribute to these properties is

essential when considering changes in materials with temperature. The thermal properties of any material are related to the vibrations of its atoms around their equilibrium positions in a crystal lattice, with the amplitude of these vibrations increasing by temperature. One way to study the properties of materials at variable temperatures is through X-ray diffraction. This technique involves the use of X-rays to determine the structure of crystals [42].

Studying polycrystalline materials at variable temperatures opens up new frontiers in the investigation of the physical and chemical properties of materials. This extended knowledge can be used to obtain a more comprehensive picture of the phase diagram of a compound and more precise information on some properties of a material. For instance, the behavior of a material under different temperatures can provide information on its thermal conductivity, coefficient of thermal expansion, and melting point. Additionally, the behavior of materials at low temperatures is of interest in fields such as superconductivity, where the electrical resistance of a material drops to zero at low temperatures. This phenomenon is related to the changes in the electronic and magnetic properties of the material that occur as temperature decreases [43].

1.3.1   Low temperature

In the field of low temperature crystallography, reducing the temperature of a crystalline sample has a significant effect on reducing lattice vibrations, resulting in decreased atomic displacements and increased Bragg scattering, ultimately improving the data quality. However, definition of "low" temperature depends on the specific material being studied [42, 44].

Low temperature X-ray diffraction has diverse applications, including the study of correlations between crystal structure and properties such as:

- phase transtion and thermal expansion coefficient

- charge density analysis

- study material which are liquid or gases at room temperature

Studying the effect of temperature on crystal lattices is crucial in developing materials for practical applications. For example, in nonlinear optical materials, high-energy laser radiation can cause thermal gradients within the crystal, which can lead to damage. In these cases, it is necessary to assess changes in unit cell parameters with temperature, as well as sample stress that can cause fractures [42, 44].

Negative thermal expansion materials, which expand as temperature decreases, are of great interest to researchers. These materials can be used to produce composites with a net zero coefficient of expansion over a broad temperature range, such as optical mirrors, fiber optics, and cookware. They can also be used to manufacture materials with tailored expansion coefficients that match those of other materials, which is critical in electronic and biomedical applications [42, 44].

To date, no report has been made regarding the investigation of the behavior of TCV family at low temperatures using X-ray diffraction.

1.3.2 High temperature

High-temperature X-ray diffraction is a powerful technique that enables the study of crystal structures at elevated temperatures. This technique is exploited in materials science, chemistry, and physics. In solid-state lasers, high-temperature X-ray crystallography is particularly useful in understanding the thermal effects that can limit the performance of the lasers [18, 45].

The thermal expansion coefficient (TEC) is an important parameter for materials that are used in high-temperature applications; for instance, in the case of crystal cracking during the growth, annealing [18]. The TEC has been studied for several calcium orthovanadate materials, including $Ca_9Y(VO_4)_7$ [18], $Ca_{9.33}K_{2.33}(VO_4)_7$ [46], $Ca_9Nd(VO_4)_7$ and $Ca_{10}K(VO_4)_7$ [47], using dilatometric methods. The volumetric thermal expansion values for these materials are in the range of $33.5 - 48$ MK^{-1} between $295 - 810$ K.

High-temperature X-ray diffraction has also been used to study phase transitions in materials. In particular, discontinuity in variation of lattice parameter with temperature has been observed in some calcium orthophosphate materials doped with rare earth elements, indicating a phase transition to *R*-3*c* space group [48, 49]. Second harmonic generation (SGH) and dielectric properties studies have been used to confirm phase transitions at high temperatures for $Ca_9In(PO_4)_7$ [50] and $Ca_8MgR(PO_4)_7(R = Pr, Tb, Lu)$ [51].

Up to now, there is no available report on the use of X-ray diffraction to investigate the behavior of calcium orthovanadates substituted with transition metals at high temperatures.

1.4   Aim of dissertation

According to the survey in sections 1.1, 1.2, and 1.3, previous studies on calcium ortho-vanadate materials have mainly focused on rare earth substitution into TCV and their applications.

Only a limited number of studies have been reported on the substitution of mono-valent and divalent ions in TCVs, but interest in these materials is growing. For example, the structure of $Ca_{10}K(VO_4)_7$ was analyzed in 1996 [52], while the structure of $Ca_{10}Li(VO_4)_7$, synthesized via the Czochralski method, was later investigated [21]. Raman spectra of $Ca_{10}Na(VO_4)_7$ were also reported, but without accompanying structural information [53]. More recently, high-temperature diffusion was utilized to prepare Mn-doped $Ca_3(VO_4)_2$ single crystals [54]. Furthermore, the effect of cobalt doping in $Ca_3(VO_4)_2$ single crystals was investigated using X-ray diffraction and X-ray absorption spectroscopy [55].

The knowledge of crystal structure is the first step for design and understanding the application of this materials.

The dissertation aims to provide comprehensive structural data for a series of cobalt, nickel, and copper ion substituted into TCV to understand if the structure is remain at *R3c* space group and what is maximum percentage of transition metal which can introduce to this structure. On the other hand, structure stability are become of curiosity to check if there is any phase transition at high and low temperature and what is the behavior of thermal expansion coefficient of this materials. These study fills the knowledge gap in the TCV group.

To achieve this, the following steps were taken:

- The X-ray diffraction (XRD) technique was used to conduct phase analysis and structure refinement. The investigation of the materials was predominantly carried out using powder XRD.

- Structure refinements for powder XRD were performed by the means of the Rietveld method.

- A series of high-temperature and low-temperature experiments were conducted using laboratory and synchrotron techniques on selected samples.

- The thermal expansion coefficients of several compounds in this series were determined.

- the Debye temperature (θ_D) was estimated for the selected compounds, providing insights into the order of magnitude of the Debye temperature for each compound. This information is valuable in understanding the vibrational properties and thermal behavior of the studied materials.

Chapter 2

Characterization technique

This chapter describes experimental techniques and apparatuses that are used to characterize whitlockite type material in this thesis.

2.1 The principles of X-ray diffraction

The basic of X-ray diffraction can be found in many textbooks for instance [56–59]. Diffraction is a phenomenon that occurs when electromagnetic radiation interacts with periodic structures that have geometrical variations on the length scale of the radiation wavelength. In crystals and molecules, the interatomic distances are typically between 1.5 and 4 Å which corresponds to X-rays with photon energies between 3 and 8 keV in the electromagnetic spectrum. When X-rays are directed at crystalline and molecular structures, phenomena such as constructive and destructive interference occur.

Thomson scattering, also known as classical scattering, is one of the three types of interaction of X-rays with matter in the relevant energy range, the other two being photoionization and Compton scattering. In Thomson scattering, the incident X-ray interacts with an electron in the target material, causing the electron to oscillate at the frequency of the incoming beam and become a source of radiation. The scattered X-ray has the same energy and wavelength as the incident X-ray, making it an elastic scattering process. Unlike photoionization and Compton scattering, Thomson scattering does not result in the ionization of the target atom. X-ray diffraction relies on the Thomson component in the scattering of X-rays to generate a diffraction pattern that can be used to determine the arrangement of atoms in the crystal.

When an X-ray beam interacts with a solid material, the electrons of the atoms in the material scatter some of the X-ray waves in different directions. However, not all diffracted waves are observable due to destructive interference.

In simple terms, Bragg's law states that when X-rays with a specific wavelength, λ, interact with a crystal containing parallel planes with a spacing of d_{hkl}, the diffracted X-rays will be in phase and constructively interfere only when the angle between the incident X-ray and the plane satisfies the equation:[60]

$$2d_{hkl}sin\theta = n\lambda \tag{2.1}$$

where θ is an angle between the incident beam and the diffracting planes and n is a positive integer and h, k and l are integers known as Miller indices that specify the orientation of the planes (Fig. 2.1).
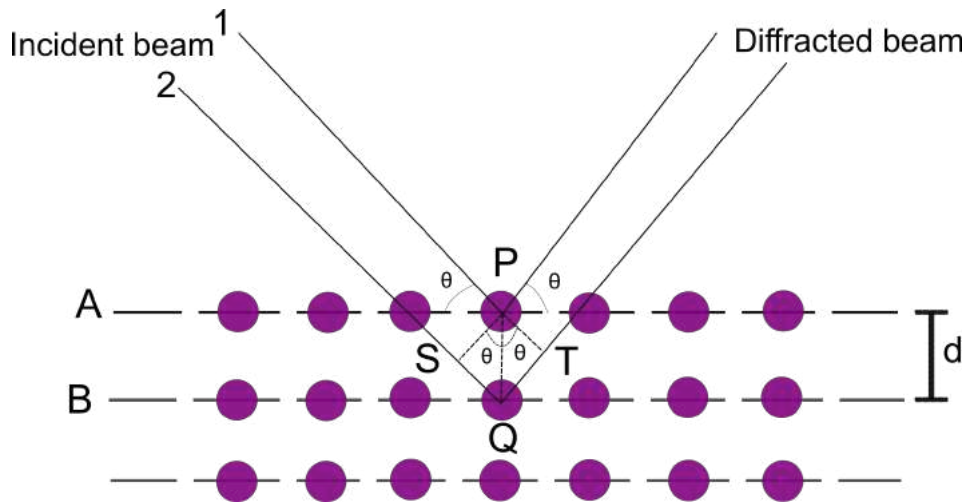
Figure 2.1: Diffraction of X-ray waves by crystallographic planes.

Bragg's law relates the diffraction angle to the inter planar spacing d_{hkl}. Then the equation, which relates the distance between planes with the lattice parameters a, b and c and the Miller indices h, k and l, can be used to calculate the orientation of the plane:

$$\frac{1}{d_{hkl}^2} = \frac{4}{3}\frac{h^2 + hk + k^2}{a^2} + \frac{l^2}{c^2} \tag{2.2}$$

This equation holds for hexagonal unit cells ($a = b$; $\alpha=\beta=90$ $\gamma=120$).

X-rays have the ability to interact with the electrons of atoms, and the scattering power of electrons by X-rays is known as the atomic scattering factor. This factor is proportional to the atomic number of the element and is identical for all atoms of the same element. The formula for atomic scattering factor (f_i) is given by

$$f_i = f_0 exp(\frac{-Ksin^2\theta}{\lambda^2})$$ (2.3)

Where f_0 = atomic scattering factor for a non-oscillating atom

λ = radiation wavelength

θ = incident angle.

The intensity of the diffracted beam (I_{hkl}) by a ($h\,k\,l$) plane of the crystal is determined by the structure factors (F_{hkl}), which is the sum of all contributions of the atoms in the crystal:

$$I_{hkl} \sim F_i = \sum_{n=1}^{N} f_i exp2\pi i(hx_i + ky_i + lz_i)$$ (2.4)

f_i = atom scattering factor

h, k, l = miller indices of the reflecting plane

x, y, z = coordinates of the i-th atom in the unit cell

structure factor indicates that intensity of the diffracted beam depends on the kind of atom (f_i) and its position (x, y, z) or the matter distribution in the crystal lattice.The geometry of the diffraction pattern, described by the Bragg law, depends on the cell parameters, such as a, b, c, α, β and γ, which are related to the sizes of atoms and molecules in the crystal lattice and their interactions [56, 58, 59].

2.2 Sources of X-rays

X-ray diffraction is based on the principle that when X-rays are directed at a crystal, they interact with the atoms in the crystal's lattice structure, causing the X-rays to diffract or scatter. This scattering produces a diffraction pattern can be captured on a detector. Two main types of experiments are conducted, namely angle dispersive (constant-wavelength) and energy dispersive (constant-angle) experiments. In this dissertation, only the constant-wavelength approach was used, which involves generating a monochromatic X-ray beam of a constant wavelength using either an X-ray tube in a laboratory diffractometer or a source of synchrotron radiation. To ensure a monochromatic beam, appropriate optics or monochromators are required. A comprehensive explanation of two types of X-ray radiation sources is given below.

2.2.1 X-ray tubes

In X-ray diffraction, X-rays are generated in an X-ray tube, which is a type of vacuum tube that converts electrical energy into X-rays. X-ray tubes have a cathode and an anode, and when a high voltage is applied across these two elements, electrons are emitted from the cathode and accelerated towards the anode. As the electrons hit the anode, they undergo an energy loss, resulting in the production of X-rays.

The material used in the anode of an X-ray tube depends on the application and the desired properties, such as melting point, thermal conductivity, and X-ray production efficiency. Common materials used in X-ray tube anodes include molybdenum and copper.

The choice of the anode depends on the method and purpose as discussed in detail e.g. in textbooks [56, 58]. Copper anode is a popular choice for X-ray crystallography because it produces X-rays with a lower energy than tungsten or molybdenum. This lower energy is ideal for crystallography because it causes less radiation damage to the crystal, resulting in higher quality diffraction patterns. Additionally, copper has a high thermal conductivity, allowing it to effectively dissipate heat produced during X-ray production. This reduces the likelihood of thermal damage to the anode and helps maintain X-ray tube performance.

Most of the X-rays are produced through bremsstrahlung radiation, which occurs when an energetic electron passes near the atomic nucleus of the target material. If the accelerated electron's energy towards the target is sufficiently high, it can result in the production of characteristic X-rays by interacting with an inner shell orbital electron in the target material. The type of radiation produced depends on the involved atomic shells (such as K, L, and M). For instance, when an electron transitions from the L shell to the K shell, it generates K radiation ($K_{\alpha 1}$ and $K_{\alpha 2}$). If the transition is from the M to K shell, it produces K_β radiation. Similarly, when the transition occurs from the M to L shell, it results in L_α radiation. On the other hand, bremsstrahlung radiation exhibits a continuous energy spectrum, while characteristic radiation displays distinct peaks. For a specific element, each peak pattern is unique [56].

2.2.2 Synchrotron radiation

Synchrotron radiation is a type of electromagnetic radiation emitted by charged particles, when they are forced to change direction under the influence of magnetic fields while traveling at close to the speed of light. The most common sources of synchrotron radiation are circular electron or positron accelerators, also known as storage rings. These rings

consist of circular pipes in which charged particles are made to follow circular paths by magnets placed along the circumference, called bending magnets. The particles are first accelerated by a linear accelerator until their energy reaches several million electron volts (MeV), and then further boosted by a booster ring to reach billions or giga electron volts (GeV) of energy before being injected into the storage ring.
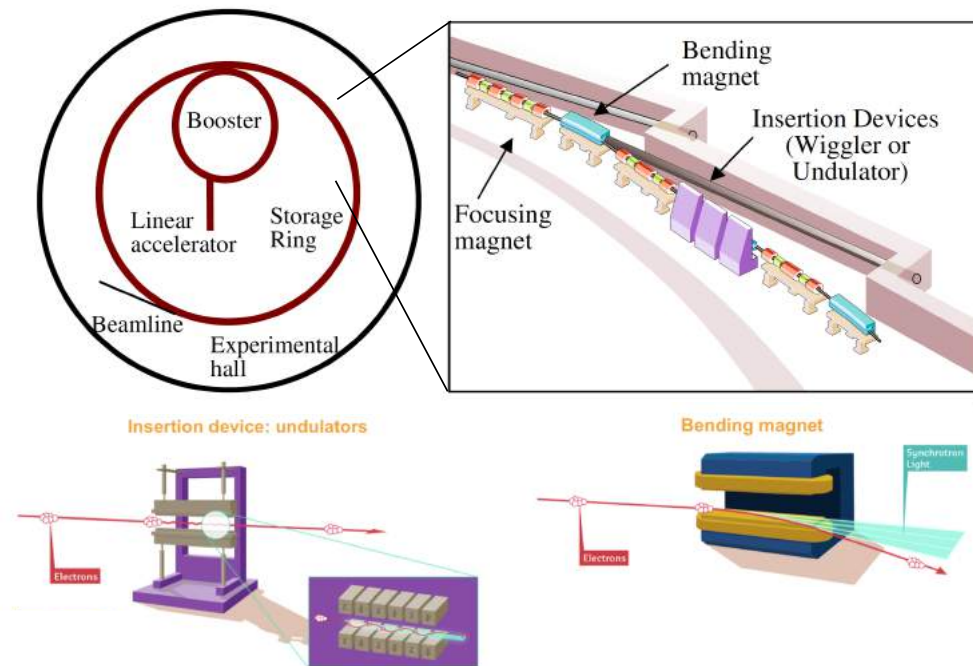
Figure 2.2: General scheme of ESRF synchrotron and element in storage ring (figure based on ref. [61])

To enhance the emission of synchrotron radiation, insertion devices such as wigglers and undulators are used. These devices consist arrays of magnets that generate sinusoidal magnetic fields perpendicular to the direction of the particle beam. The magnetic field induces horizontal "wiggles" in the orbits of electrons or positrons, leading to the emission of radiation along the insertion device.

The energy spectrum of the radiation emitted by a wiggler is continuous, while that of an undulator is structured, consisting of fundamental and harmonic wavelengths that can be tuned by changing the gap between magnets. Additionally, the light emitted by an undulator is much more collimated and brighter than that produced by a wiggler. More detail information can be found in Refs. [62–64].

2.3 Powder X-ray diffraction

Powder diffraction is a widely used technique for studying crystalline materials. The basic principle of powder diffraction is based on Bragg's law. In powder diffraction, the sample contains many small randomly oriented crystals, and there will always be several in the correct position for diffraction according to Bragg's law.

There are several ways of instrumental setup with respect to the X-ray source and the recording device which each of them has advantages and disadvantages in terms of required sample amounts, recording time, and peak resolution. In this dissertation, two different geometries, namely Bragg-Brentano and Debye-Scherrer, have been utilized, and their descriptions are provided below.

2.3.1 Bragg-Brentano geometry

In the classical Bragg-Brentano geometry, the primary principle involves focusing the diffracted beam onto the detector. This is achieved by placing a flat sample, a radiation source, and a detector on the focusing circle of the diffractometer. The source and detector are positioned equidistantly from the sample. During the measurement process, two out of the three components (X-ray tube, sample, detector) rotate simultaneously around the axis of the diffractometer. This rotation can occur between the source and the detector, resulting in a movement by an angle of θ, while the sample remains fixed. Another setup involves rotating the sample by θ while the detector moves at an angle of 2θ.

The Bragg-Brentano geometry, commonly employed in powder diffraction experiments, can be improved to obtain accurate and high-quality diffraction patterns by modifying the X-ray beam path. In the laboratory measurements conducted for this dissertation, the Bragg-Brentano geometry, as shown in Fig. 2.3, was employed. Soller slits were used to improve the quality and resolution of the diffraction pattern. These slits effectively limit the axial divergence of the incident and diffracted X-ray beams, thereby improving peak shape and resolution in 2θ-θ scans, particularly at low scattering angles. The Soller slits consist of a set of parallel plates that reduce axial divergence. One slit is placed in the path of the incident beam, while the second slit is positioned along the path of the diffracted beam. The applied apparatus is a modern version equipped with a primary beam monochromator and a linear position-sensitive detector. Further details about this geometry can be found in [65, 66].
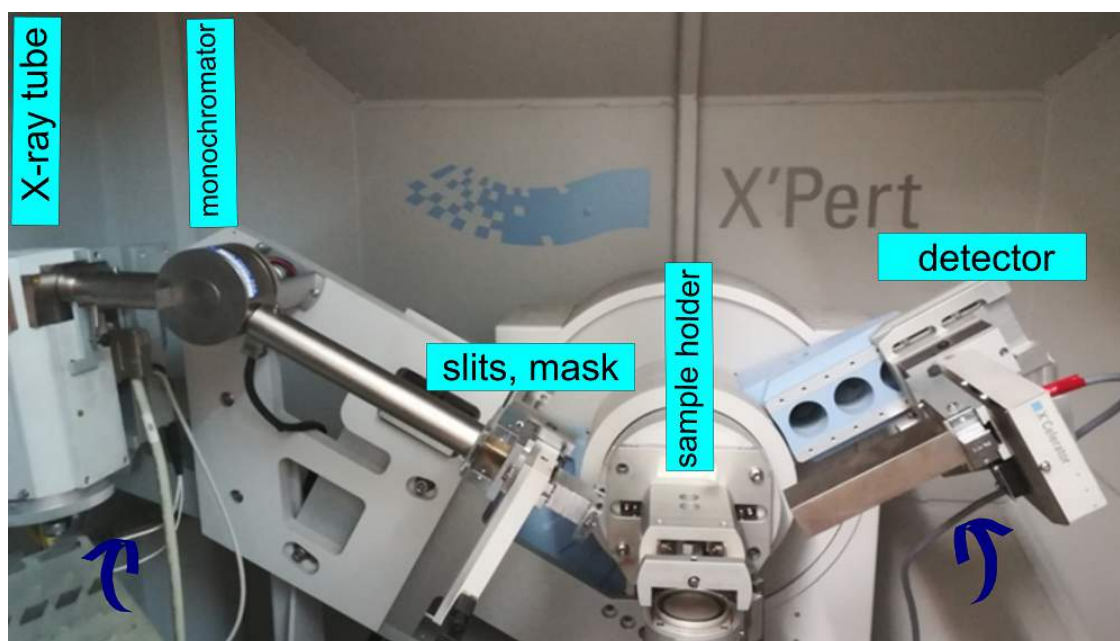
Figure 2.3: X'Pert PRO MPD (PANalytical) diffractometer in a Bragg-Brentano geometry

2.3.2 Debye-Scherrer geometry

In Debye-Scherrer geometry, a fine powdered sample is placed inside a capillary, which is then mounted on a spinner to allows for improving the peak shape because much more crystallites will be at diffraction position. The incident X-ray beam, typically produced by an X-ray tube, is directed towards the sample in a parallel manner.

One of the key advantages of the Debye-Scherrer method is its ability to analyze samples using a very small amount of material. This makes it particularly useful for handling air or moisture-sensitive samples, as the top of the capillary can be easily sealed to prevent contamination. However, due to scattering from air and the capillary, the background level of the Debye-Scherrer method is generally higher than that of the Bragg-Brentano geometry.

In this dissertation, the Debye-Scherrer geometry was employed at the ID22 beamline located at the European Synchrotron Radiation Facility (ESRF). The diffractometer was equipped with nine analyser crystals, which are mounted on an arm, and scan over a 2θ angle. This geometry, known as the parallel-beam geometry, has been shown to greatly improve the angular accuracy and resolution of the diffractogram. The use of multiple analyzer crystals help to reduce noise in the diffraction pattern, leading to more accurate analysis of the sample structure.
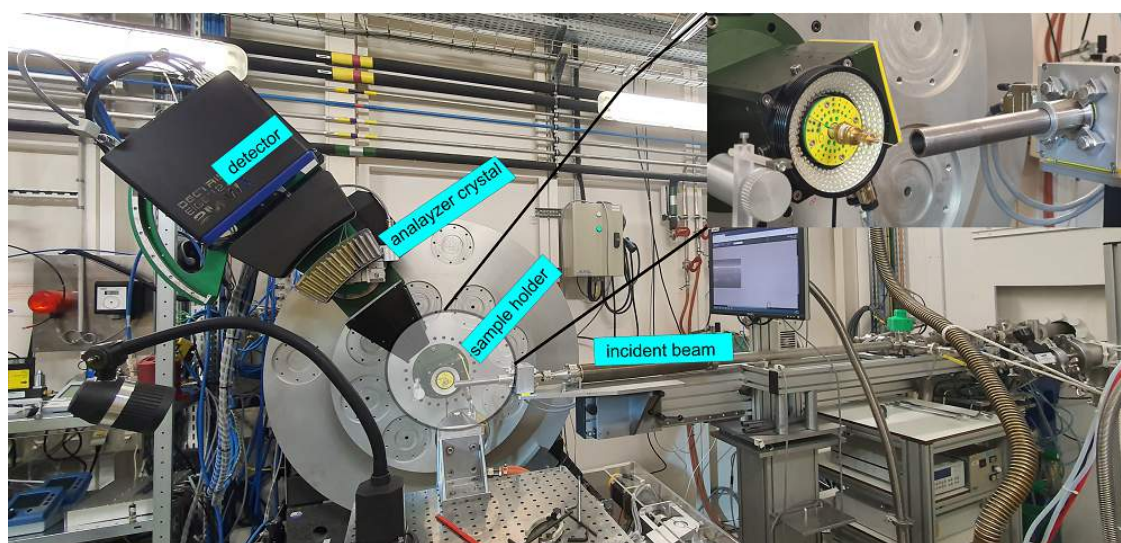
Figure 2.4: X-ray diffractometer at a synchrotron beamline with the high-resolution setup (ID22 beamline, ESRF).

2.4   Structure refinement by the Rietveld method

The Rietveld method, named after Hugo Rietveld, was introduced in the late 1960s and first presented at the seventh congress of the International Union of Crystallography (IUCr) in Moscow in 1966 [67]. This method was further improved the following year [68] and has since become the predominant approach for refining structures based on powder diffraction data. In contrast to other methods, which were developed before the Rietveld method, that minimize the difference between the calculated and observed intensities of individual peaks, the Rietveld method optimizes the fit of the entire diffraction pattern simultaneously.

The following equation represents the minimization process based on the method of least squares, where the squared sum of differences between the observed ($Y_{obs,i}$) and calculated ($Y_{calc,i}$) step scan intensities in a powder pattern is minimized:

$$\sum_{i=0}^{n-1} w_i (Y_{obs,i} - Y_{calc,i})^2 \tag{2.5}$$

where n represents the total number of intensity steps while the running index *i* represents the angular position in the powder pattern according to

$$2\theta_i = 2\theta_{start} + i\Delta 2\theta \tag{2.6}$$

with the starting angle $2\theta_{start}$ and the angular step width $\Delta 2\theta$. The weight w_i is derived from the variance of $Y_{obs,i}$.

The calculated intensity $Y_{calc,i}$ is expressed by

$$Y_{calc,i} = \sum_{ph=1}^{phases} \left(S_{ph} \sum_{hkl(ph)} \left(K_{hkl,(ph)} F^2_{hkl(hp)} \Phi_{hkl(ph)} (2\theta_i - 2\theta_{hkl(ph)}) \right) \right) + b_i(obs) \qquad (2.7)$$

The outer sum runs over all phases, *ph*, present in the powder pattern, while the inner sum runs over all reflections, *hkl*, of a phase *ph* that contribute to position *i* in the powder pattern. The scaling factor S_{ph} assigned to each phase in the powder pattern is proportional to its weight fraction. The product of various correction factors to the reflection intensities, represented by $F^2_{hkl(hp)}$, is denoted as $K_{hkl,(ph)}$. These correction factors depend on the diffraction geometry and material characteristics.

The profile function, $\Phi_{hkl}(2\theta_i - 2\theta_{hkl})$, is defined for the profile point $(2\theta_i - 2\theta_{hkl})$ relative to the position of the Bragg reflection *hkl*. The observed background at position *i* in the powder pattern is denoted as $b_i(obs)$.

In order to analyze a powder pattern, the entire pattern must be modeled. However, modeling the entire pattern is a complex task. The information content of the pattern can be divided into several distinct parts, such as peak intensity, peak shape, peak position, and background.

Peak intensity: The intensity of a Bragg reflection *hkl* is determined by the squared absolute value of the structure factor amplitude F_{hkl}. This amplitude can be calculated by summing up the atomic form factors, which are multiplied by the complex phase factor that is dependent on the Miller indices *hkl*, as well as the relative positions of all atoms in the unit cell, x, y, and z.

The correction factors, K_{hkl}, include the multiplicity of a reflection, as well as the Lorentz-polarization factor, preferred orientation correction and absorption. The multiplicity of a reflection accounts for the number of symmetry-related reflections that overlap in the diffraction pattern. Additionally, the Lorentz–polarization factor corrects for the varying intensities of the diffracted X-rays due to the geometry of the diffractometer and the polarization of the X-rays, while the preferred orientation correction accounts for the possibility of certain crystallites being preferentially oriented in a particular direction.

Peak shape: The peak shape is influenced by various factors such as the size of the crystallites or domains, the level of stress or strain within the sample, and the presence of defects or vacancies. In addition, the geometry of the experiment and experimental optics affect the peak shape. The accurate description of the peak shapes in a powder pattern is vital to the success of Rietveld refinement.

The pseudo-Voigt function is widely used to approximate the peak shape of X-ray diffraction pattern. The function is expressed as a linear combination of the Gaussian and Lorentzian functions, where the mixing parameter determines the relative weight of the two functions.

Peak position: The 2θ position of the *hkl* reflection is determined by Bragg's law, which relates the scattering angle (2θ) of the incident X-ray beam and the distance between the atomic planes (d_{hkl}) in the crystal lattice, given the wavelength of the radiation (λ) used. For precise correction of the peak position, it is crucial to consider additional corrections related to systematic errors such as zero shift and sample displacement.

Background: At a given position i in the powder pattern, the background signal, denoted as $b_i(obs)$, can be effectively modeled using a function with refinable parameters. This modeling approach often employs orthogonal Chebyshev polynomials of higher order. Alternatively, the background can be estimated and then subtracted by a linearly interpolated set of points. While the former method may appear more elegant, the latter approach is considered more sophisticated and proves useful when the polynomial function fails to accurately represent the background characteristics.

Refinement analysis

Several statistical agreement, (R-) factors, used to evaluate the quality of a Rietveld refinement.

Profile factor:

$$R_P = \frac{\sum_{i=1}^{n} |y_{obs,i} - y_{calc,i}|}{\sum_{i=1}^{n} y_{obs,i}} \tag{2.8}$$

Weighted profile factor:

$$R_{wp} = \left[\frac{\sum\limits_{i=1}^{n} w_i |y_{obs,i} - y_{calc,i}|}{\sum_{i=1}^{n} w_i y_{obs,i}} \right]^{1/2} \tag{2.9}$$

expected weighted profile factor:

$$R_{exp} = \left[\frac{N - P}{\sum_i w_i y_{obs,i}} \right]^{1/2} \tag{2.10}$$

where N is the number of observation and P is the number of parameters.

Goodness of fit:

$$\chi^2 = \frac{R_{wp}}{R_{exp}} \tag{2.11}$$

Bragg intensity factor:

$$R_{Bragg} = \frac{\sum_k |I_{obs,k} - I_{calc,k}|}{\sum_k |I_{obs,k}|} \tag{2.12}$$

where $I_{obs,k}$ and $I_{calc,k}$ are observed and calculated intensities respectively of the kth reflection.

2.5 Thermal expansion determination by X-ray diffraction

Thermal expansion is a fundamental characteristic for understanding the temperature-dependent behavior of materials and is critical in materials science. It affects the optical power of a thermal lens, and knowledge of the thermal expansion coefficient (TEC) is beneficial in preventing crystal cracking during the processes of growth, annealing, and laser action [18]. On the other hand, in the design of alloys for high-temperature applications, the materials must have high thermal expansion coefficients to prevent thermal shock.

The expansion of a material occurs due to an increase in the kinetic energy of the atoms when heated. This causes the atoms to move around their position in the crystal lattice, increasing the average distance between them. This increase in distance between atoms results in a change in the length of the unit cell and causes the distance between

planes to increase, shifting the position of the corresponding plane's Bragg peak. The rate of expansion varies for different materials and is not necessarily the same in every direction.

Classical techniques used to measure thermal expansion include dilatometry (inductive, capacity, optical interference) and diffraction methods such as X-ray or neutron diffraction. Among these, diffraction methods are often employed to investigate temperature-dependent behavior in single crystals or polycrystalline compounds. By analyzing diffractograms obtained at different temperatures while heating, the lattice parameters (a, b, c) and unit cell volume (V) can be determined using Rietveld refinement, enabling the derivation of the $L(T)$ dependence (where $L = a, b, c, V$). At high temperatures ($\gtrsim 300$ K), an empirical form of thermal expansion is commonly used:[69]

$$V(T) = V_{T_0} exp[\int_{T_0}^{T} \alpha(T) dT] \tag{2.13}$$

where V_{T_0} is the volume at the reference temperature T_0 (here taken to be 300 K) and α_T is the volumetric thermal expansion coefficient with the first order.

$$\alpha(T) = \alpha_0 + \alpha_1 T \tag{2.14}$$

The value of V_{T_0}, α_0 and α_1 can be evaluated by fitting graph of volume against to temperature.

According to the most general approach, the thermal expansion coefficient can be defined as:

$$\alpha_L = \frac{1}{L(T)} (\frac{dL}{dT})_p \tag{2.15}$$

which simply describes the change of L (it can be lattice parameters or unit cell volume) when the temperature of the material is increased, assuming constant pressure p condition. This thesis employed a numerical approach to calculate the thermal expansion coefficient across a wide range of temperatures. Additionally, polynomial functions and the Debye approximation were utilized within a specific temperature range.

2.6   Debye temperature

In a crystal lattice, atoms are arranged in a periodic manner, forming a repeating pattern. In a state of thermodynamic equilibrium, these atoms remain immobile and exhibit no

discernible movement or displacement. However, when the crystal is subjected to an external force, such as heat or pressure, the atoms begin to vibrate around their equilibrium positions. These vibrations are known as phonons, and they contribute to the crystal's thermodynamic properties such as specific heat, thermal conductivity, and thermal expansion.

The Debye temperature (θ_D) describes the temperature of a crystal's highest normal mode of vibration. It serves as a crucial parameter that connects the elastic and thermodynamic properties of a crystal, including phonons, thermal expansion, thermal conductivity, specific heat, and lattice enthalpy [70].

At low temperatures, the unit cell volume and thermal expansion data can be fitted by utilizing Debye approximations as a theoretical approach. This model treats the effects of thermal expansion as equivalent to elastic strain, thus enabling the estimation of Debye temperature. When dealing with data covering a broad temperature range, a second-order Grüneisen approximation in the form is more suitable: [71, 72]

$$V(T) = V_0 + \frac{V_0}{Q - bU} \tag{2.16}$$

where V_0, b and Q can be evaluated by fitting. The internal energy, U, as function of temperature is calculated using the Debey approximation

$$U(T) = 9Nk_BT \left(\frac{T}{\theta_D}\right)^3 \int_0^{\theta_D/T} \left(\frac{x^3}{exp(x) - 1}\right) dx \tag{2.17}$$

where k_B is Boltzmann's constant, θ_D is the Debye temperature and N is the number of atoms in the unit cell.

These equations provide a framework for the calculation of the thermal expansion based on the Debye approximation and fitting parameters.

Chapter 3

Details of synthesis and X-ray diffraction experiment

3.1 Method of synthesis of $Ca_{10.5-x}TM_x(VO_4)_7$

The synthesis of materials belonging to the calcium orthovanadates family has been extensively described in numerous scientific papers. Initially, the Czochralski method was employed as the primary technique for synthesizing $Ca_3(VO_4)_2$, due to the interest in investigating the optical properties of single crystals grown using this technique[1, 21, 73, 74]. However, subsequently, the solid-state reaction method has emerged as another synthesis technique for these types of materials [27, 75–77]. In this method, reactants are ground together and heated at high temperatures to promote diffusion and reaction between the constituents. More recently, high-temperature diffusion doping of calcium orthovanadate crystals has been performed using both closed-zone and open-zone diffusion techniques [54].

For this dissertation, TCV which is substituted by divalent transition metal were prepared by solid state reaction. There were two different starting point. For $Ca_{10.5-x}Co_x(VO_4)_7$ and $Ca_{10.5-x}Cu_x(VO_4)_7$ the reaction is as follows:

$$CaCO_3 + V_2O_5 + TMO \rightarrow Ca_{10.5-x}TM_x(VO_4)_7 + CO_2^{\uparrow} \quad TM = Co, Cu \qquad (3.1)$$
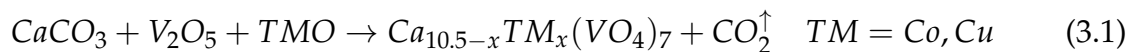
The samples were achieved by mixing CoO (99.7%), CuO (99.9%), V_2O_5 (99.995%), and $CaCO_3$ (99.995%) in stoichiometric proportions. The resulting mixture was then subjected to a uniaxial pressure of 200 kPa to form pellets.

The pellets were subsequently calcined in a three-step process, each lasting 6 hours. The first step was conducted at a temperature of 1273 K, while the following two steps

were carried out at 1173 K [P1]. The resulting materials were found to have different colors (figure 3.1).

Figure 3.1: Photographs of samples synthesised by solid-state reaction (left-$Ca_{10.5-x}Co_x(VO_4)_7$, right- $Ca_{10.5-x}Cu_x(VO_4)_7$)

The synthesis of polycrystalline samples of $Ca_{10.5-x}Ni_x(VO_4)_7$ followed a solid-state reaction method using stoichiometric ratios of CaO, NiO (99.99%), and V_2O_5 (99%). CaO was obtained from $CaCO_3$ (99%) by heating in air at 1173 K for several days. For each sample, powders thoroughly mixed, and placed in an alumina crucible with a cover, then subjected to a temperature of 1173 K for about 16 h in air. The resulting powder was ground, formed into pellets, and then heated at 1273 K for 16 h, except for the first sample ($Ca_{10.34}Ni_{0.16}(VO_4)_7$), which was heated at 1323 K. The synthesis reaction was carried out according to the following formula [P3]:

$$(10.5 - x)\, CaO + 3.5\, V_2O_5 + x\, NiO \rightarrow Ca_{10.5-x}Ni_x(VO_4)_7 \tag{3.2}$$
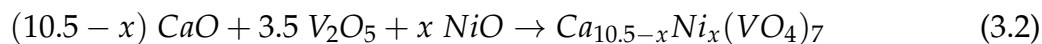
The yellowish color of the samples was observed to become more intense with increase of the content of Ni (figure (3.2)).

3.2 X-ray diffraction experiments

Polycrystalline samples were analyzed by collecting powder patterns at X'Pert PRO MPD (PANalytical) diffractometer equiped with a Cu X-ray tube. Phase analysis was conducted on the obtained diffractograms using X'Pert HighScore software and ICSD databases.
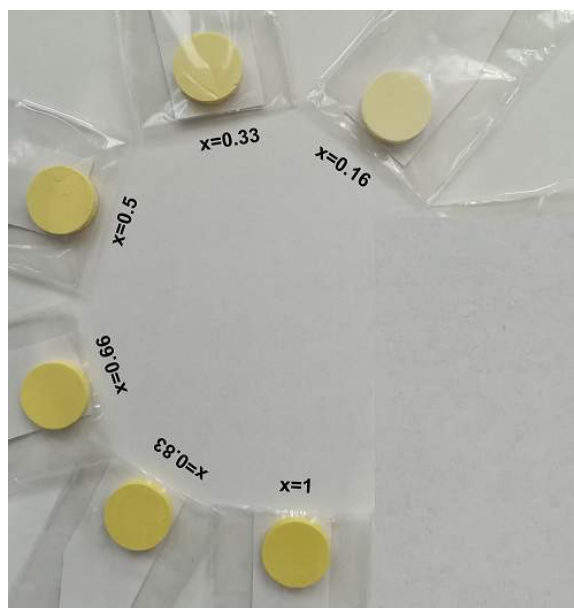
Figure 3.2: photograph of samples synthesised by solid-state reaction $(Ca_{10.5-x}Ni_x(VO_4)_7)$

3.2.1 Laboratory measurements-room temperature

In the conducted experiments, a Bragg-Brentano geometry was utilized under ambient conditions. The incident beam was monochromtaize a Johansson (Ge) monochromator that provided $CuK\alpha_1$ radiation with a wavelength of 1.54056 Å. To formation of the incident beam, divergence ($1°$) and anti-scattering ($2°$) slits were placed in the beam's path, followed by Soller slits (0.02 rad). The mask was adjusted to fit the diameter of the specimen, typically 20 mm, on the sample holder. Additional Soller slits (0.04 rad) were placed in the reflected beam path to improve the peak shape. A semiconductor strip detector X'Celerator was used to collect the diffracted X-rays. The scans were performed in continuous mode, and the recording step was set to $0.0167°$. The temperature was maintained at 298(2) K during the measurement. Further information about the experimental setup can be found in Ref. [66]. The collected powder diffractograms were subjected to Rietveld refinements using the FullProf suite program [78] to refine the crystal structure of the synthesized samples.

3.2.2 Laboratory measurements-high temperature

As a part of the high-temperature measurements, a portion of the experiments was conducted on the X'Pert PRO diffractometer, which was also used for room temperature measurements. To perform these high-temperature experiments, the same diffractometer equipped with an HTK 1200N temperature stage. The measurements were carried out

in the Bragg-Brentano geometry, using CuKα radiation with two different wavelengths (λ_1 = 1.54056 Å and λ_2 = 1.54439 Å). The powder was placed in a alumina sample holder (Fig. 3.3). The temperature range was set from 300 K up to 1200 K with different temperature steps, which were typically 50 or 100 K. A waiting time of 2 minutes was set after reaching the required temperature step to stabilize the temperature and ensure uniform temperature within the sample.
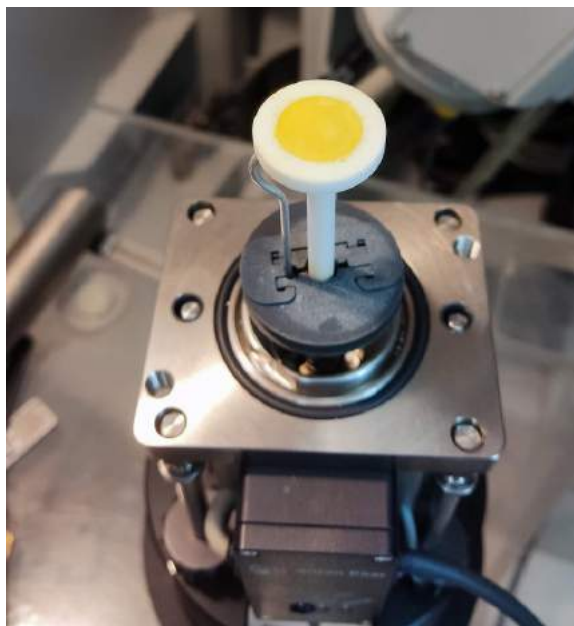
Figure 3.3: Photograph of samples prepared for high temperature measurement at laboratory

3.2.3   Synchrotron measurements-high temperature

The high-resolution powder X-ray diffraction experiments were conducted at the ID22 beamline of the European Synchrotron Radiation Facility (ESRF) in Grenoble for two samples at high temperatures. The powder was placed in a quartz capillary with a diameter of 0.7 mm (Fig. 3.4). The patterns were collected using a parallel-beam, high-resolution setup, with nine detectors situated behind nine analyzer crystals, as described in Ref. [79]. The wavelength of the X-rays used was λ = 0.400218(4) Å. The temperature was varied in steps of 50 or 100 K, starting from 300 K and up to 1200 K.

Figure 3.4: Photographs of samples prepared for high temperature XRD measurement at synchrotron beamilne

Figure 3.5: Photographs of samples prepared for low temperature XRD measurement at synchrotron beamilne

3.2.4   Synchrotron measurements-low temperature

High-resolution X-ray powder diffraction was employed to perform low temperature (LT) measurements on three selected samples at the ID22 beamline of the European Synchrotron Radiation Facility (ESRF). A helium cryostat was utilized to conduct the measurements over a temperature range of 4–29 K. The high-resolution diffraction data were collected at LT, using a nine-crystals multi-analyzer stage and a wavelength of 0.35420(1) Å. XRD patterns were obtained from a fine powder of samples that was sealed in a 0.5 mm diameter borosilicate glass capillary (Fig. 3.5).

Chapter 4

Structure study of $Ca_{10.5-x}TM_x(VO_4)_7$ at room temperature

4.1 Phase analysis

The phase analysis of $Ca_{10.5-x}Co_x(VO_4)_7$, $Ca_{10.5-x}Ni_x(VO_4)_7$ and $Ca_{10.5-x}Cu_x(VO_4)_7$ compounds at room temperature was conducted, revealing that all samples crystallize in the $R3c$ space group. However, in most of the $Ca_{10.5-x}Co_x(VO_4)_7$ and $Ca_{10.5-x}Cu_x(VO_4)_7$ samples, a trace of $Ca_2V_2O_7$ was observed. In the case of $Ca_{9.67}Co_{0.83}(VO_4)_7$, a trace of $Ca_{2.5}Co_2(VO_4)_3$ was detected.

On the other hand, for $Ca_{10.5-x}Ni_x(VO_4)_7$ samples, no impurity was observed until $x = 0.66$. However, for $x = 0.83$, a few extra peaks of low intensity were detected, and for $x = 1$, these peaks were markedly stronger. These impurity phases were identified as $Ca_{2.5}Ni_2(VO_4)_3$ crystallized in a cubic structure. The initial identification of these impurity phases was based on the layout of the diffraction peak positions and intensity relations, which was further confirmed by the Rietveld refinement. The results of the phase analysis are presented in Tables 4.1, 4.2, and 4.3.

Additionally, for the $Ca_{10.34}Co_{0.16}(VO_4)_7$, $Ca_{10.34}Cu_{0.16}(VO_4)_7$, $Ca_{10.17}Co_{0.33}(VO_4)_7$, $Ca_{10.17}Cu_{0.33}(VO_4)_7$ and $Ca_{10}Cu_{0.5}(VO_4)_7$ samples, several foreign peaks were observed. However, the corresponding phase was not identified. The foreign phase remained despite additional annealing of these samples. Supposedly the foreign peaks correspond to carbon containing phase that did not decompose despite the prolonged annealing. A zoom on the low 2θ angles is presented in Fig. A.16 for the compounds in which some minor phases occur.

Table 4.1: Phase analysis of Ca$_{10.5-x}$Co$_x$(VO$_4$)$_7$.

x	Ca$_{10.5-x}$Co$_x$(VO$_4$)$_7$	Ca$_2$V$_2$O$_7$	Ca$_{2.5}$Co$_2$(VO$_4$)$_3$	foreign peaks
0.16	+	-	-	+[a]
0.33	+	+	-	-
0.5	+	+	-	-
0.66	+	+	-	-
0.83	+	+	-	-
1	+	+	+	-

[a] There are foreign peaks at (2θ (°), d (Å)) = (14.87,5.952),(16.05,5.510),(19.31,4.593),
(19.35,4.583) ,(20.45,4.339),(23.12,3.844),(23.42,3.795),(24.89,3.574),(25.12,3.542),
(26.29,3.387),(29.22,3.054),(29.50,3.025),(29.96,2.980),(31.04,2.878),(32.42,2.759),
(34.15,2.623),(34.23,2.617) with less than 29% intensity.

Table 4.2: Phase analysis of Ca$_{10.5-x}$Ni$_x$(VO$_4$)$_7$.

x	Ca$_{10.5-x}$Ni$_x$(VO$_4$)$_7$	Ca$_{2.5}$Ni$_2$(VO$_4$)$_3$
0.16	+	-
0.33	+	-
0.5	+	-
0.66	+	-
0.83	+	+
1	+	+

4.2   Rietveld refinement for Ca$_{10.5-x}$TM$_x$(VO$_4$)$_7$ compounds

The materials crystal structures in this thesis were determined using the Rietveld method, which is a routine procedure for crystal structure refinement. Refinements were performed with different numbers of parameters, depending on the specific sample being analyzed. The selection of parameters was sample-dependent and carefully considered.

The background treatment was a crucial step, as it depended on the shape and complexity of the background. In general, a 3 or 4-term polynomial was used to fit the background, along with additional terms proportional to $1/(2\theta)$, $1/(2\theta)^2$. However, for a few samples, the background was determined manually and refined later in the calculation process. Any artifacts originating from the sample holder in non-ambient temperature were usually excluded from refinements to avoid their impact on the refinement quality.

Table 4.3: Phase analysis of $Ca_{10.5-x}Cu_x(VO_4)_7$.

x	$Ca_{10.5-x}Cu_x(VO_4)_7$	$Ca_2V_2O_7$	foreign peaks
0.16	+	-	+[a]
0.33	+	-	+[b]
0.5	+	+	+[c]
0.66	+	+	-
0.83	+	+	-
1	+	+	-

[a] There are foreign peaks at $(2\theta\ (°),\ d\ (\text{Å})) = (19.25,4.607),(19.28,4.600),$
(20.40,4.350),(21.55,4.120),(23.14,3.840),(23.41,3.797),(23.46,3.789),
(24.52,3.627), (24.86,3.578),(26.47,3.364),(30.04,2.972),(32.64,2.741),
(34.10,2.627),(34.22,2.618) with less than 18% intensity.
[b] There are foreign peaks at $(2\theta\ (°),\ d\ (\text{Å})) = (27.57,3.233),(29.19,3.057),$
(30.12,2.964),(30.83,2.898),(32.09,2.786),(32.15,2.781),
(35.23,2.545),(35.33,2.538) with less than 7% intensity.
[c] There are foreign peaks at $(2\theta\ (°),\ d\ (\text{Å})) = (25.77,3.454),(36.77,2.442),$
(37.00,2.427), (37.07,2.423) with less than 1% intensity.

To refine the crystal structure, various parameters such as the scale parameter, lattice constants, and systematic errors (sample displacement corrections) were introduced. For powder data from room temperature measurements, all atomic positions were refined. The occupancy of vanadium (V) and oxygen (O) were fixed, while isotropic atomic displacement parameters were set to be identical for all oxygen atoms. Attempts at refining individual atomic displacement parameters of oxygen failed, indicating that they are inherently linked and cannot be refined independently due to low scattering factor.

The pseudo-Voigt function was used to model the diffraction peak shapes, and asymmetry function were also included in the refinement due to axial beam divergence . The Rietveld refinements were performed for room temperature for all samples, and the results are presented below.

In the following chapter, we illustrate the Rietveld refinement and provide a more comprehensive qualitative analysis of phase characterization. Full results of structure refinements are available in the Tables A.1, A.2, A.3, and A.4. The discussion of the trends in lattice parameters, occupancy and interatomic distances in the $Ca_{10.5-x}TM_x(VO_4)_7$ compounds, based on the obtained structure models, is conducted in section 4.3, 4.4, and 4.5.

4.2.1 $Ca_3(VO_4)_2$

The diffraction pattern shows a perfect match with the $Ca_3(VO_4)_2$ pattern reported in the literature [2], and no foreign phases were detected in the material (Fig. 4.1).
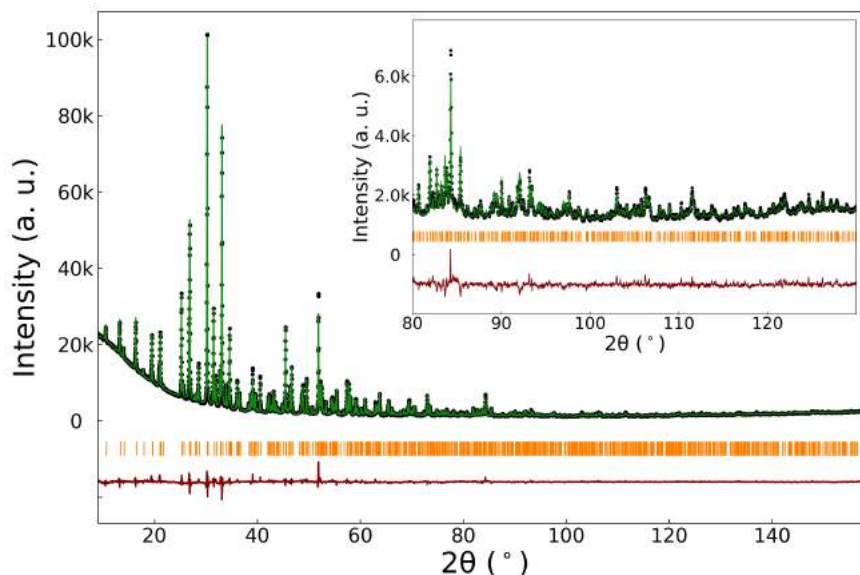
Figure 4.1: Illustration of the Rietveld refinement of $Ca_3(VO_4)_2$ sample. The experimental X-ray diffraction profile is represented by black circles, while the solid green line corresponds to the theoretically calculated X-ray diffraction pattern. The dark red line at the bottom represents the difference between the theoretical and experimental data. The orange vertical bars depict the Bragg positions, which are the characteristic peaks in the diffraction pattern. The refinement results are quantified by the R factors, with values of R factors are: Rp = 3.08%, Rwp = 4.46% and Rexp = 1.61%. Data were published in [P2].

4.2.2 $Ca_{10.5-x}Co_x(VO_4)_7$

The analysis of Rietveld refinement (illustrated in Figs. 4.2, A.1-A.5) revealed the presence of a second phase related to $Ca_2V_2O_7$ (observed for samples starting with $x = 0.33$) increased from 1.4 wt% to 2.4 wt% for $x = 1$ (Table 4.4). The lattice parameters of the minor phase, $Ca_2V_2O_7$, were determined and found to be in close agreement with those reported in Ref. [80]. This result indicates that there is no significant difference in the chemical composition of this phase in comparison to the reported one. Additionally, a third phase related to $Ca_{2.5}Co_2(VO_4)_3$ [81] was identified for the sample with $x = 1$.

4.2.3 $Ca_{10.5-x}Ni_x(VO_4)_7$

The analysis of Rietveld refinement (illustrated in Figs. 4.3, A.6-A.10) demonstrate that the proportion of the minority phase, $Ca_{2.5}Ni_2(VO_4)_3$, was increased from 3 wt% (for

Table 4.4: Phase content of $Ca_{10.5-x}Co_x(VO_4)_7$.

x	$Ca_{10.5-x}Co_x(VO_4)_7$ (wt%)	$Ca_2V_2O_7$ (wt%)	$Ca_{2.5}Co_2(VO_4)_3$ (wt%)
0.16	100	-	-
0.33	98.6	1.4	-
0.5	98.3	1.7	-
0.66	97.9	2.1	-
0.83*	98.1	1.9	-
1*	92.4	2.4	5.2

* nominal x value
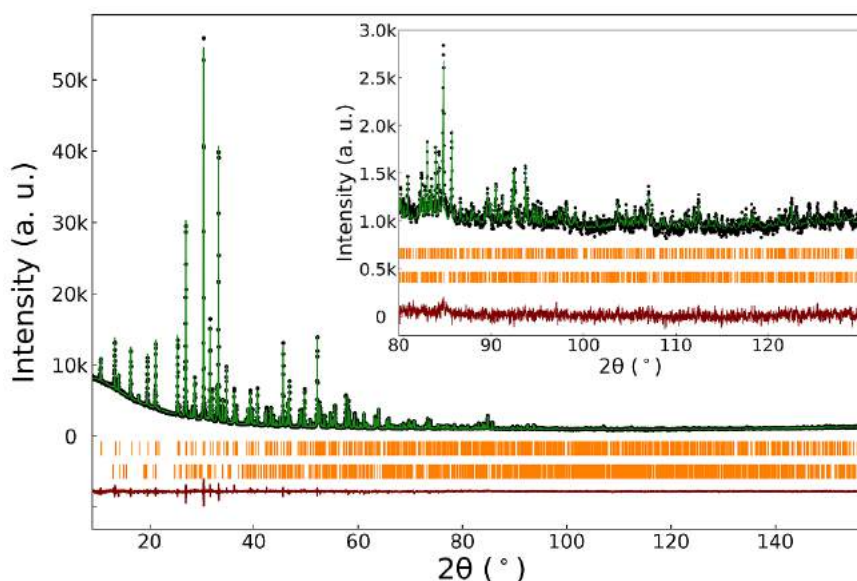
Figure 4.2: Illustration of the Rietveld refinement of $Ca_{10}Co_{0.5}(VO_4)_7$ sample. The upper orange vertical bars represent peak position of $Ca_{10}Co_{0.5}(VO_4)_7$ - main phase and the lower vertical bars represent peak position of $Ca_2V_2O_7$- minor phase. R factors are: Rp = 2.56%, Rwp = 3.35% and Rexp = 2.27%. Data were published in [P1].

$Ca_{9.67}Ni_{0.83}(VO_4)_7$) to 7 wt% (for $Ca_{10}Ni_1(VO_4)_7$) (Table 4.5). Analysis of the lattice parameters of $Ca_{2.5}Ni_2(VO_4)_3$ indicated values closely matching those reported in ref. [82]. These findings suggest that increasing the Ni content does not result in a significant alteration in the chemical composition of this phase.

4.2.4 $Ca_{10.5-x}Cu_x(VO_4)_7$

The obtained results (illustrated in Figs. 4.4, A.11-A.15) showed the presence of a secondary phase associated with $Ca_2V_2O_7$, which started to appear from $x = 0.5$. The proportion of this phase increased gradually from 3.3% to 6.2% at $x = 1$. The lattice parameters of the minor phase, $Ca_2V_2O_7$, were determined, and it was observed that they were

Table 4.5: Phase content of $Ca_{10.5-x}Ni_x(VO_4)_7$.

x	$Ca_{10.5-x}Ni_x(VO_4)_7$ (wt%)	$Ca_{2.5}Ni_2(VO_4)_3$ (wt%)
0.16	100	-
0.33	100	-
0.5	100	-
0.66	100	-
0.83*	97	3
1*	92.3	7.7

* nominal x value
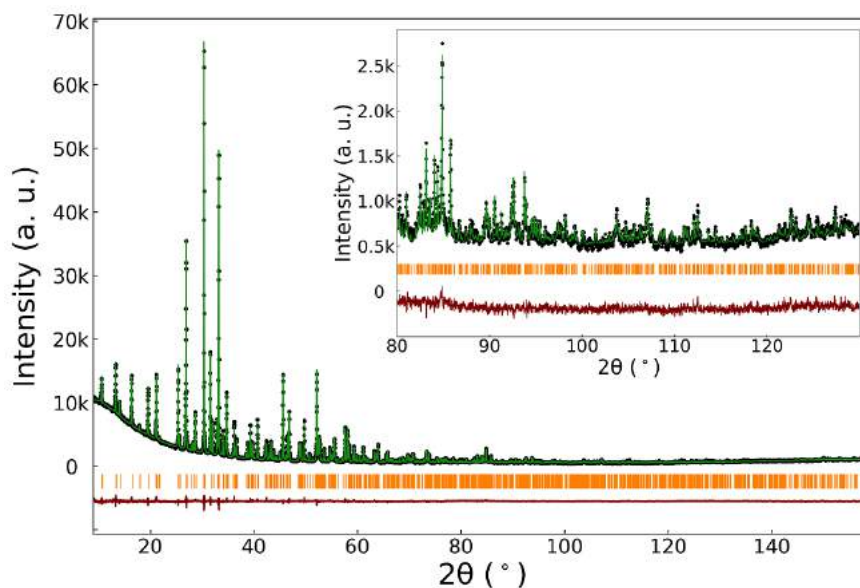
Figure 4.3: Illustration of the Rietveld refinement of $Ca_{10}Ni_{0.5}(VO_4)_7$ sample. R factors are: Rp = 2.78%, Rwp = 3.91% and Rexp = 2.37%. Data were published in [P3].

in close agreement with the values reported in ref. [80]. These findings suggest that there are no significant differences in the chemical composition of this phase compared to the reference. The full results of structure refinement are available in the Tables A.1, A.4.

4.3 Lattice parameters and solubility limit

The substitution of transition metals (Co, Ni, Cu) in $Ca_3(VO_4)_2$ results in changes in the refined lattice parameters of the TCV structure. The evolution of the lattice parameters a and c, as well as the unit cell size, were studied as a function of the substituent content (x). The results showed a nearly linear decrease in the lattice parameters below $x = 0.83$. For the last two samples ($x = 0.83$ and 1) unit cell size did not change and it because of solubility limit which will be discussed later.

Table 4.6: Phase content of $Ca_{10.5-x}Cu_x(VO_4)_7$.

x	$Ca_{10.5-x}Cu_x(VO_4)_7$ (wt%)	$Ca_2V_2O_7$ (wt%)
0.16	100	-
0.33	100	-
0.5	96.7	3.3
0.66	96.7	3.3
0.83 *	95.0	5.0
1 *	93.8	6.2

* nominal x value
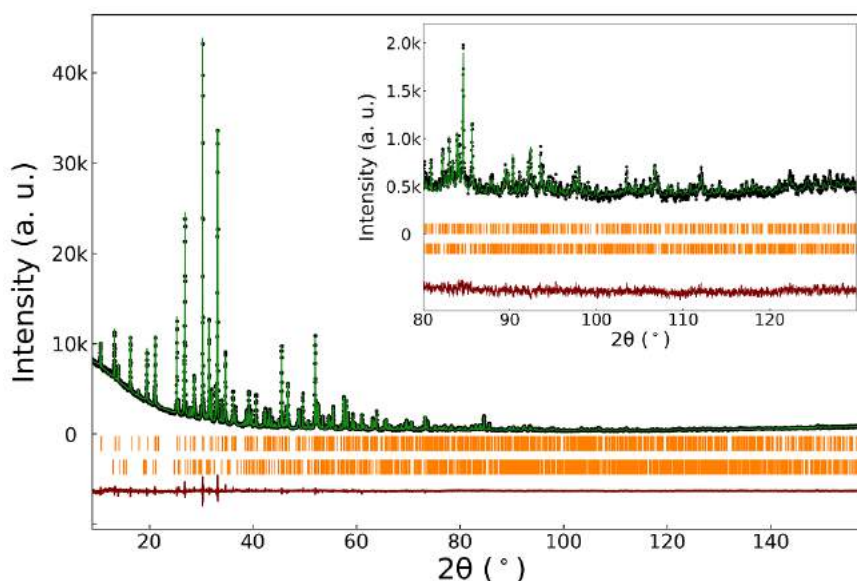
Figure 4.4: Illustration of the Rietveld refinement of $Ca_{10}Cu_{0.5}(VO_4)_7$ sample. The upper orange vertical bars represent peak position of $Ca_{10}Cu_{0.5}(VO_4)_7$ - main phase and the lower vertical bars represent peak position of $Ca_2V_2O_7$- minor phase. R factors are: Rp = 3.17%, Rwp = 4.31% and Rexp = 2.71%. Data were published in [P1]

Specifically, for $Ca_{10.5-x}Co_x(VO_4)_7$, the refined a lattice parameter decreased from 10.81388(4) Å (x = 0) to 10.77187(8) Å (x = 0.66), while the lattice parameter c decreased from 38.02858(15) Å (x = 0) to 37.73979(31) Å (x = 0.66). For $Ca_{10.5-x}Ni_x(VO_4)_7$, the reduction in the lattice parameters was about 0.43% for a and 0.82% for c lattice parameter, while for $Ca_{10.5-x}Cu_x(VO_4)_7$, the reduction was 0.31% for a and 0.44% for c lattice parameter.

The reduction in both lattice parameters a and c, and the consequent decrease in the unit cell volume, with increasing levels of transition metal substitution provides clear evidence of Co, Ni, Cu incorporation into the TCV structure. This reduction can be attributed to differences in the ionic radii of the calcium and transition metal ions. The ionic

radii of Co^{2+}, Ni^{2+}, Cu^{2+} and Ca^{2+} ions have been reported to be 0.65 Å (low spin, CN = 6), 0.69 Å 0.73 Å (CN = 6), and 1.00 Å (CN = 6), respectively [83].
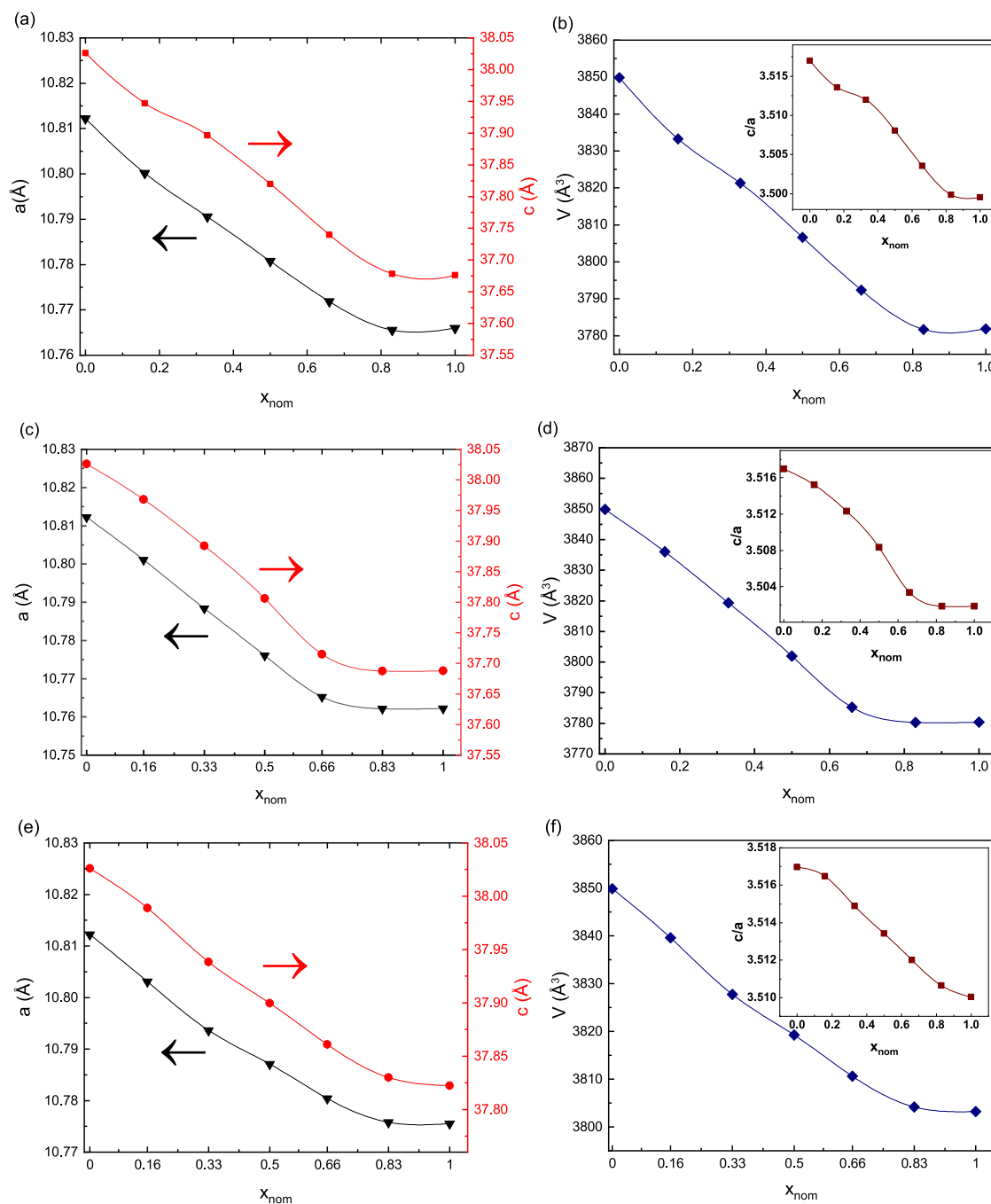
Figure 4.5: Lattice parameters (left), volume (right), and c/a axial ratio (inset) for $Ca_{10.5-x}TM_x(VO_4)_7$ TM = Co (a,b), Ni (c,d), Cu (e,f) versus x content of TM. Lines are simply guides for the eye. Error bars are generally smaller than the size of the symbol. Data for *x* = 0 were published in [P2]. Data for *x* = 0.5 TM = Co, Cu were published in [P1]. Data for TM = Ni were published in [P3]

The contraction observed in unit cell size of $Ca_{10.5-x}TM_x(VO_4)_7$ is analogous to the

behavior of $Ca_3(VO_4)_2:x$Co crystal, where the unit cell volume decreases as the Co_2O_3 content in the initial melt increases [55]. A similar concentration-dependent effect on unit-cell parameters has been observed in isostructural solid solution $Ca_{10.5-x}Cu_x(PO_4)_7$ [8, 84]. This trend of contraction is consistent with the findings of earlier studies on substitution by Mg and Zn ions in TCP [85, 86].

As mentioned before, in $Ca_{10.5-x}TM_x(VO_4)_7$, all samples with x = 0.83 and above shows no reduction in lattice parameters and unit cell volume. This finding indicates a solid solution limit below 0.83. When divalent TM ions completely substitute for Ca^{2+} ions in the TCV lattice, they instead form a secondary phase, $Ca_{2.5}Co_2V_3O_{12}$ and $Ca_{2.5}Ni_2V_3O_{12}$, in two sets of samples ($Ca_{10.5-x}Co_x(VO_4)_7$ and $Ca_{10.5-x}Ni_x(VO_4)_7$) with x$\geq$0.83.

The solubility limit of the material can be estimated from V(x), with values of 0.78(3), 0.72(2) [P3] and 0.75(4) observed for $Ca_{10.5-x}Co_x(VO_4)_7$, $Ca_{10.5-x}Ni_x(VO_4)_7$, and $Ca_{10.5-x}Cu_x(VO_4)_7$, respectively.

There are few studies of solubility limit less than x = 1 for TCV compounds which substituted by Ba^{2+} and Mg^{2+}. In the case of $Ca_{9-x}Ba_xBi(VO_4)_7$, samples with x values ranging from 0 to 0.7 were observed to be single phase, indicating that Bi^{3+} and Ba^{2+} cations were fully incorporated into the host framework [77]. Similarly, the solubility limit of Mg^{2+} substitution in $Ca_{9-x}Mg_xBi(VO_4)_7$ was determined to be x = 0.7 [87].

In previous studies, The solubility limit for TCP which is substituted by divalent ions was expected to be at 1 or higher [6–8]. For instance, the maximum solubility of Mg substitution in $Ca_{10.5-x}Mg_x(PO_4)_7 : Eu^{2+}$ samples was observed at x = 1.5 [6].

To analyze the elemental composition of obtained $Ca_{10.5-x}TM_x(VO_4)_7$ samples, the EDX technique was employed (Figs. A.17-A.22). The results of the EDX analysis indicate that the TMs content closely matches the expected nominal value up to x = 0.66 (refer to Table 4.7). However, for the last two samples with x = 0.83 and 1, a deviation in the transition metal content from the nominal value suggests the presence of a solubility limit at around x = 0.77(2) for TM = Co, x = 0.71(4) for TM = Ni but For TM = Cu, it can not be estimated very precise about solubility limit. The solubility limit which evaluated on basis of $V(x)$ are in reasonable agreement with EDX analysis.

From now, we know the sample with x_{nom} = 0.83 as sample with the composition of x = 0.78(3) for Co substituent, 0.72(2) For Ni substituent and 0.75(4) for Cu substituent.

Table 4.7: Comparison of composition of transition metal obtained by EDX (x_{EDX}) with nominal value (x_{nom})

x_{nom}	x_{EDX}		
	Co	Ni [a]	Cu
0.16	0.19(1)	0.16(2)	0.18(3)
0.33	0.33(1)	0.29(3)	0.33(1)
0.5	0.49(2)[b]	0.48(2)	0.5(8)[b]
0.66	0.67(3)	0.66(4)	0.67(1)
0.83	0.77(2)	0.71(4)	0.84(5)
1	0.81(1)	0.69(2)	1.46(20)

[a] Data were published in [P3]
[b] Data were published in [P1]

4.4   Site occupancy of transition metals

In general, the Rietveld analysis provide a valuable approach for determining the occupancies of substituting ions. However, in the case of substituting ions with similar atomic numbers, such as Ca (Z = 20), Co (Z = 27), Ni (Z = 28), and Cu (Z = 29), the accuracy of the Rietveld method can be limited. Specifically, the Rietveld analysis of X-ray diffraction data using classical sources and a single fixed wavelength cannot precisely determine the percentage of substituted atoms [88]. Trial Rietveld refinements were conducted, considering different sites (M1-M5) for hosting the substituting ions. Through final refinements, it can be concluded that Co, Ni, and Cu tend to occupy the M5 site in the crystal structure. Our model have shown that the occupancy calculated through Rietveld refinement tends to be either underestimated or overestimated for most of samples which is due to the correlation of scattering factor of Ca and TMs (see Figs. 4.6, 4.7, and 4.8).

Divalent ions smaller than calcium are often incorporated into orthophosphate whitlockite type materials by sharing substitutional atoms with calcium at the M5 site. For instance, the M5 site is suggested as the preferential location for copper ion in TCP. Recent studies indicate that up to 15 mol% of Cu^{2+} can be incorporated into the structure of TCP, with Cu^{2+} ions preferring to enter the M5 site. At higher concentrations, the M3 and M2 sites start to host Ca ions after achieving almost full occupancy of the M5 site [8]. Cobalt ions substituted into TCP preferentially occupy the M5 site [89], as do divalent Mg ions [7] and Ni ions [90]. Theoretical calculations based on density functional theory also suggest that Mg^{2+} ions prefer the M5 site [91]. Similarly, manganese ions are found to occupy only M5 sites in the solid solution $Ca_{3-x}Mn_x(PO_4)_2$ [45, 92], with M1 and M2 sites being more preferable after filling the M5 site [93]. Zinc ions also exhibit a preference

for occupying the M5 site in TCP [85].

Furthermore, rare-earth ions occupy different sites depending on their ionic radius, with the M5 site being the main host site for small rare-earth ions substituted for TCV. With increasing rare-earth content, M1 and M2 sites become occupied, while large rare-earth ions enter mainly into the M3 site instead of M5 [94, 95].

In summary, the present study's results are consistent with earlier works on divalent ion substitution, indicating that the M5 site is a host site for divalen (cobalt, nickel and copper) ions. $Ca_{10.5-x}TM_x(VO_4)_7$ compounds can be classified as substitutionally disordered due to the sharing of the M5 site by calcium and transition metal, as well as the vacancy in the M4 site.
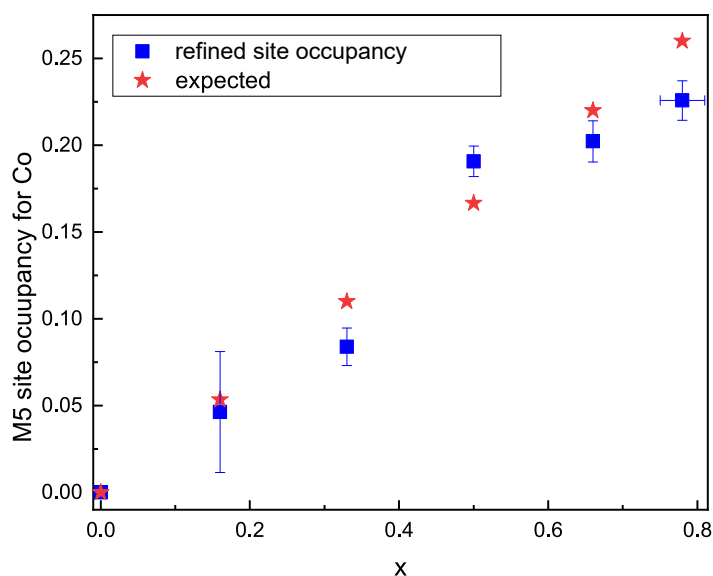
Figure 4.6: Dependence of Co occupancy in M5 site for $Ca_{10.5-x}Co_x(VO_4)_7$ on x

4.5 Interatomic distances

The analysis of atomic coordinates for $Ca_{10.5-x}TM_x(VO_4)_7$ reveals that the addition of transition metals induces only minor changes (approximately 0.001), which are consistent among Co, Ni, and Cu (see appendix A). Therefore, only the set of interatomic distances is presented and discussed. The M-O distance distribution is site-specific for each M1-M5 site, as shown in Figs. 4.9, 4.10 and 4.11.
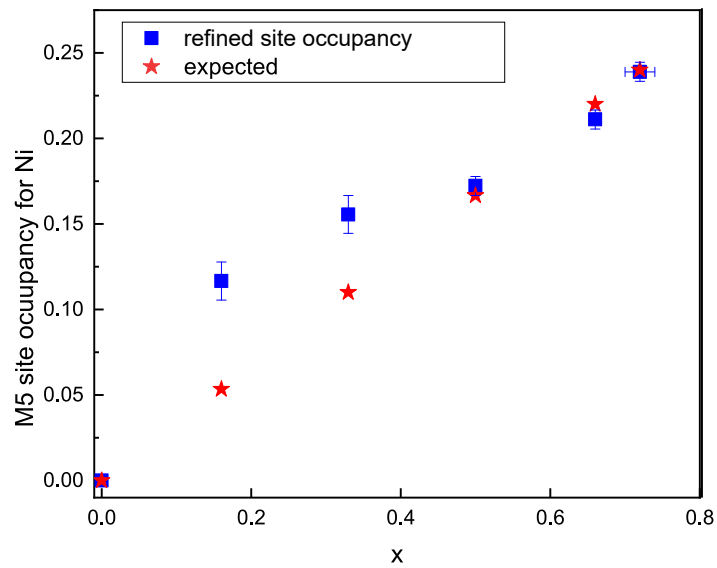
Figure 4.7: Dependence of Ni occupancy in M5 site for Ca$_{10.5-x}$Ni$_x$(VO$_4$)$_7$ on *x*. Data were published in [P3].
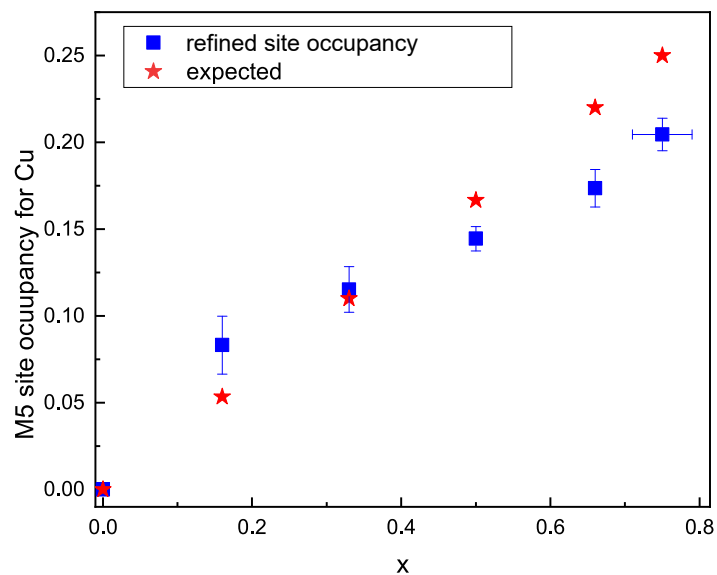
Figure 4.8: Dependence of Cu occupancy in M5 site for Ca$_{10.5-x}$Cu$_x$(VO$_4$)$_7$ on *x*.

$Ca_{10.5-x}Co_x(VO_4)_7$

The M1 site in $Ca_{10.5-x}Co_x(VO_4)_7$ structure has a seven-fold coordination environment, and the average M1-O distances range from 2.44(1) Å ($x = 0$) to 2.45(1) Å ($x = 0.78(3)$). The M2 site has an irregular eight-fold coordination with average M2-O distances of 2.53(1), 2.53(4), 2.53(1), 2.54(1), 2.54(1), and 2.54(1) Å for $x = 0$, $x = 0.16$, $x = 0.33$, $x = 0.5$, $x = 0.66$, and $x = 0.78(3)$ respectively. The M3-O, M1-O, and M2-O distances remain relatively constant despite the increase in Co content. However, there is a reduction in M4-O distances by approximately 4.5%. Additionally, there is a change in the M5 site, which is the only regular polyhedron. The M5-O distances decrease from 2.31(1) ($x = 0$) to 2.13(2) ($x = 0.78(3)$). The presence of Co^{2+} at the M5 site, which has a smaller ionic radius than Ca^{2+}, accounts for the reduction in M5-O distances, thereby supporting the proposed model of the M5 site as a host for the Co substituent.
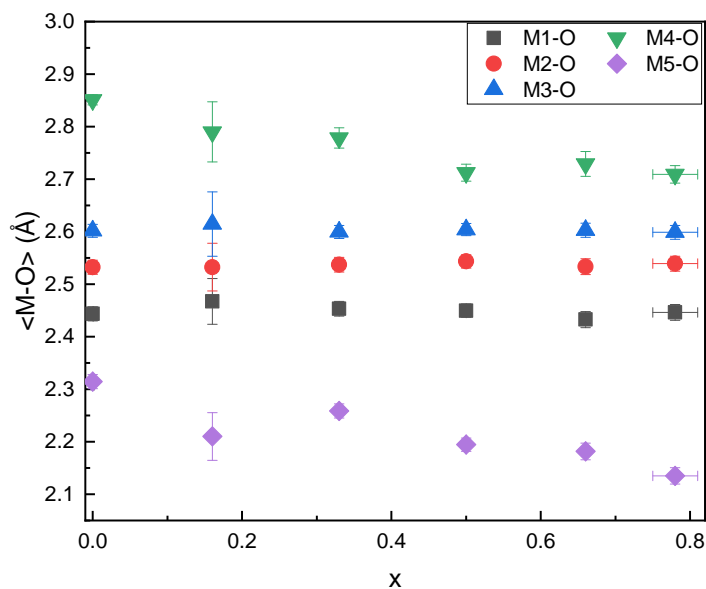
Figure 4.9: Dependence of M-O average interatomic distances on x for the five independent Ca sites of $Ca_{10.5-x}Co_x(VO_4)_7$ structure. Data for $x = 0.5$ were published in [P1].

$Ca_{10.5-x}Ni_x(VO_4)_7$

The M1 site in $Ca_{10.5-x}Ni_x(VO_4)_7$ structure exhibits a 7-fold coordination environment, and the average M1-O distance keep an unchanged value 2.44(1) Å between the $x = 0$ and $x = 0.72(2)$ samples. The M2-O and M3-O distances, as well as M1-O, remain approximately constant regardless of the increasing Ni content (see Fig. 4.10). Conversely, for the M5 site, which represents the only regular polyhedron, there is a distance decrease of approximately 6.8% from $x = 0$ to $x = 0.72(2)$ sample, and thereafter, no changes occur in

distances involving this site. Meanwhile, there is a 4.4% shortening in M4-O distances. This reduction in M5-O is associated with the presence of Ni^{2+} at this site, which has a smaller ionic radius compared to Ca^{2+}. This supports the model of considering the M5 site as a host for the Ni substituent.
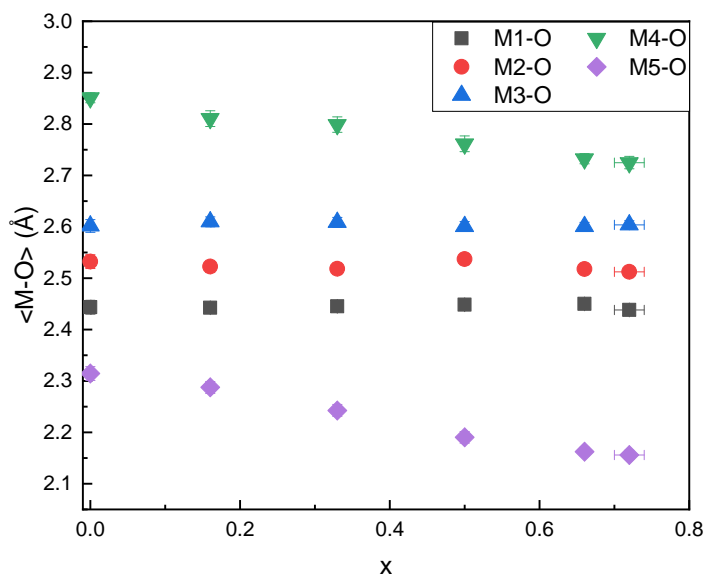
Figure 4.10: Dependence of M-O average interatomic distances on x for the five independent Ca sites of $Ca_{10.5-x}Ni_x(VO_4)_7$ structure. Data were published in [P3].

$Ca_{10.5-x}Cu_x(VO_4)_7$

Based on the results of interatomic distances, the average distances for M1-O, M2-O, M3-O, and M4-O in $Ca_{10.5-x}Cu_x(VO_4)_7$ structure remain relatively constant as the Cu content increases. However, there is a significant reduction of 4.1% in the M5-O distance from x = 0 to x = 0.75(4), indicating the presence of copper at this site.

The M5 site (with CN = 6) exhibits the shortest distances to the oxygen sites and has a regular polyhedron shape for all 3 set of compounds ($Ca_{10.5-x}TM_x(VO_4)_7$ TM = Co, Ni, Cu). The average M4-O distances also reduced by adding transition metal but the percenatge of reduction is less than M5-O distances. As mentioned before, the M4 site is connected to three oxygen atoms with equal bond lengths, forming a planar triangular shape in its environmental geometry. The next three oxygen atoms over the M4-O distances are at further distances, suggesting a weak bond between these oxygen atoms and the cations present at the M4 site. Because of specific environment with oxygen and half occupancy of this site, furthure study is necessary to expalin the reduction of M4-O distances.
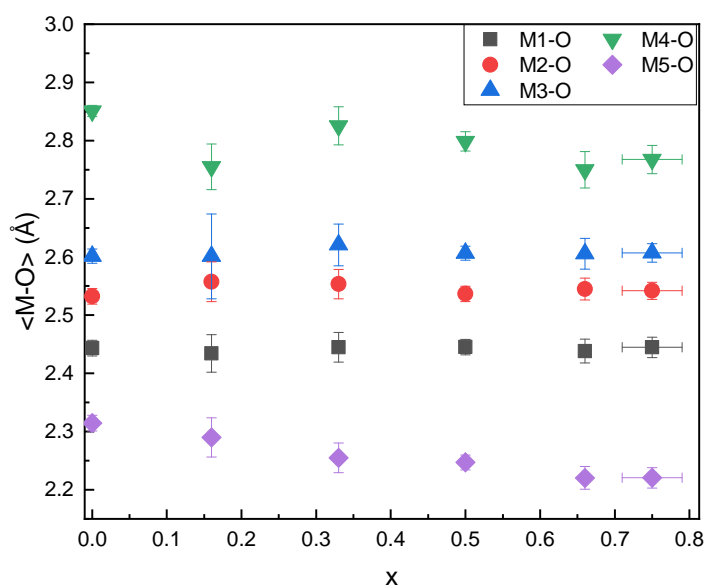
Figure 4.11: Dependence of M-O average interatomic distances on x for the five independent Ca sites of $Ca_{10.5-x}Cu_x(VO_4)_7$ structure. Data for $x = 0.5$ were published in [P1].

As discussed in previous section, transition metals distribution over the five sites was investigated by testing the possible TM localization in all the sites. The result of the occupancy refinements led to the presence of the TM cation only in the M5 site. Moreover, the preference of specific sites by transition metal is at some level determined by the size effect, e.g. the polyhedra with the smallest M-O distances (that it, M5-based) are occupied more favorably by TM than calcium ions, and it was confirmed by analysis of distances, the presence of Ni and Cu at M5 site for $Ca_{2.9}Me_{0.1}(PO_4)_2$ compounds [90]. Analysis of interatomic distances of Mn-substituted $Ca_3(PO_4)_2$ also showed a decrease of M5-O [92]. Further investigation executed in the open chemistry database (OChemDb), the free online portal designed for analyzing crystal-chemical information [96], whose obtained statistics are depicted in Fig. 4.12; this revealed that the most recurrent data for Co-O distances is 2.08 Å for Ni-O distances is 2.06 Å and Cu-O distances is 1.94 Å which are close to the the value which experimentally found in the M5-O distances for $Ca_{10.5-x}TM_x(VO_4)_7$.
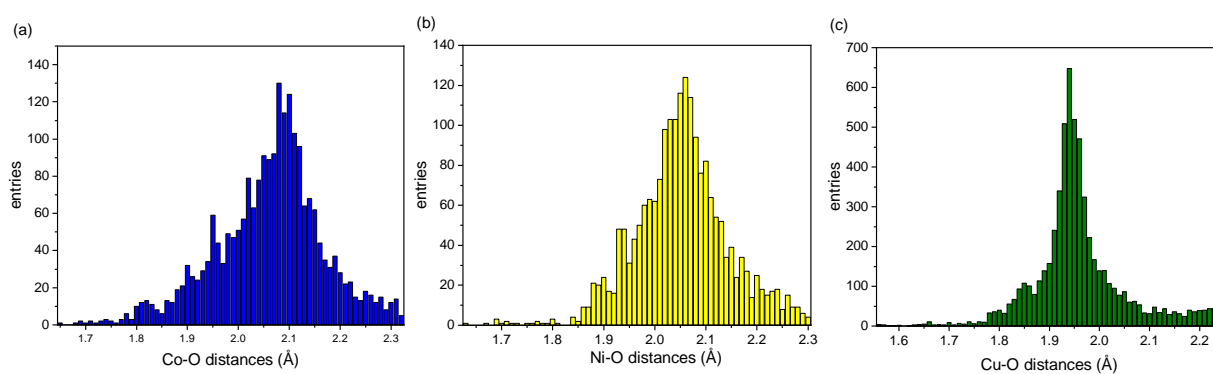
Figure 4.12: Bond distances investigation within inorganic structures performed via open chemistry database (OChemDb) for divalent ions Co-O (a), Ni-O (b), and Cu-O (c).

Chapter 5

Structure study of $Ca_{10.5-x}TM_x(VO_4)_7$ at high temperature

5.1 Temperature evolution of lattice parameters

In order to elucidate the change of temperature behavior of $Ca_{10.5-x}TM_x(VO_4)_7$, high temperature diffraction experiment were conducted for selected samples, $Ca_3(VO_4)_2$, $Ca_{10.5-x}Co_x(VO_4)_7$ (x=0.5, 0.66, 0.78(3)), $Ca_{10.5-x}Ni_x(VO_4)_7$ (x=0.16, 0.33, 0.5, 0.66, 0.72(2)) and $Ca_{10.5-x}Cu_x(VO_4)_7$ (x=0.5, 0.66, 0.75(4)). Phase analysis demonstrate that there is no sign of phase transition. The procedures for refinement were carried out as described in chapter 4. However, the atomic positions were fixed to the value obtained at room temperature because of low resolution. The temperature dependent behavior of lattice parameters are presented in Figs. 5.1-5.7
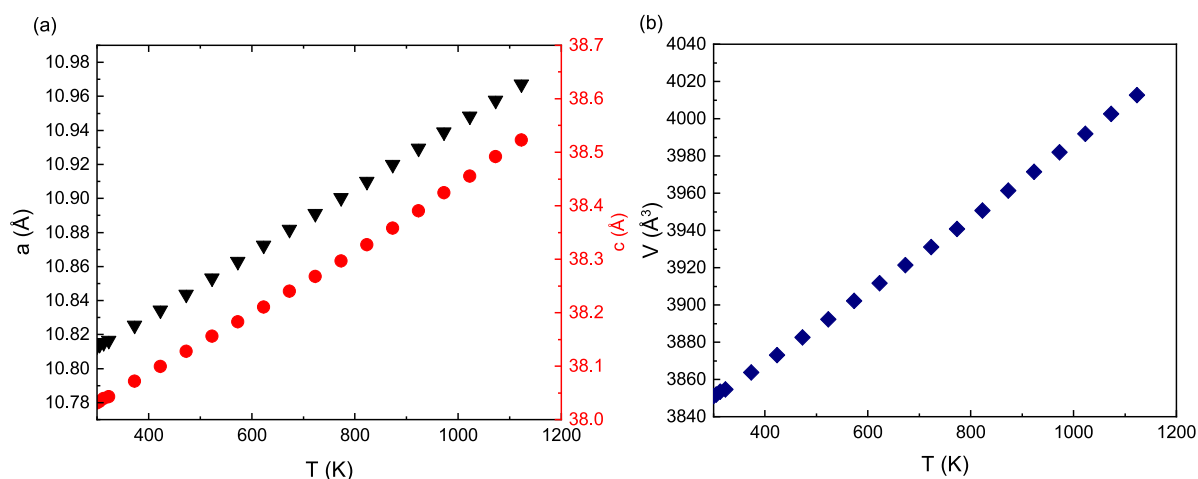
Figure 5.1: Temperature evolution of lattice parameters (a) and unit cell volume (b) for $Ca_3(VO_4)_2$. Data were published in [P2].
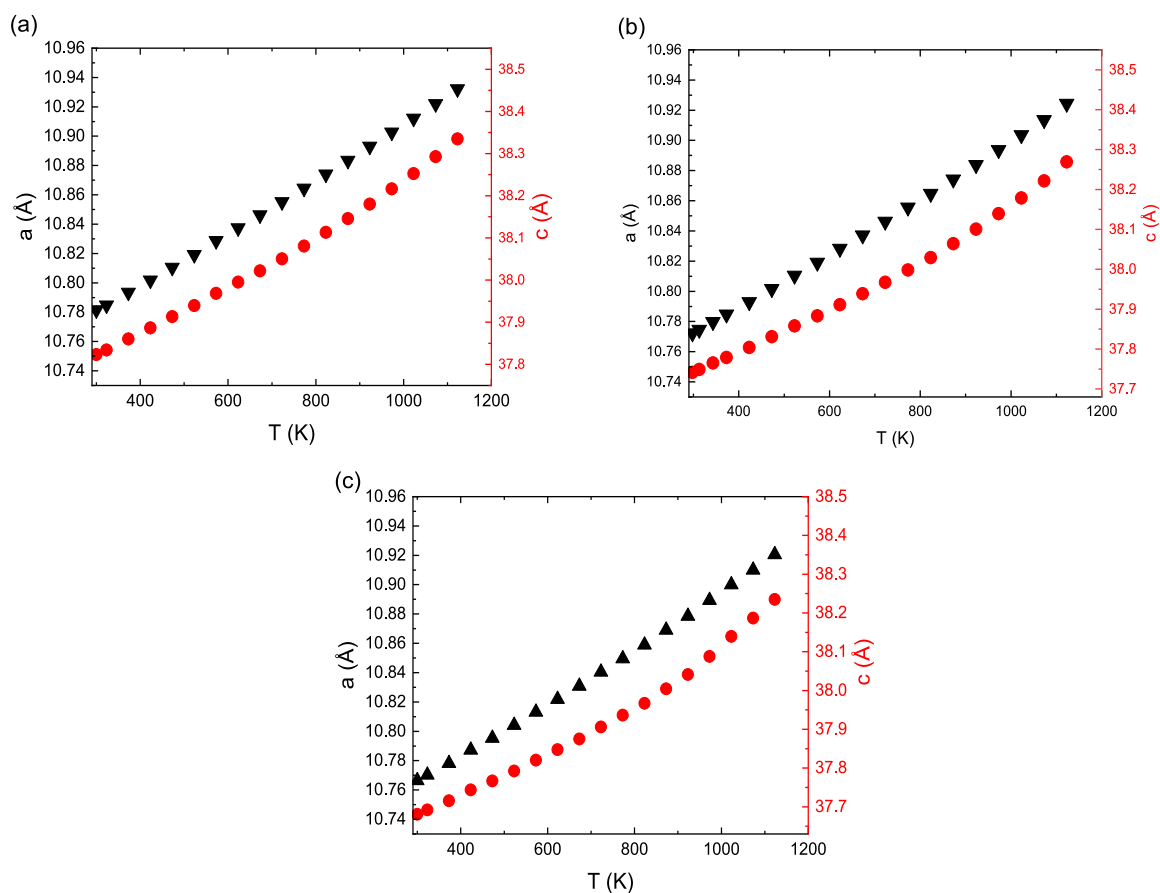
Figure 5.2: Temperature evolution of lattice parameters for Ca$_{10.5-x}$Co$_x$(VO$_4$)$_7$ $x = 0.5$ (a), 0.66 (b), 0.78(3) (c). Data for $x = 0.5$ from RT till 800 were published in [P1].
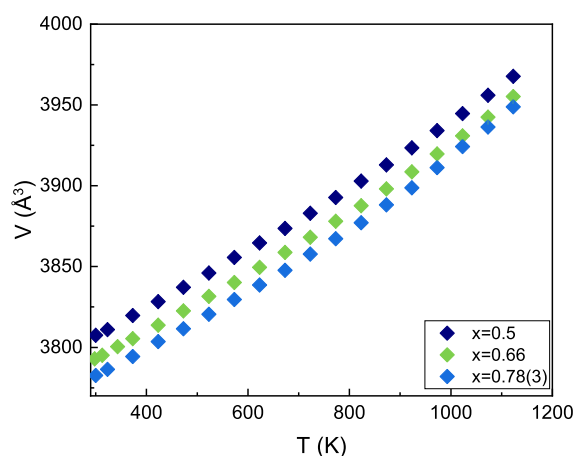
Figure 5.3: Temperature evolution of unit cell volume for Ca$_{10.5-x}$Co$_x$(VO$_4$)$_7$ $x = 0.5$, 0.66, 0.78(3). Data for $x = 0.5$ from RT till 800 were published in [P1].
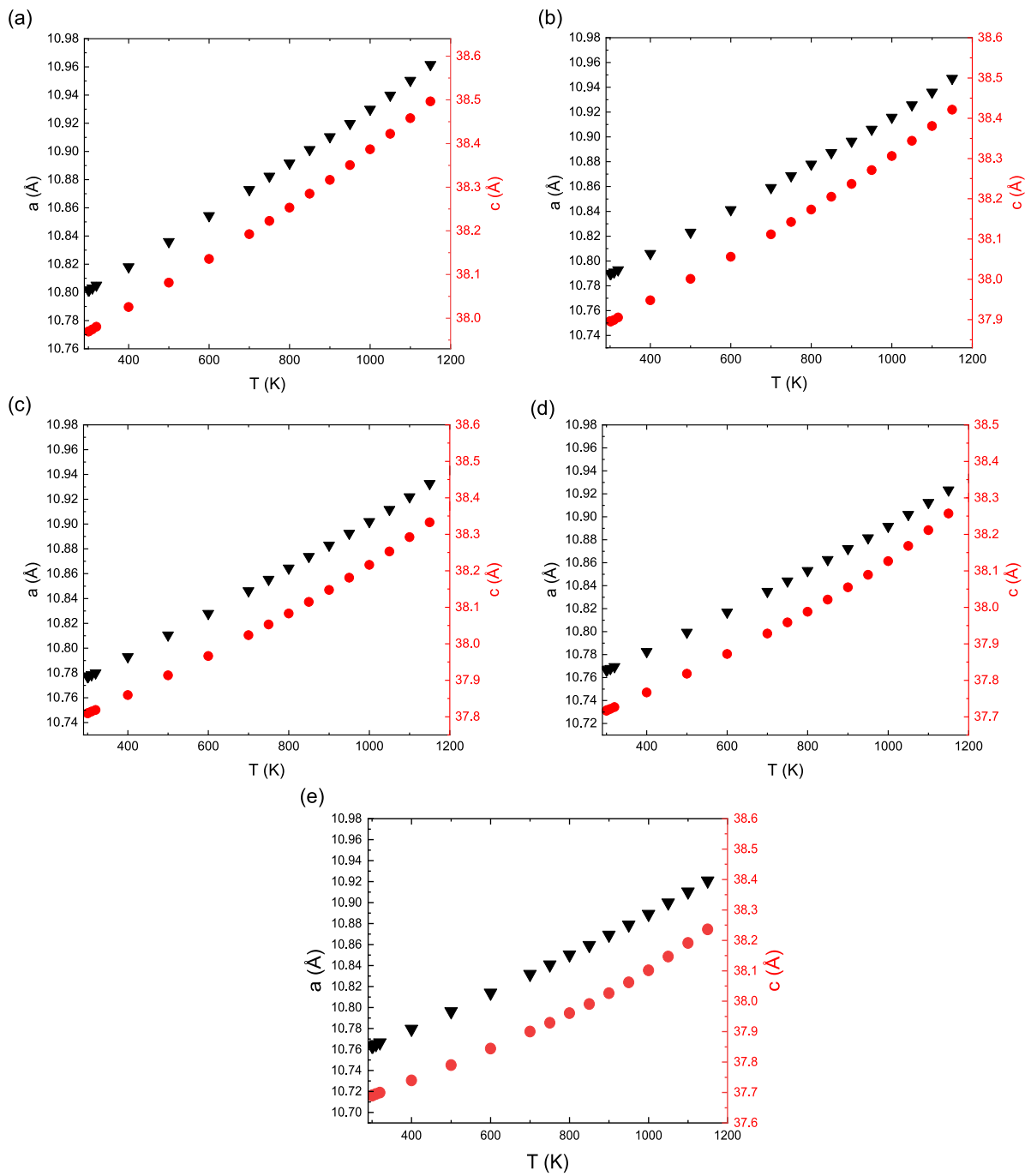
Figure 5.4: Temperature evolution of unit cell parameters for $Ca_{10.5-x}Ni_x(VO_4)_7$ $x = 0.16$ (a), 0.33 (b), 0.5 (c), 0.66 (d), 0.72(2) (e). Data were published in [P3].
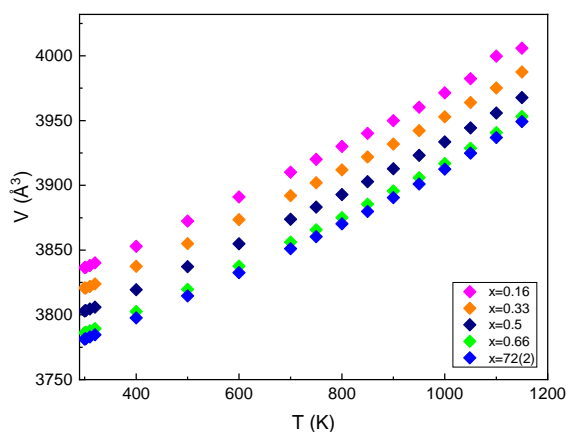
Figure 5.5: Temperature evolution of unit cell volume for Ca$_{10.5-x}$Ni$_x$(VO$_4$)$_7$ x = 0.16. 0.33, 0.5, 0.66, 0.72(2). Data were published in [P3].
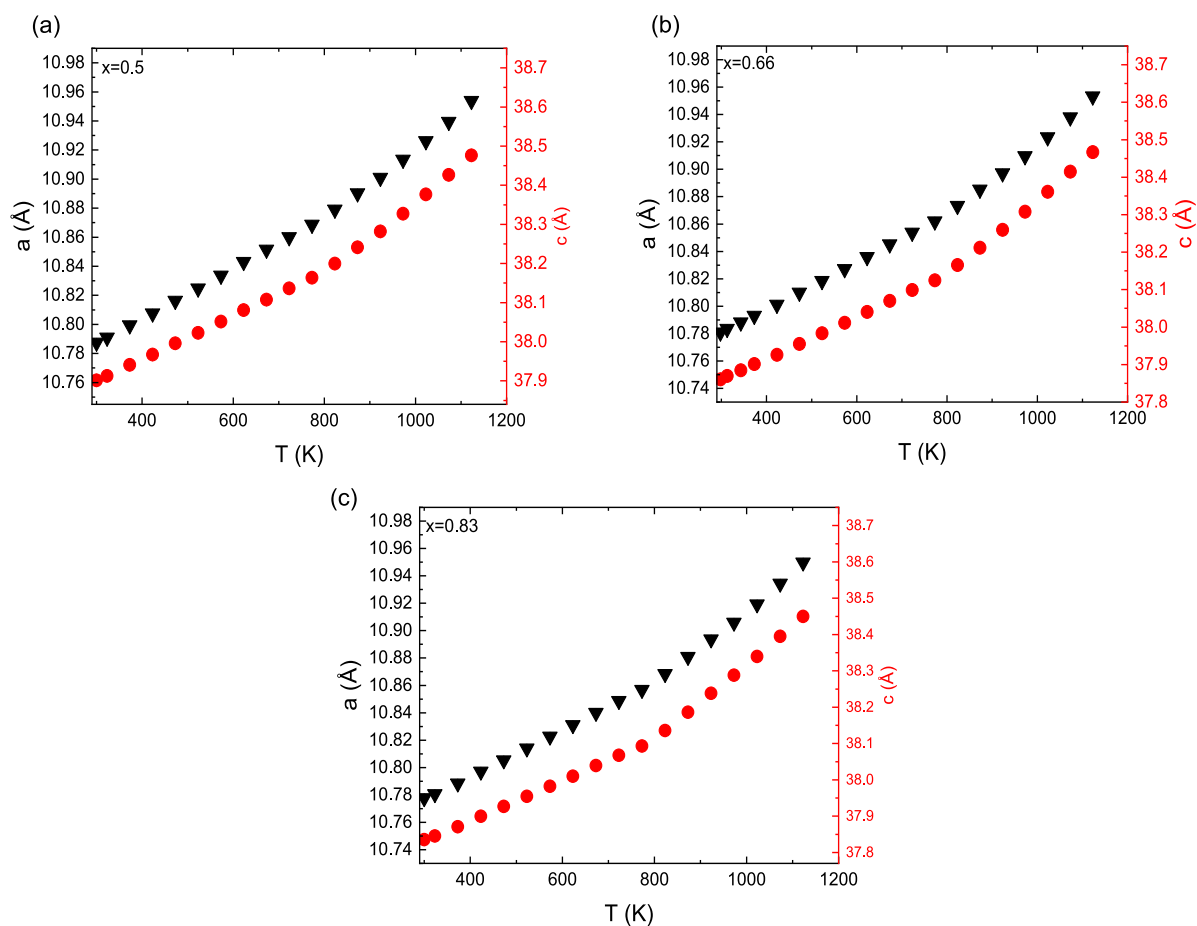
Figure 5.6: Temperature evolution of lattice parameters for Ca$_{10.5-x}$Cu$_x$(VO$_4$)$_7$ x = 0.5 (a), 0.66 (b), 0.75(4) (c). Data for x = 0.5 from RT till 800 were published in [P1].
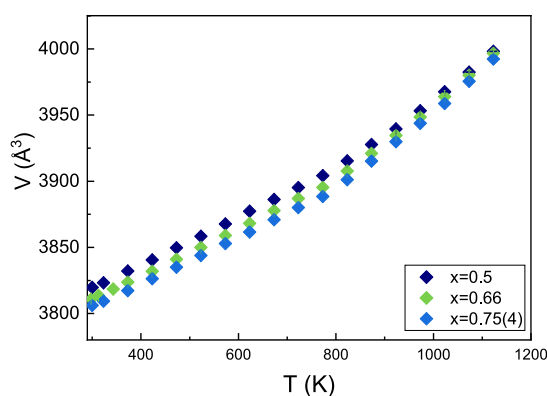
Figure 5.7: Temperature evolution of unit cell volume for $Ca_{10.5-x}Cu_x(VO_4)_7$ $x = 0.5, 0.66,$ $0.75(4)$. Data for $x = 0.5$ from RT till 800 were published in [P1].

All compounds show a consistent expansion with temperature evolution for lattice parameters (a, c) and unit cell volume up to around 800 K. At higher temperatures, notable changes occur in the temperature dependence slope of the a and c lattice parameters.

The axial ratios (as shown in Figs. 5.8, 5.9, 5.10 and 5.11) provides a straightforward means to observe this week feature. The trend in the c/a(T) ratio is such that it decreases for all compounds from room temperature until approximately 800 K. Beyond this temperature range, the slope of the c/a(T) is changed which indicating that , the lattice parameter a increases at a faster rate than the lattice parameter c.
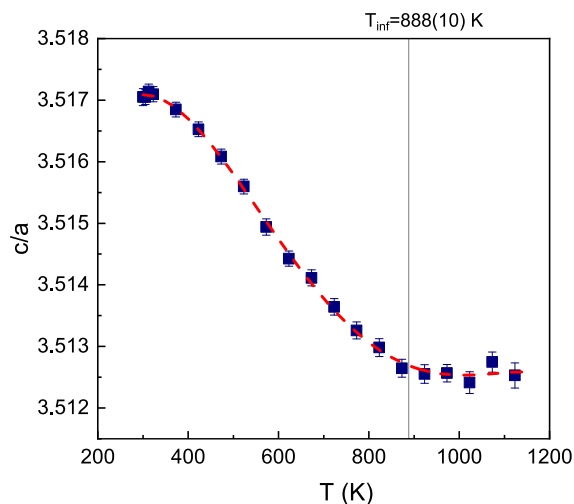
Figure 5.8: Temperature evolution of axial ratio for $Ca_3(VO_4)_2$. Data were published in [P2].
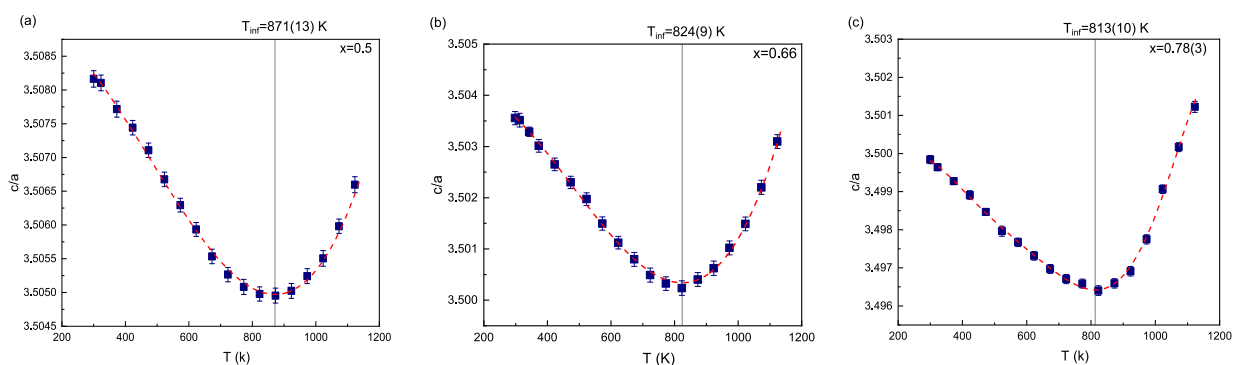
Figure 5.9: Temperature evolution of axial ratio for Ca$_{10.5-x}$Co$_x$(VO$_4$)$_7$. $x = 0.5$ (a), 0.66 (b), 0.78(3) (c). Data for $x = 0.5$ from RT till 800 were published in [P1].
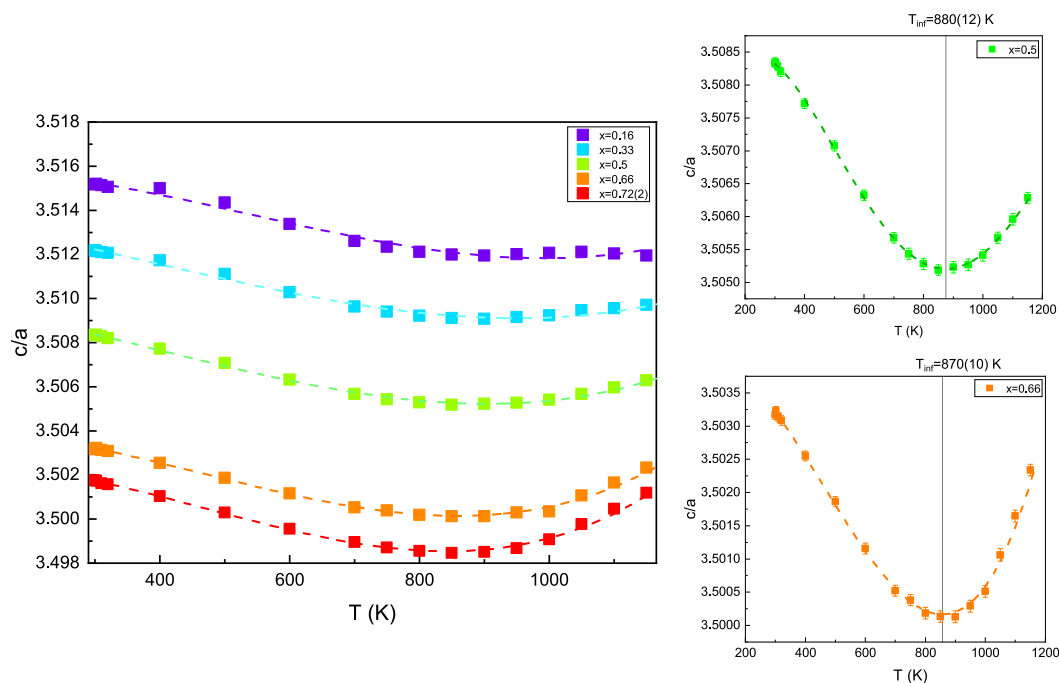
Figure 5.10: Temperature evolution of axial ratio for Ca$_{10.5-x}$Ni$_x$(VO$_4$)$_7$. Adapted with permission from [P3].
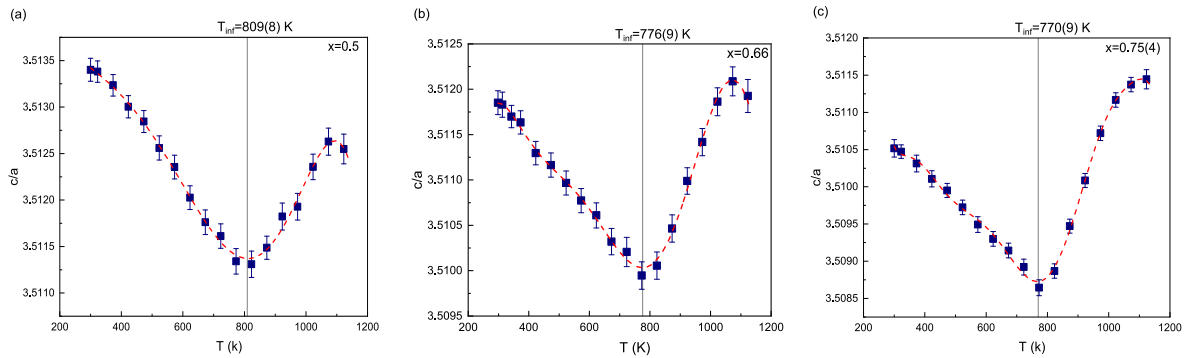
Figure 5.11: Temperature evolution of axial ratio for $Ca_{10.5-x}Cu_x(VO_4)_7$ $x = 0.5$ (a), 0.66 (b), 0.75(4) (c). Data for $x = 0.5$ from RT till 800 were published in [P1].

In general, the non-linear behavior of lattice parameters in whitlockite type materials suggests complex reordering in structure occur with temperature. The inflection temperature (T_{inf}) marks the temperature at which these changes in lattice parameters occur. Inflection temperature decrease by increasing the content of transition metals. For instance, $Ca_{10}Co_{0.5}(VO_4)_7$ exhibits T_{inf} at approximately 871 K, whereas for $Ca_{9.72}Co_{0.78}(VO_4)_7$, T_{inf} occurs at 813 K. A similar trend is observed in copper and nickel samples (Figs. 5.10,5.11), with T_{inf} estimated at 905 K and 870 K for $Ca_{10.34}Ni_{0.16}(VO_4)_7$ and $Ca_{9.84}Ni_{0.66}(VO_4)_7$, respectively. However, these approximations require further studies with smaller temperature steps for more accurate determination of T_{inf}.

5.2 Thermal expansion

The Laurent polynomial is widely used to estimate unit cell size variation with temperature in numerous materials, including minerals of complex structures. This approximation is particularly applicable at temperatures above RT. Although the polynomial is suitable for a (routine) behavior, in some cases the Lagrangian approach is a good solution in cases where one wishes to determine the variation without applying any model. In the case of the whitlockite type material investigation in this thesis, a combined approach is adopted. Specifically, the behavior below the inflection point is modeled using the Laurent polynomial (Eq. 5.1), while the Lagrange interpolation approach (Eq. 5.2) is utilized for the entire temperature range to prevent any bias from the model. Laurent polynomial extrapolation above the inflection temperature (T_{inf}) predict the hypothetical behavior of quenched samples, which are not anticipated to display any anomalous behavior above T_{inf}.

$$L(T) = A + BT + C/T \tag{5.1}$$

$$\begin{aligned} \alpha_n(T_n) = (&\frac{T_n - T_{n+1}}{(T_{n-1} - T_n)(T_{n-1} - T_{n+1})} L_{n-1} + \frac{2T_n - T_{n-1} - T_{n+1}}{(T_n - T_{n-1})(T_n - T_{n+1})} L_n \\ &+ \frac{T_n - T_{n-1}}{(T_{n+1} - T_{n-1})(T_{n+1} - T_n)} L_{n+1}) \frac{1}{L_n} \end{aligned} \tag{5.2}$$

Thermal expansion coefficients of lattice parameters are presented in Figs. 5.13, 5.14, and 5.15. The majority of TEC values calculated using Lagrangian interpolation are encompassed by the lines depicted through the Laurent polynomial model.

The values of linear and volumetric thermal expansion coefficients from room temperature up to approximately 800–900 K do not change significantly for all compounds. The value of TEC along *a* direction is slightly bigger than along *c* direction, However, above inflection temperature, TEC in *c* direction increase faster than *a* direction.

Above inflection temperature, thermal expansion in *c* direction of zero sample $(Ca_3(VO_4)_2)$ approximately equal to that in *a* direction.
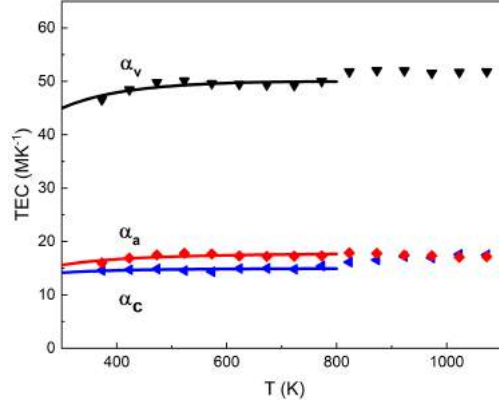
Figure 5.12: Temperature evolution of TEC for $Ca_3(VO_4)_2$ using Lagrangian interpolation. Solid line represent the polynomial model. Data were published in [P2].
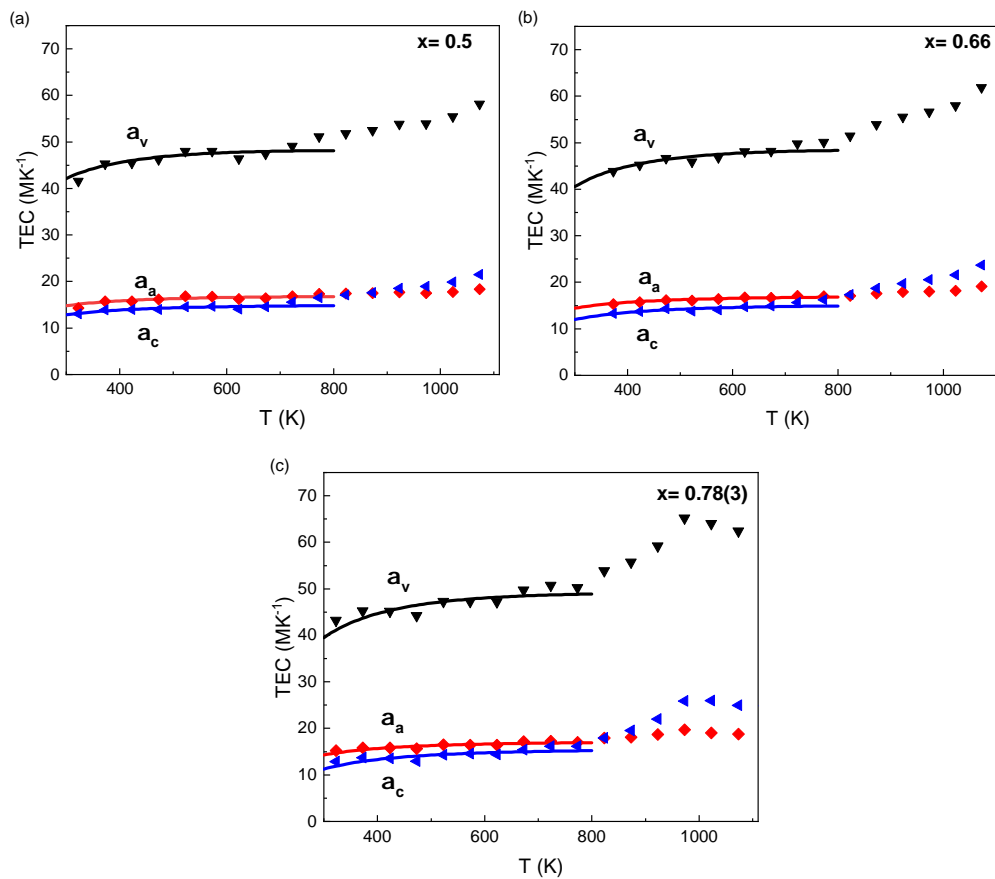
Figure 5.13: Temperature evolution of TEC for $Ca_{10.5-x}Co_x(VO_4)_7$ $x = 0.5$ (a), 0.66 (b), 0.78(3) (C) using Lagrangian interpolation. Solid line represent the polynomial model. Data for $x = 0.5$ from RT till 800 were published in [P1].
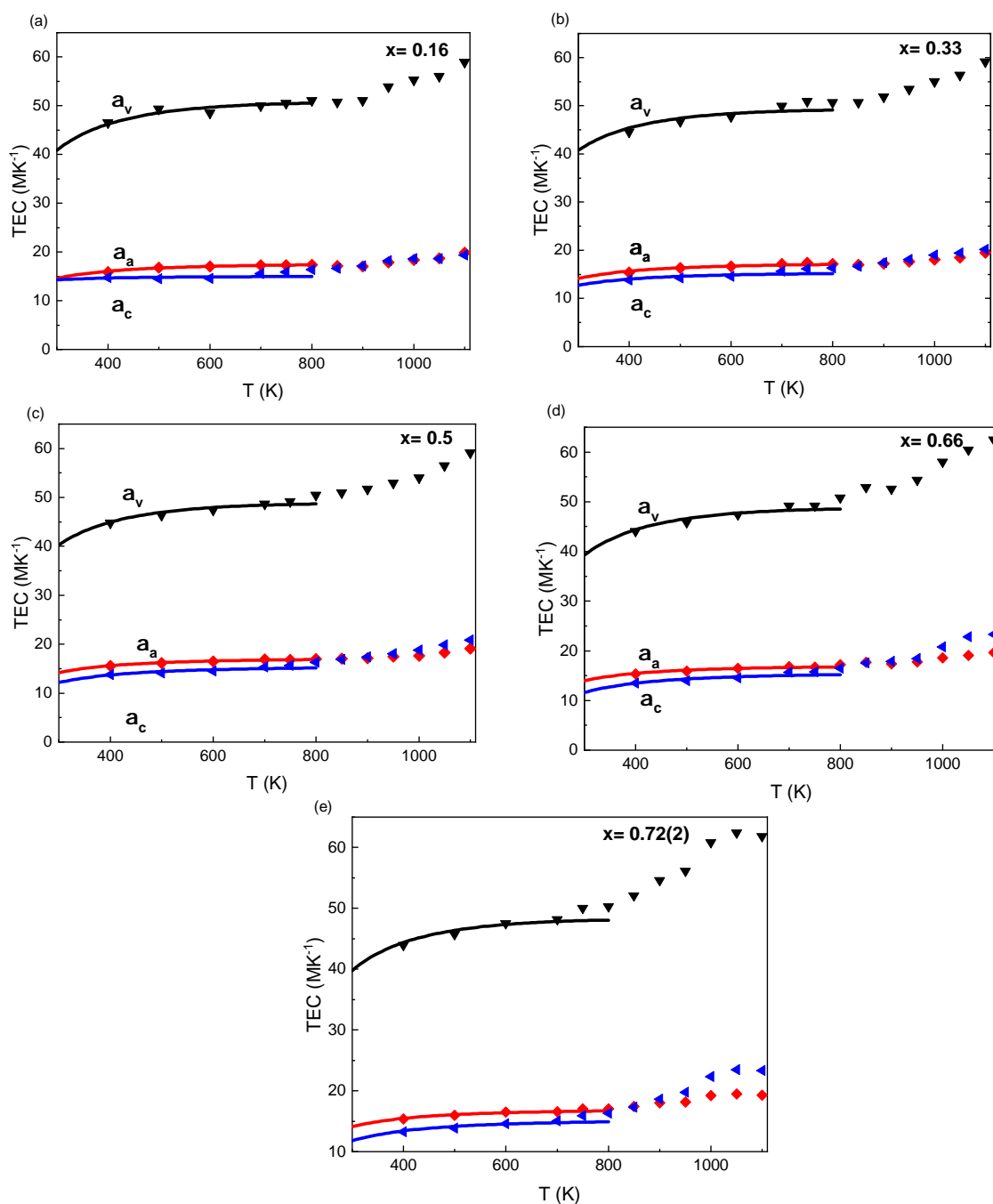
Figure 5.14: Temperature evolution of TEC for unit-cell parameters of $Ca_{10.5-x}Ni_x(VO_4)_7$ $x = 0.16$ (a), 0.33 (b), 0.5 (C), 0.66 (d), 0.72(2) (e) using Lagrangian interpolation. Solid line represent the polynomial model. [P3].

5.3. Crystal structure of Ca$_{10}$Co$_{0.5}$(VO$_4$)$_7$ *and* Ca$_{10}$Cu$_{0.5}$(VO$_4$)$_7$ *as function of temperature*

57
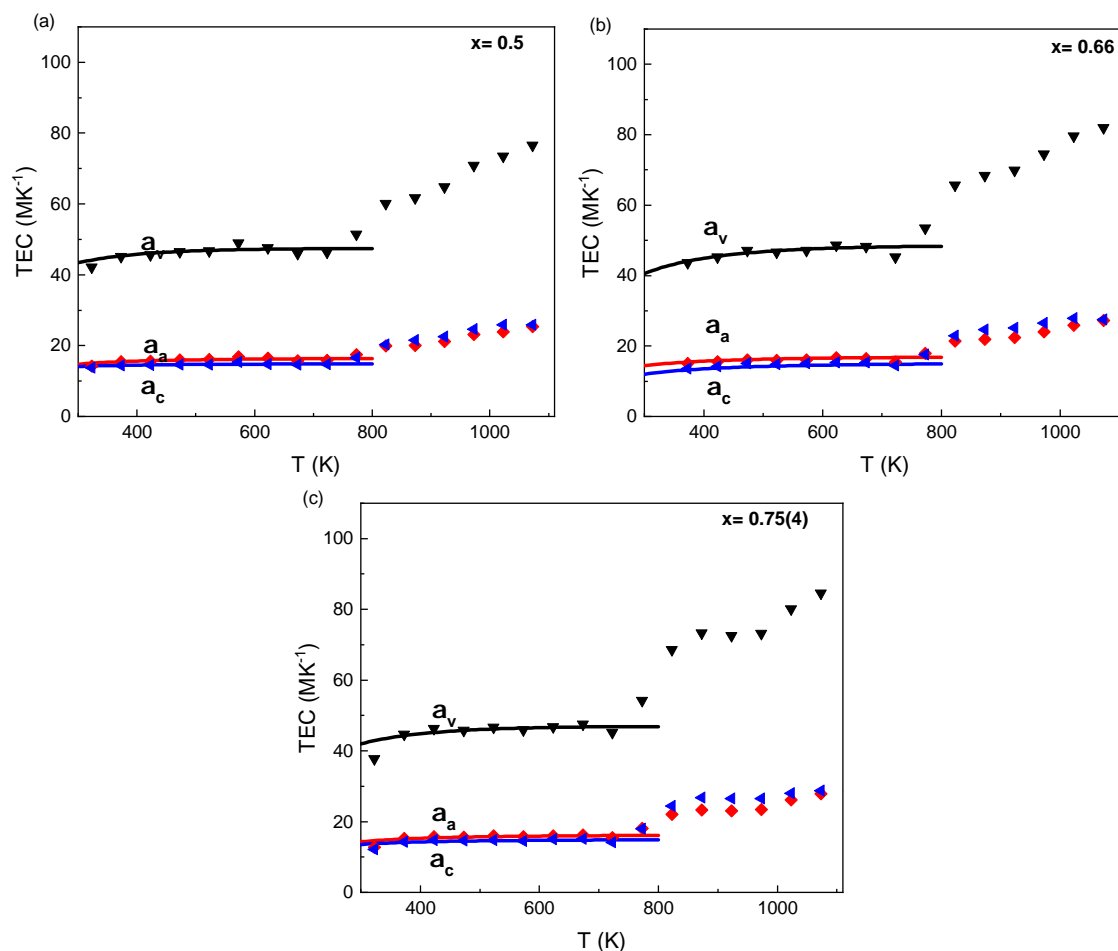
Figure 5.15: Temperature evolution of TEC for Ca$_{10.5-x}$Cu$_x$(VO$_4$)$_7$ x = 0.5 (a), 0.66 (b), 0.75(4) (C) using Lagrangian interpolation. Solid line represent the polynomial model. Data for x = 0.5 from RT till 800 were published in [P1].

5.3 Crystal structure of Ca$_{10}$Co$_{0.5}$(VO$_4$)$_7$ and Ca$_{10}$Cu$_{0.5}$(VO$_4$)$_7$ as function of temperature

To understand the behavior of transition metal at high temperature, two samples (Ca$_{10}$Co$_{0.5}$(VO$_4$)$_7$ and Ca$_{10}$Cu$_{0.5}$(VO$_4$)$_7$) are selected to measure at ID22 beamline in temperature range 300-1100 K.. In contrast to laboratory data, synchrotron data enabled the refinement of the crystal structure of Ca$_{10.5-x}$TM$_x$(VO$_4$)$_7$ at high temperatures due to better resolution. As the temperature increases, the diffraction peaks exhibit a slight shift towards the low-angle side due to the ongoing expansion of the lattice (see Fig. 5.16).
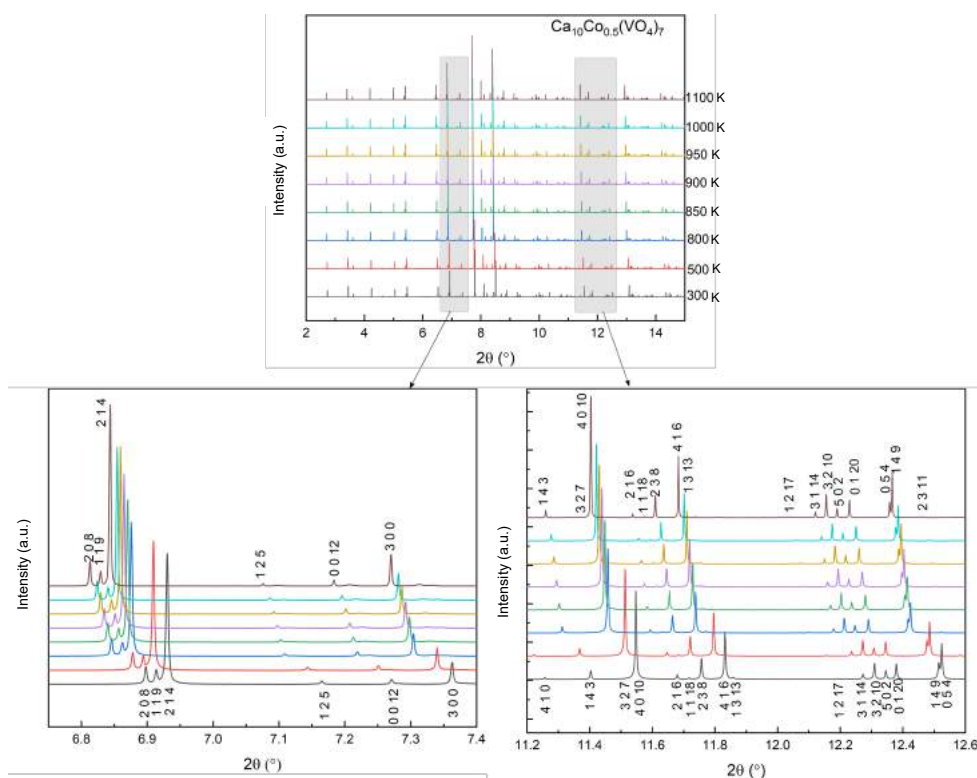
Figure 5.16: x-ray diffraction of $Ca_{10}Co_{0.5}(VO_4)_7$ at high temperature with magnification of high and low angles.

The refinement procedures were conducted according to the previously described but for these two sample, all atomic positions were refined. The quality of refinements is illustrated for $Ca_{10}Cu_{0.5}(VO_4)_7$ at 850 K (Fig. 5.17) as representative example. Magnification of high angles are presented in Fig. B.1. The analysis revealed the presence of a second phase related to $Ca_2V_2O_7$ exhibits a consistent quantity as the temperature increases.

The behavior of unit cell size are in good agreement with laboratory data for these two samples (Fig. 5.18).

The Rietveld refinement was used to determine the occupancy at M5 sites for each temperature. The stability of the occupancy scheme remains unchanged up to approximately 850 K for $Ca_{10}Cu_{0.5}(VO_4)_7$, and up to about 900 K for $Ca_{10}Co_{0.5}(VO_4)_7$ (Fig. 5.19). However, above these temperatures, a reduction in occupancy at M5 site was observed, which may indicate that a small quantity of transition metals occupies another sites. Different models by considering M1, M2 and M3 sites were tried to host for Ni ions but due to the minimal difference in the electronic structure of Co, Ni, and Cu, as well as calcium, it is not possible to determine which site (M1-M3) serves as the host for these transition
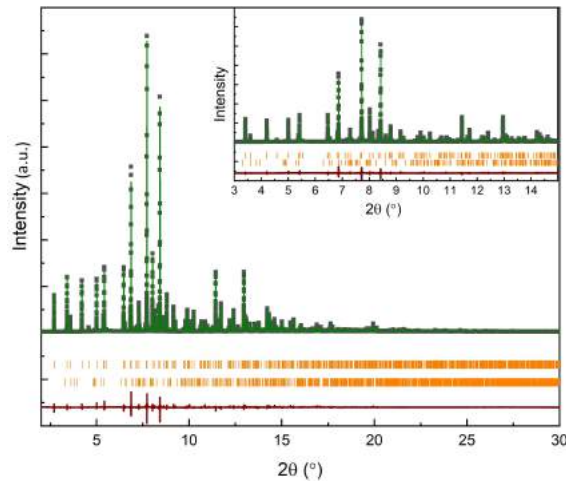
Figure 5.17: Illustration of Rietveld refinement of $Ca_{10}Cu_{0.5}(VO_4)_7$ at 850 K .
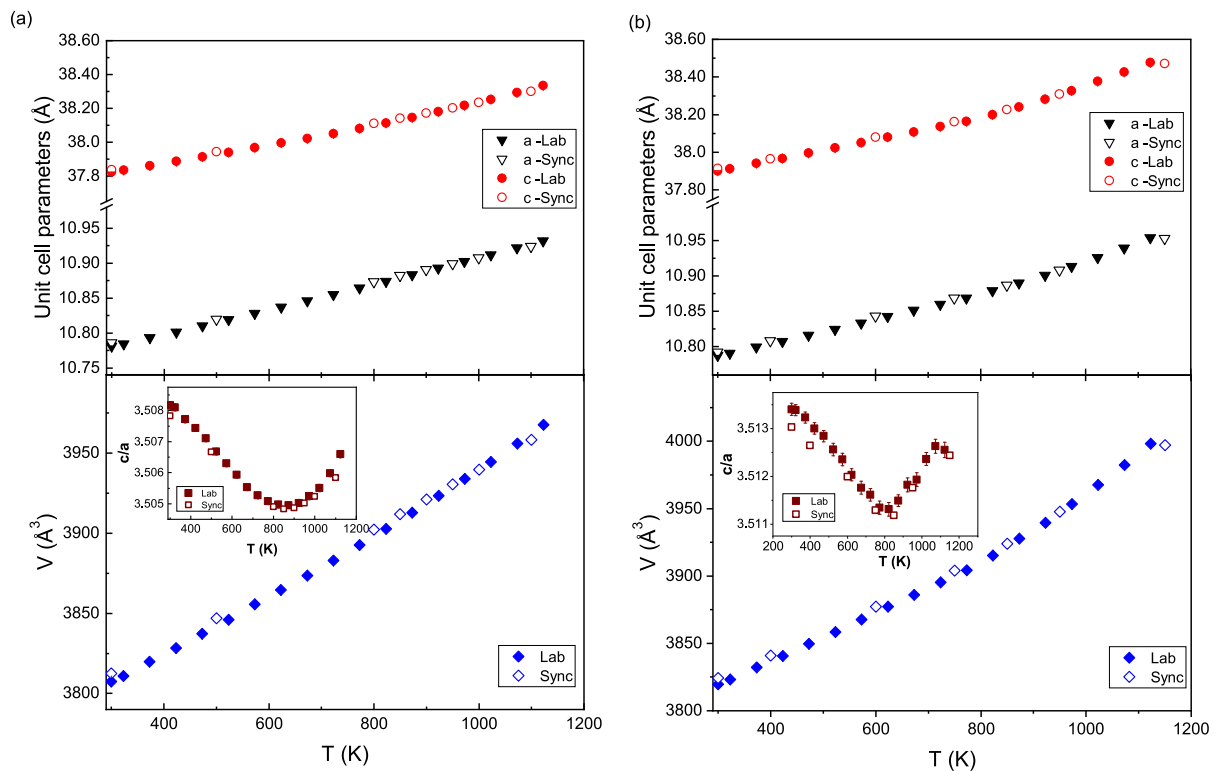
Figure 5.18: Temperature evolution of unit cell parameters (top), volume (bottom) and c/a axial ratio (inset) for $Ca_{10}Co_{0.5}(VO_4)_7$ (a) and $Ca_{10}Cu_{0.5}(VO_4)_7$ (b). Solid symbols correspond to the laboratory experiment and empty symbols to the synchrotron experiment.

metals. Consequently, further studies are required to identify the exact location of the transition metals at higher temperatures.

The process of cation rearrangement with increasing temperature is a hypothetical source that can lead to anomalies in lattice parameter and thermal expansion. Similar anomalies have been reported in other oxides with mixed crystallographic site occupation, such as Ca$_3$Eu$_2$(BO$_3$)$_4$ [97, 98]. Specifically, changes in cation ordering, particularly in the fractional occupation of Eu^{3+} at sites M1 and M3, were observed above 923 K.
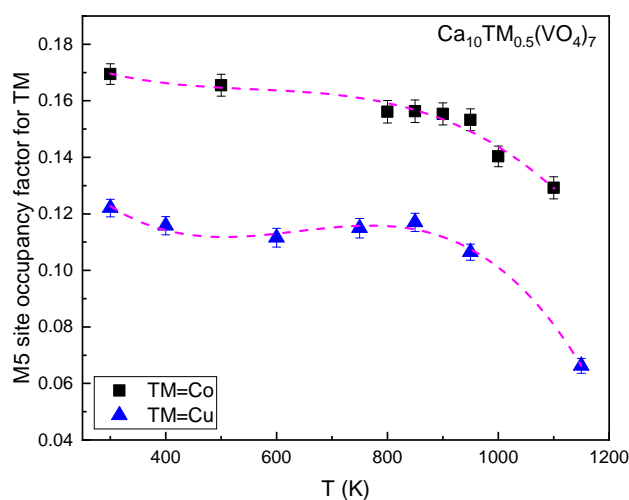
Figure 5.19: Variation of occupancy at M5 site with temperature for Ca$_{10}$TM$_{0.5}$(VO$_4$)$_7$ TM= Co, Cu

Chapter 6

Structure study of $Ca_{10.5-x}TM_x(VO_4)_7$ at low temperature

6.1   Temperature evolution of lattice parameters

Three samples were chosen for low temperature measurement at the ESRF synchrotron: $Ca_3(VO_4)_2$, $Ca_{10}Ni_{0.5}(VO_4)_7$ and $Ca_{10}Cu_{0.5}(VO_4)_7$. The diffraction patterns demonstrate that there was no indication of any changes in symmetry during the investigated temperature range (4 - 280 K), thus confirming the stability of the phase (see Fig. 6.1).
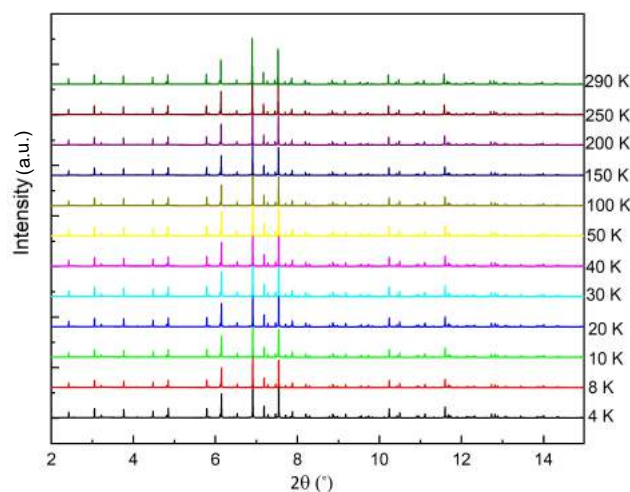
Figure 6.1: X-ray diffraction of $Ca_{10}Cu_{0.5}(VO_4)_7$ at low temperatures.

The refinement procedures were carried out following the methodology described in chapter 4. Illustration of the Rietveld refinement for $Ca_{10}Ni_{0.5}(VO_4)_7$ at a temperature of 100 K is presented Fig. 6.2.

Behavior of lattice parameters as function of temperature were obtained for all selected compounds. The results of the analysis are displayed in Figs. 6.3, 6.4, and 6.5,
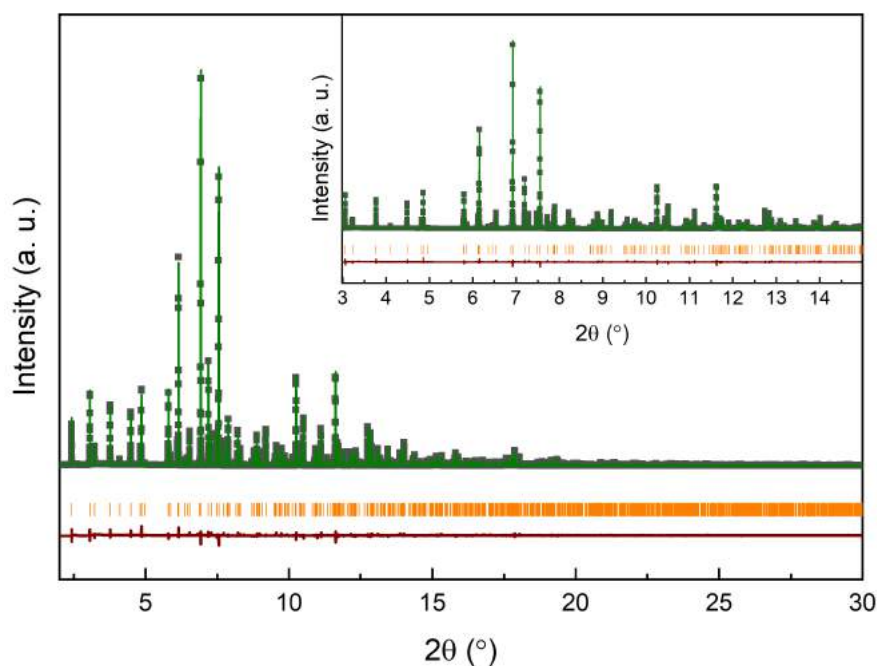
Figure 6.2: Illustration of Rietveld refinement of $Ca_{10}Ni_{0.5}(VO_4)_7$ at 100 K.

which provide detailed graphical representations of the observed changes and trends in lattice parameters across the range of temperatures studied.

Investigation of the low temperature dependence of lattice parameters revealed that, for all the compounds we studied, there is an expansion for the *a* lattice parameter (1%) and unit cell volume (3%) datasets (Figs. 6.3-a&c , 6.4-a&c, and 6.5-a&c). However, in the case of the *c* lattice parameter, we observed a reduction from 4 K to 30 K for $Ca_{10}Ni_{0.5}(VO_4)_7$ and the same reduction from 4 K to 50 K for $Ca_{10}Cu_{0.5}(VO_4)_7$ and then, followed by a similar increase with the evolution of temperature up to 290 K. These distinctive features are particularly visible when we consider the axial ratios (c/a) for each compound, as illustrated in Figs. 6.3-c, 6.4-c, and 6.5-c. This behavior is possibly due to change of polyhedra's vibration (transversal to longitudinal vibration) at very low temperature.

The heating of three samples from 4 K to 290 K results in minimal changes to the average M-O bond lengths, as demonstrated in Figs. 6.6, 6.7, and 6.8. There is no discernible trend observed in the variations of bond lengths across different sites with increasing temperature. However, slight changes in the order of 0.001 Å are observed for different oxygen atoms at specific sites, as documented in Appendix C.

These observations suggest that the irregular shape of polyhedra may be responsible
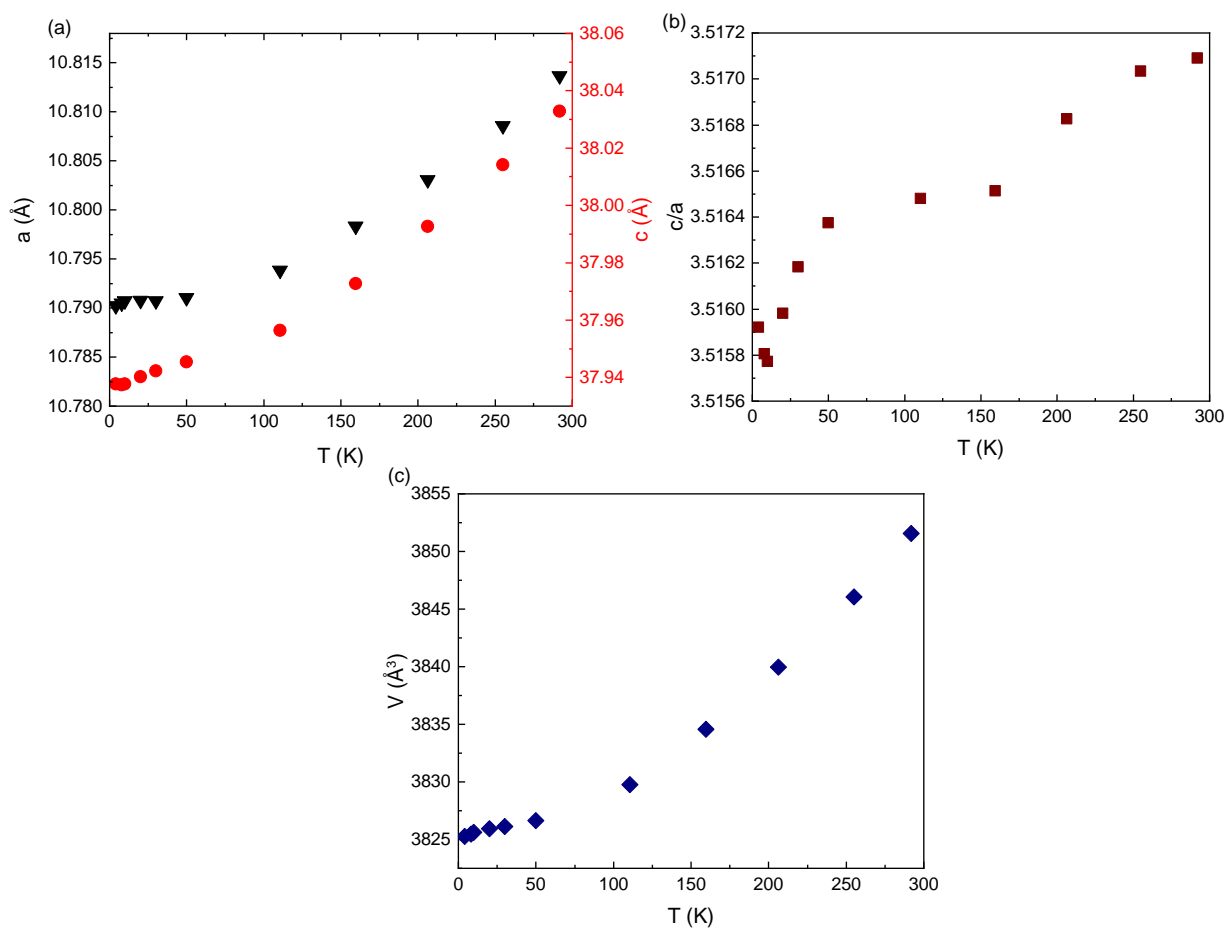
Figure 6.3: Temperature evolution of lattice parameters (a), axial ratio (b), and unit cell volume (c) for $Ca_3(VO_4)_2$. Data were published in [P2]
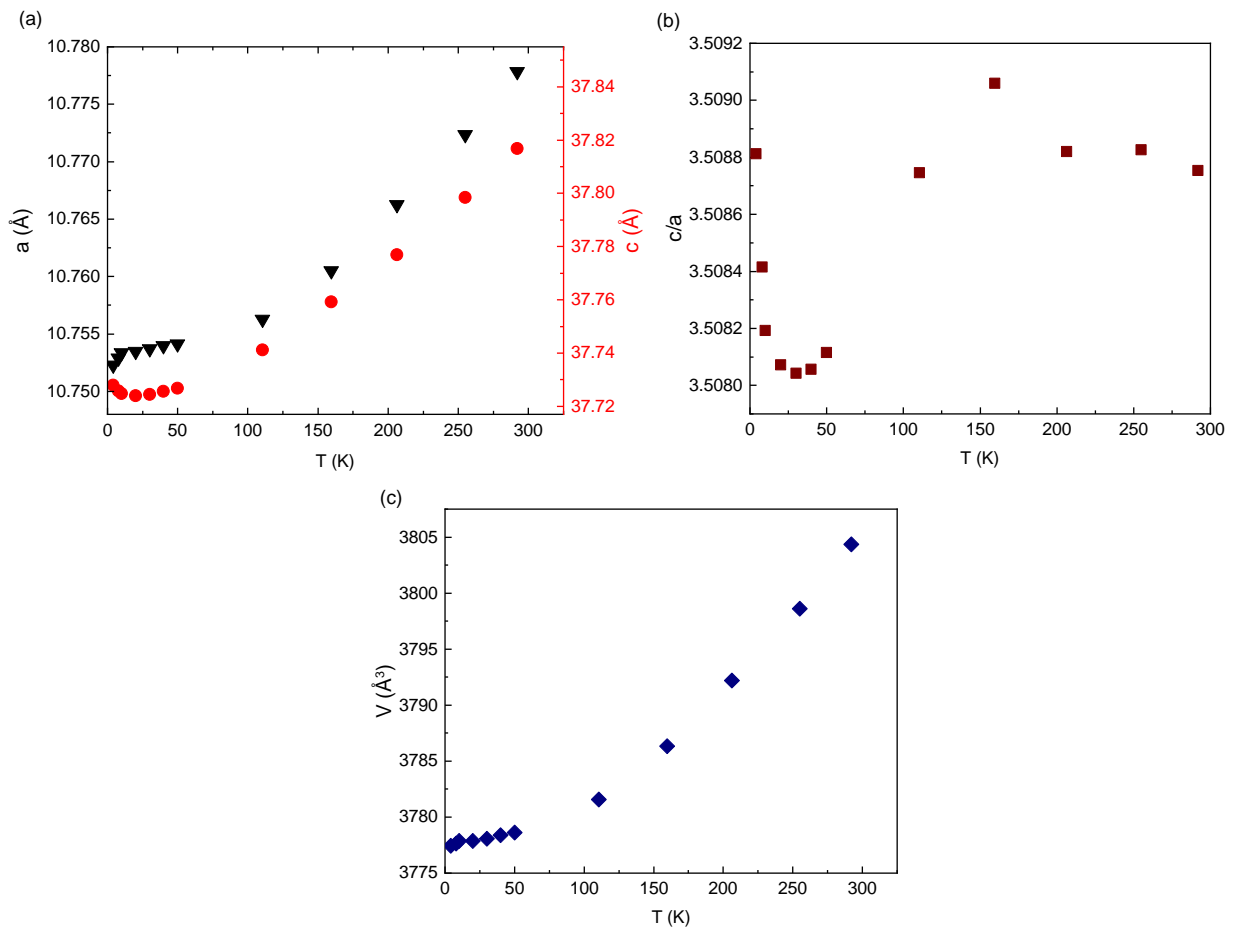
Figure 6.4: Temperature evolution of lattice parameters (a), axial ratio (b), and unit cell volume (c) for Ca$_{10}$Ni$_{0.5}$(VO$_4$)$_7$.
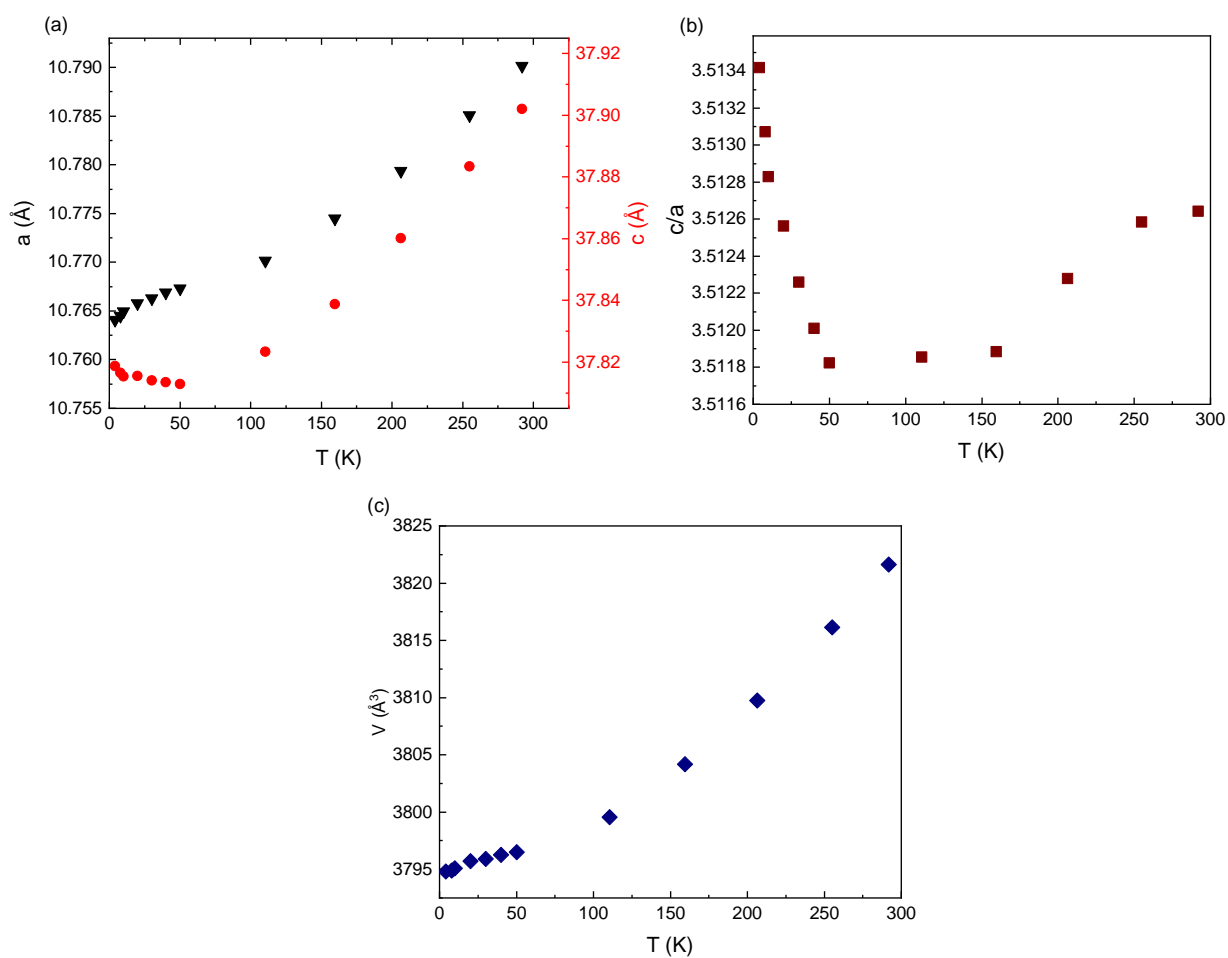
Figure 6.5: Temperature evolution of lattice parameters (a), axial ratio (b), and unit cell volume (c) for $Ca_{10}Cu_{0.5}(VO_4)_7$.

for the observed behavior of the bond lengths. At low temperatures, the vibrational motion of atoms is reduced, and changes in bond lengths may be associated with the rotation of polyhedra.
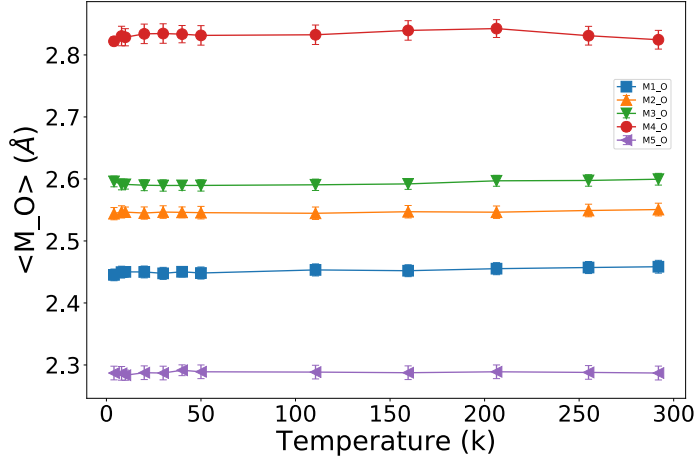
Figure 6.6: Temperature evolution of average interatomic distances for $Ca_3(VO_4)_2$.
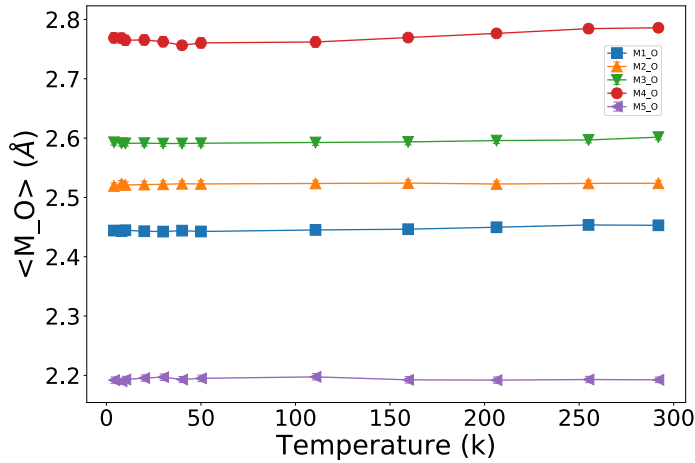
Figure 6.7: Temperature evolution of average interatomic distances for $Ca_{10}Ni_{0.5}(VO_4)_7$.

6.2   Thermal expansion

In order to determine the volumetric thermal expansion value at low temperatures, the second order of Grüneisen approximation were utilized to fit the unit cell volume. The solid dashed line depicted in Fig. 6.9 represents the results obtained from this model.

Thermal expansion coeeficient $\alpha_V(T)$ acquire from

$$\alpha_V = \frac{1}{V(T)}\frac{dV(T)}{dT} \tag{6.1}$$
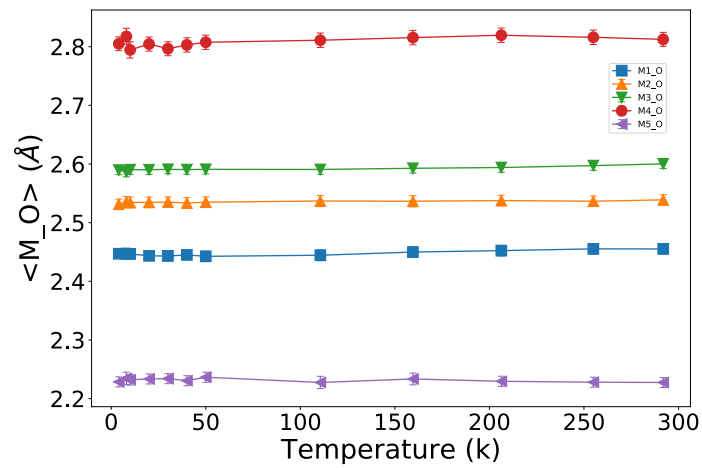
Figure 6.8: Temperature evolution of average interatomic distances for $Ca_{10}Cu_{0.5}(VO_4)_7$.
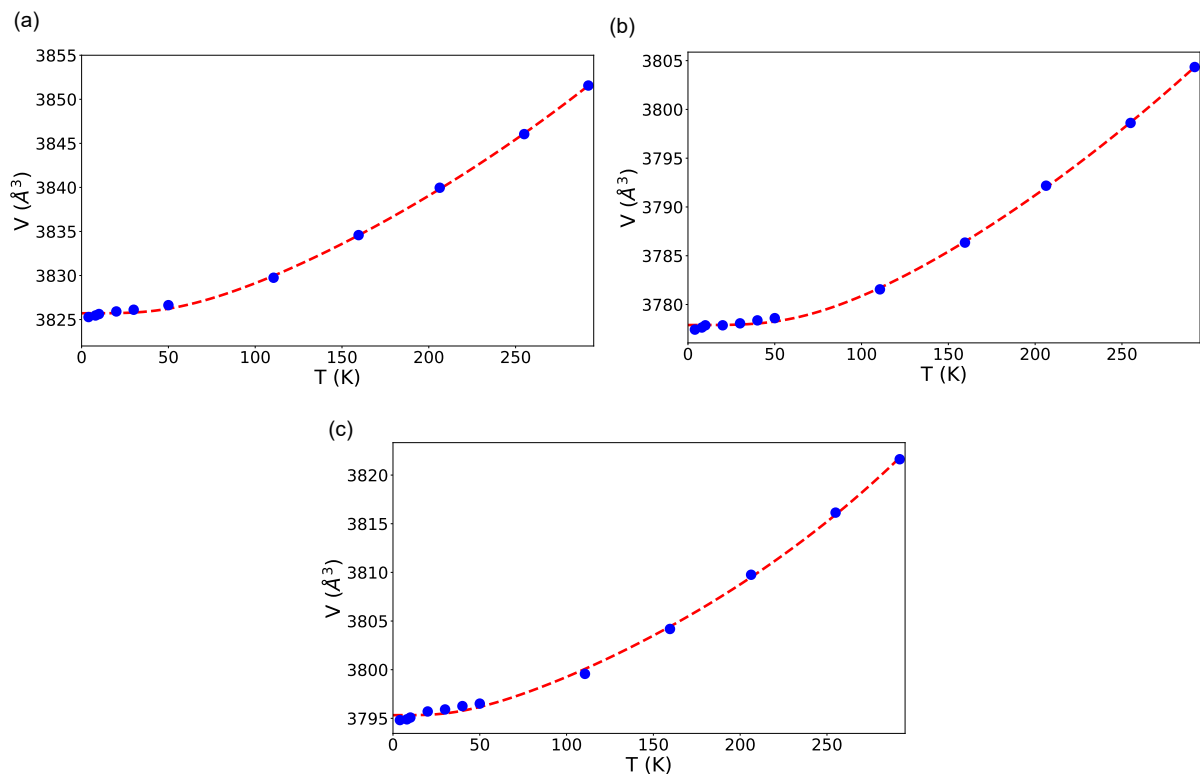
Figure 6.9: Temperature evolution of volume for $Ca_3(VO_4)_2$ (a), $Ca_{10}Ni_{0.5}(VO_4)_7$ (b), $Ca_{10}Cu_{0.5}(VO_4)_7$ (c). The results of modeling by a second order Grüneisen approximation, are shown with a dashed line. Figure (a) reproduces form [P2]

the Grüneisen approximation agrees quite well with the experimental data using lagrangian interpolation (Fig. 6.10).
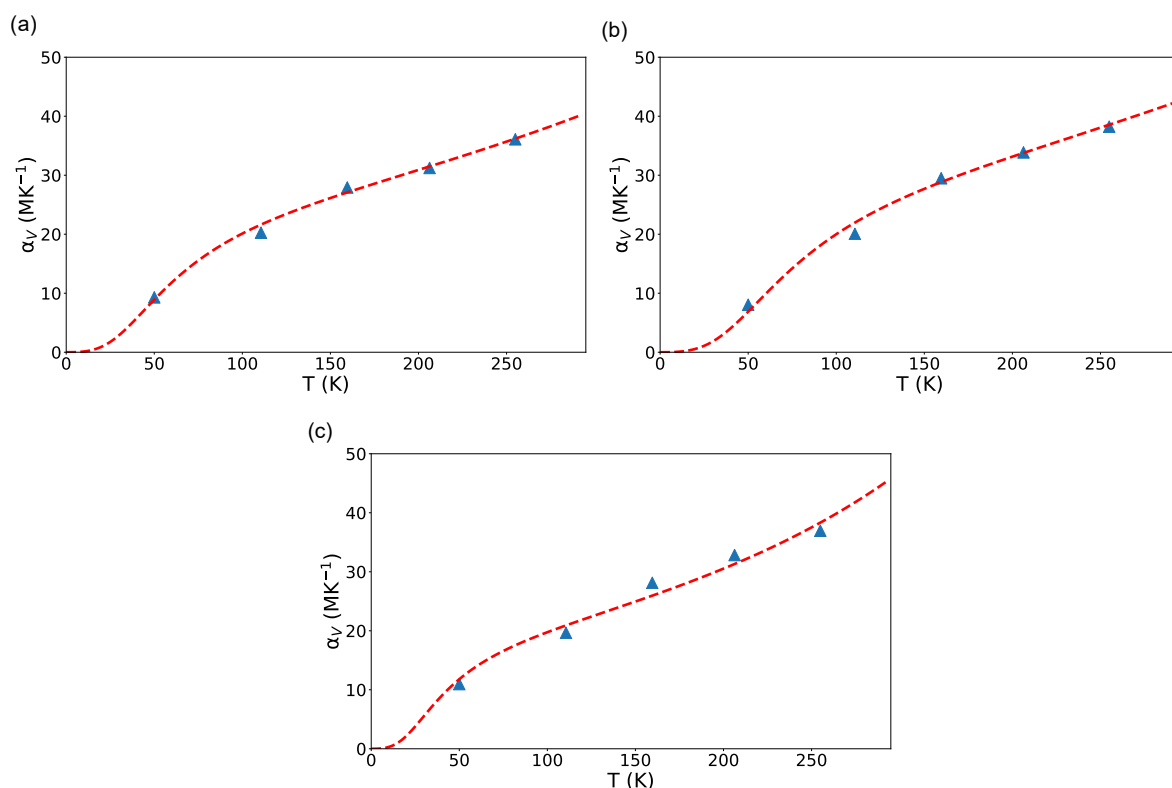
Figure 6.10: Temperature evaluation of volumetric thermal expansion coefficients (TEC) for Ca$_3$(VO$_4$)$_2$ (a), Ca$_{10}$Ni$_{0.5}$(VO$_4$)$_7$ (b), Ca$_{10}$Cu$_{0.5}$(VO$_4$)$_7$ (c) using both Lagrangian interpolation (symbols) and second order Grüneisen approximation (dashed line). Figure (a) reproduces form [P2].

The Debye temperature (θ_D) were evaluated for the three compounds and obtained values of θ_D = 264(2) K for Ca$_{10}$(VO$_4$)$_7$ [P2], 331(1) K for Ca$_{10}$Ni$_{0.5}$(VO$_4$)$_7$ and 177(1) K for Ca$_{10}$Cu$_{0.5}$(VO$_4$)$_7$. It should be noted that these values are only approximate and may not be entirely precise. It is important to conduct further studies to obtain more accurate values of the Debye temperature for these materials. Nonetheless, these estimated values provide insight into the order of magnitude of the Debye temperature for each compound, which can be useful for understanding the vibrational properties and thermal behavior of the materials.

There have been limited reports on the use of DFT calculations to determine the Debye temperature of other materials related to Ca$_3$(VO$_4$)$_2$ but possessing different space groups. For instance, the Debye temperature calculated for Sr$_3$P$_2$O$_8$ (space group *R-3m*) is 559 K [99]. Replacing Ca with a heavier atom, such as Sr, increases the structure rigidity and this could account for the observed differences in Debye temperatures. Similarly, a

variation in Debye temperatures is noted when comparing $Ca_3(PO_4)_2$:$0.07Ce^{3+}$ ($\theta_D = 541$ K) with $Ca_{1.5}Sr_{1.5}(PO_4)_2$:$0.07Ce^{3+}$ ($\theta_D = 730$ K) [100].

Chapter 7

General discussion

Among various multicomponent oxides, those that crystallize in the whitlockite-β-$Ca_3(PO_4)_2$ structure type offer a wide range of compositions, allowing for tuning of their properties. The richness of the properties of interest can be attributed to the presence of specific sites with distinct substitution.

This thesis presents an investigation into the structure of three closely related compounds, in which divalent transition metals (Co, Ni, Cu) are substituted into $Ca_3(VO_4)_2$ compounds. The substituents were chosen to be of similar ionic size in order to facilitate a comparative analysis of the observed effects of substitution on the structure and on thermal expansion. These compounds, denoted as $Ca_{10.5-x}TM_x(VO_4)_7$, exhibit a trigonal crystal lattice within the $R3c$ space group.

With substituting the TMs, there is a clear decrease in both lattice parameters a and c, as well as the unit cell volume, which is consistent with previous studies on the effect of Co [55], Ni [90], Zn [85, 86], and Cu [8, 84] ions on the crystal structure of TCP. The observed decrease in the c lattice parameter is more pronounced when substituting into TCV than when substituting into TCP. For instance, for copper ion which is substituted to TCP [84] and TCV , reduction c is 0.25% for $Ca_{9.84}Cu_{0.66}(PO_4)_7$ and 0.44% for $Ca_{9.84}Cu_{0.66}(VO_4)_7$ in comparison to pure sample of each family. On the other hand, decrease in a lattice parameter is 0.51% for $Ca_{9.84}Cu_{0.66}(PO_4)_7$ and 0.30% for $Ca_{9.84}Cu_{0.66}(VO_4)_7$.

One interesting feature of these compounds is their smaller solubility limit compared to the TCP family. The solubility limits for studied compounds were determined as $x = 0.78(3)$ for $Ca_{10.5-x}Co_x(VO_4)_7$, $x = 0.72(2)$ for $Ca10.5 - xNi_x(VO_4)_7$, and $x = 0.75(4)$ for $Ca_{10.5-x}Cu_x(VO_4)_7$. These limits are very similar to that earlier studied doubly substituted compounds, $Ca_{9-x}Ba_xBi(VO_4)_7$ [77] and $Ca_{9-x}Mg_xBi(VO_4)_7$ [87]. The present finding indicate that in TCV family the solubility limit is about 0.7 for divalent substitution.

For monovalent and rare earth this value is equal one or higher [21, 52, 95]. In contrast, the solubility limit for the TCP family is equal to or higher than one for all monovalent and divalent elements, as well as rare earth substitution. [6–8].

For small divalent ions (compared to calcium), the M5 site is a suitable location for the sharing of substituted atoms, such as Mn [45, 92], Co [89], Ni [90], Cu [8, 90, 101], Zn [85], with calcium in TCP compounds. The present study's model for occupancy aligns with previous works on divalent ion substitution mentioned above and indicates that the M5 site hosts cobalt, nickel, and copper in $Ca_{10.5-x}TM_x(VO_4)_7$ compounds.
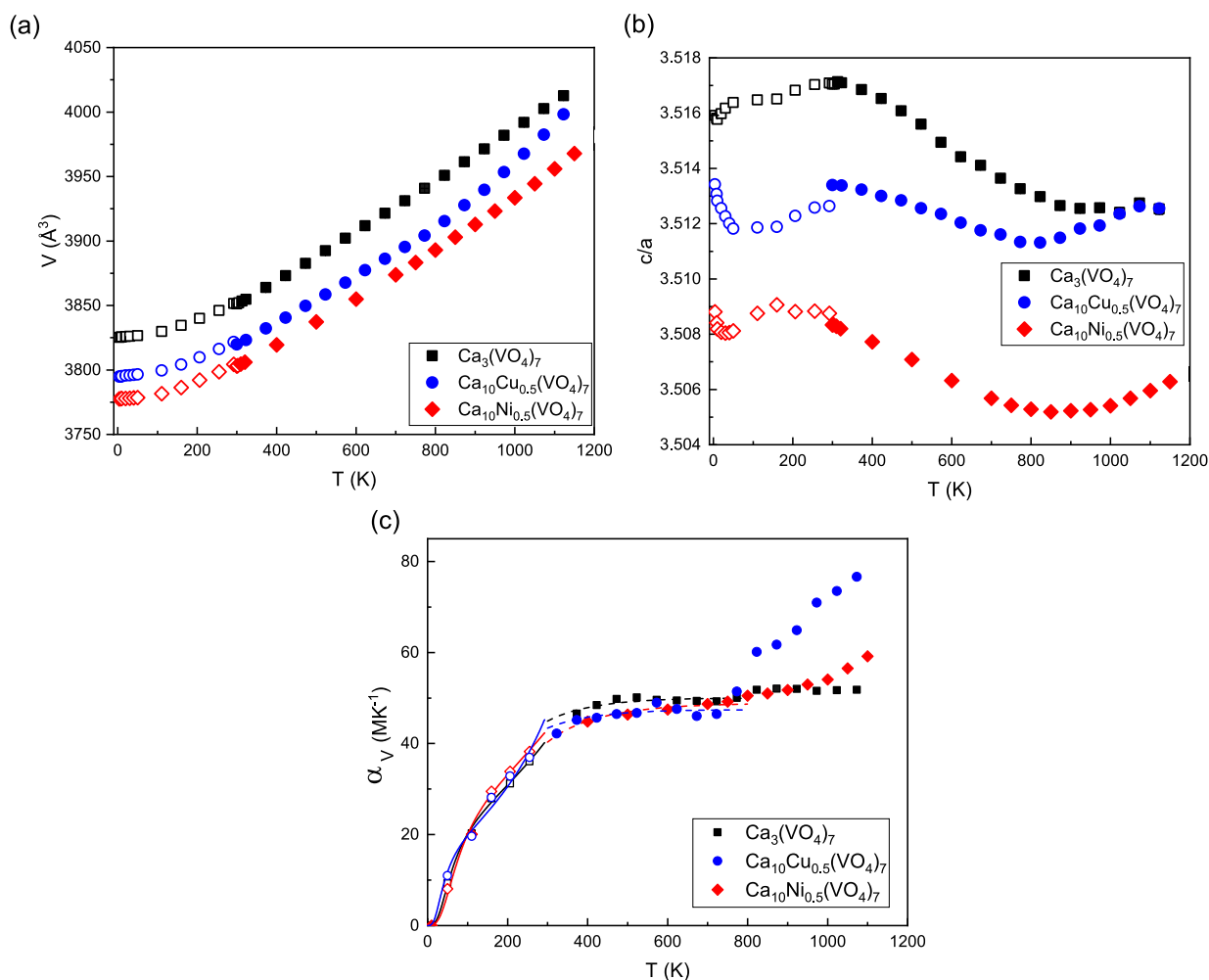
Figure 7.1: Temperature evolution of volume, axial ratio and TEC for $Ca_3(VO_4)_2$, $Ca_{10}Ni_{0.5}(VO_4)_7$ and $Ca_{10}Cu_{0.5}(VO_4)_7$. Empty symbols are data from synchrotron measurement and solid symbols are data from laboratory measurement.

The structures of $Ca_{10.5-x}TM_x(VO_4)_7$ remain stable over the entire temperature range (4-1150 K), with no signs of phase transition and decomposition. For pure material, volume expands smoothly by increasing the temperature, while by adding the transition

metal, change of slope are observed at high temperatures around 800-900 K (Fig. 7.1-a).

In whole temperature range, very weak anisotropy fluctuation in lattice parameter exist which are visible by axial ratio (Fig. 7.1-b).

There are several changes in slope of axial ratio which are dependent on composition and transition metal type. For example, at high temperature the inflection temperature decreases by increasing the content of transition metal. No such effects have been reported for whitlockite type materials till now.

The inflection temperature (T_{inf}), that we obtained from $c/a(T)$, are in line with T_{inf} that obtained from thermal expansion anisotropy defined as α_a/α_c when it equal to one. This implies that the direction of thermal expansion anisotropy changes above the inflection temperature. From room temperature till inflection temperature, α_a is bigger than α_c and above T_{inf}, α_c becomes larger. The only study of thermal expansion using high temperature X-ray measurement related to $Ca_9Gd(VO_4)_7$ [47]. For this material, thermal expansion anisotropy is bigger than in comparison to our studied material for whole temperature range (Fig. 7.2). In relation to the change in anisotropy direction, a notable reduction in TM occupancy at the M5 site was observed above inflection temperature.
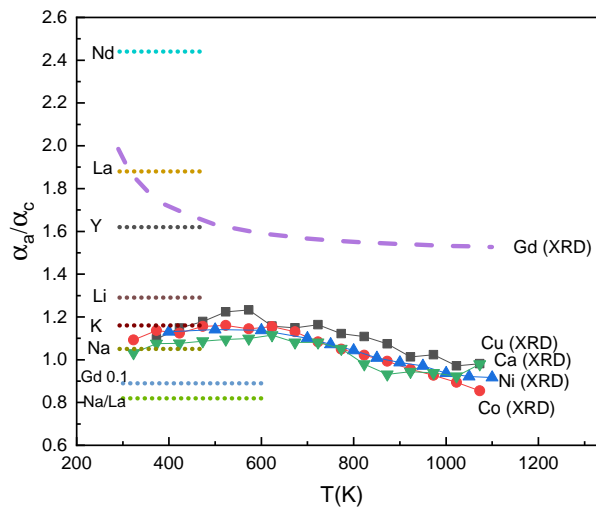
Figure 7.2: Temperature evolution of thermal expansion anisotropy for $Ca_{10}TM_{0.5}(VO_4)_7$ TM = Ca , Co , Ni , Cu using XRD measuremnt. Data for $Ca_9Gd(VO_4)_7$ is taken from [47] (dashed line). dotted lines represent average value of aniostripy using dilatometry for rare erath substituent ($Ca_9Nd(VO_4)_7$ [47] (Nd), $Ca_9La(VO_4)_7$ [18] (La), $Ca_9Y(VO_4)_7$ [18] (Y), $Ca_{2.85}Gd_{0.1}(VO_4)_2$:$Nd^{3+}$ [102] (Gd 0.1)) and monovalent substituent ($Ca_{10}Li(VO_4)_7$:Nd [47] (Li), $Ca_{10}K(VO_4)_7$ [47] (K), $Ca_{10}Na(VO_4)_7$:Nd [47] (Na)) and $Ca_{9.03}Na_{1.08}La_{0.62}(VO_4)_7$:Nd [103] (Na/La).

Additionally, when comparing the average values, which are calculated using dilatometry data [18, 47, 102, 103], the thermal expansion anisotropy is found to be greater than one ($\alpha_a/\alpha_c = 1$ indicating isotropic thermal expansion), except for the samples with low Gd content [102] and those double-substituted with Na and La [103]. Thermal expansion aniosotropy larger than for rare earth substitution in comparison to transition metals. For TMs, the thermal expansion anisotropy value are comparable to the monovalent ions substitutions . By doubly substitution into TCV, we can tune thermal expansion anisotropy which can be useful for future application of this materials.

The volumetric thermal expansion coefficient increase from $9\,\text{MK}^{-1}$ to $46\,\text{MK}^{-1}$ from $50\,\text{K}$ to $\sim400\,\text{K}$ for all investigated materials. In the range from $400\,\text{K}$ till inflection temperature, thermal expansion of $Ca_{10.5-x}TM_x(VO_4)_7$ remain near $46\,\text{MK}$ and for pure material is slightly bigger by $\sim5\,\text{MK}$ (see Fig. 7.1-c). Above inflection temperature, the thermal expansion values increase further, which reach the value of about $60\,\text{MK}^{-1}$ for TM = Co, Ni at $1100\,\text{K}$ and with a more pronounced effect observed for TM = Cu (around $85\,\text{MK}^{-1}$ at 1073 K). TEC slightly decreases by increasing the content of transition metal at room temperature and increase at high temperature (the variations are of the order of uncertainty). For $Ca_9Gd(VO_4)_7$, at room temperature the volumetric thermal expansion is 39 MK^{-1} and increases to $45\,\text{MK}^{-1}$ in the range from 600-1100 K [47]. One can notice that in temperature range till inflection temperature, the value of volumetric thermal expansion for $Ca_{10.5-x}TM_x(VO_4)_7$ are relatively similar to $Ca_9Gd(VO_4)_7$. The effect of substitution ions are appears in change in the nature of aniostropy and step like increase in thermal expansion at temperature above $\sim800\,\text{K}$.

Chapter 8

Conclusions

The dissertation presents a comprehensive investigation into the structure properties of a novel series of compounds, denoted as $Ca_{10.5-x}TM_x(VO_4)_7$, where TM represents the transition metals Co, Ni, and Cu. These compounds were synthesized through a solid-state reaction method.

The structures of the investigated $Ca_{10.5-x}TM_x(VO_4)_7$ compounds were refined by the Rietveld method, based on the powder X-ray diffraction (PXRD) data. The refinement result confirmed that $Ca_{10.5-x}TM_x(VO_4)_7$ crystallizes in a trigonal crystal system within the $R3c$ space group, adopting the whitlockite-β-$Ca_3(PO_4)_2$ structure type.

At room temperature, the unit cell size for $Ca_{10.5-x}TM_x(VO_4)_7$ series decreases as the content of transition metals increases. This is attributed to the smaller ionic radius of Co, Ni, and Cu compared to the Ca ion. One notable characteristic of these compounds is their smaller solubility limit compared to the β-$Ca_3(PO_4)_2$ family. The solubility limits for the studied compounds are determined as $x = 0.78(3)$ for $Ca_{10.5-x}Co_x(VO_4)_7$, $x = 0.72(2)$ for $Ca_{10.5-x}Ni_x(VO_4)_7$, and $x = 0.75(4)$ for $Ca_{10.5-x}Cu_x(VO_4)_7$. These limits closely resemble those observed in previous studies on doubly substituted compounds. The findings suggest that the solubility limit for divalent substitution in TCV based compounds is around 0.7, while it equals or exceeds unity for divalent substitutions in TCP based compounds.

The results of the occupancy refinements revealed the presence of the transition metal cation at the M5 site. Furthermore, the preference of specific sites by the transition metal is influenced by the size effect. Specifically, the site with the smallest M-O distances (i.e., M5-based) are more favorable for occupation by the transition metal.

The structure of $Ca_{10.5-x}TM_x(VO_4)_7$ remains stable from room temperature till 1150 K and there is no sign of phase transition. Lattice parameters expand with temperature but the fluctuations in axial ratio with temperature indicate that the lattice undergoes

anisotropic expansion. The inflection temperature at HT tends to decrease as the content of transition metal increases. Such phenomenon has not been reported in other whitlockite type material investigated till now.

It is found that the occupancy of TMs at M5 site for $Ca_{10}Co_{0.5}(VO_4)_7$ and $Ca_{10}Cu_{0.5}(VO_4)_7$ reduce above inflection temperature. It is possible to observe such behavior for various concentrations and different transition metals. Drop of fractional TM occupancy roughly correlated with change of anisotropy direction.

Volumetric thermal expansion coefficient increases from 9 MK^{-1} to 46 MK^{-1} from 50 K to $\sim$400 K. In the range from 400 K till inflection temperature, thermal expansion of pure material is slightly bigger that substituted ones (around 5 MK^{-1}). Around the inflection temperature, volumetric thermal expansion is the same and at the highest temperature, for TM = Co, Ni, the thermal expansion increases by approximately 50%. For TM = Cu, this change is twice bigger. On the other hand for pure sample, $Ca_3(VO_4)_2$, from inflection till 1073 K, there is no change in volumetric thermal expansion.

Debye temperature based on Grüneisen approximation $V(T)$ was evaluated for $Ca_3(VO_4)_2$, $Ca_{10}Ni_{0.5}(VO_4)_7$ and $Ca_{10}Cu_{0.5}(VO_4)_7$ samples which is around $\sim$250 K.

The results obtained in this dissertation provide a wide knowledge of structural properties of novel $Ca_{10.5-x}TM_x(VO_4)_7$ compounds. In particular, the determination of solubility limit and effect of TMs in thermal expansion which maybe useful for future application.

Appendix A

Structures of Ca$_{10.5-x}$TM$_x$(VO$_4$)$_7$ compounds at room temperature
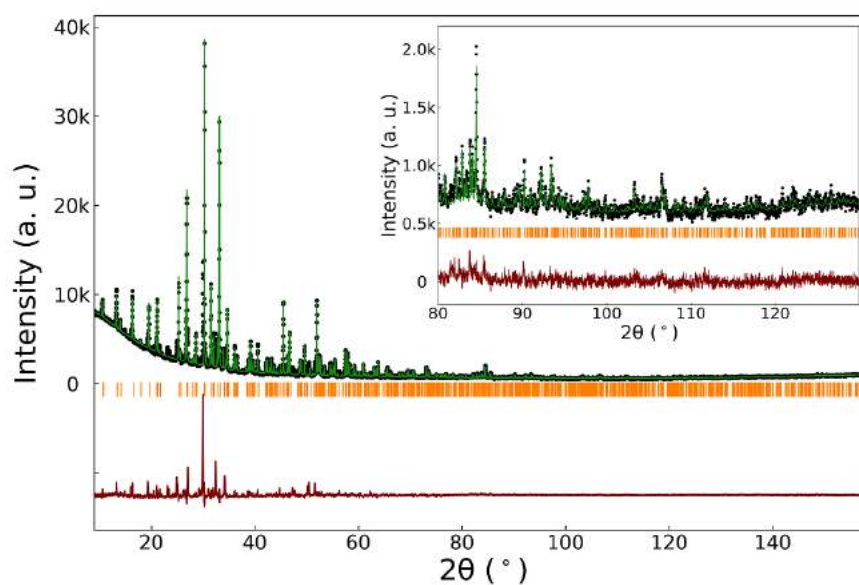
Figure A.1: Illustration of the Rietveld refinement of Ca$_{10.34}$Co$_{0.16}$(VO$_4$)$_7$ sample. The refinement results are quantified by the R factors, with values of R factors are: Rp = 5.54%, Rwp = 10.40% and Rexp = 2.55%
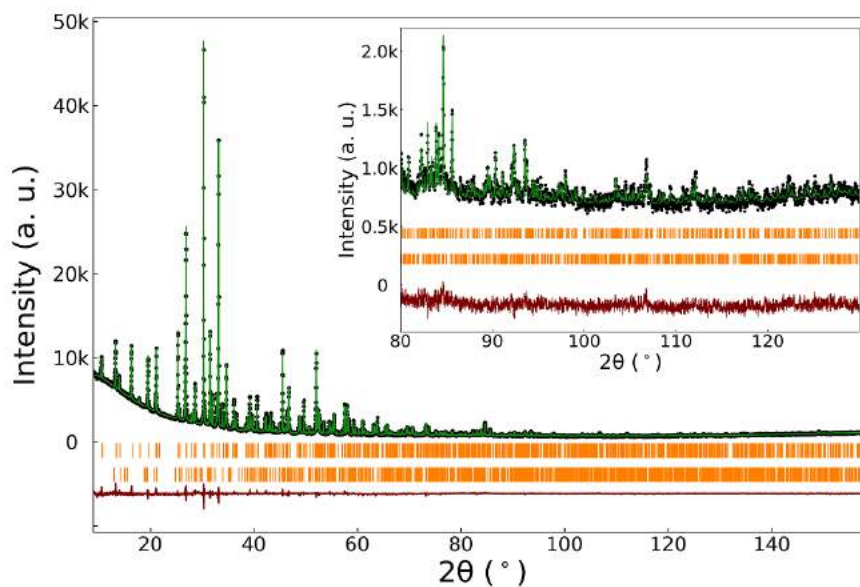
Figure A.2: Illustration of the Rietveld refinement of $Ca_{10.17}Co_{0.33}(VO_4)_7$ sample. The upper orange vertical bars represent peak position of $Ca_{10.17}Co_{0.33}(VO_4)_7$ - main phase and the lower vertical bars represent peak position of $Ca_2V_2O_7$- minor phase. R factors are: Rp = 2.80%, Rwp = 3.72% and Rexp = 2.46%
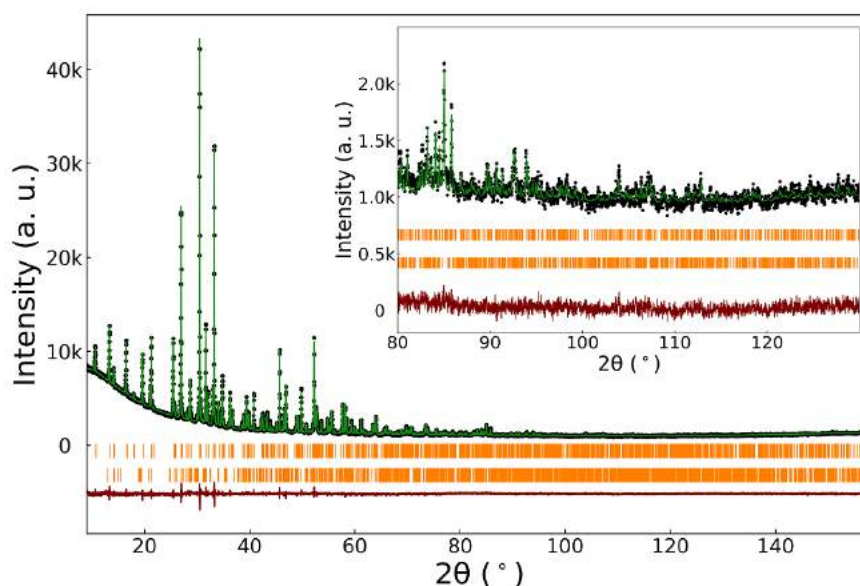
Figure A.3: Illustration of the Rietveld refinement of $Ca_{9.84}Co_{0.66}(VO_4)_7$ sample. The upper orange vertical bars represent peak position of $Ca_{9.84}Co_{0.66}(VO_4)_7$ - main phase and the lower vertical bars represent peak position of $Ca_2V_2O_7$- minor phase. R factors are: Rp = 2.46%, Rwp = 3.27% and Rexp = 2.27%
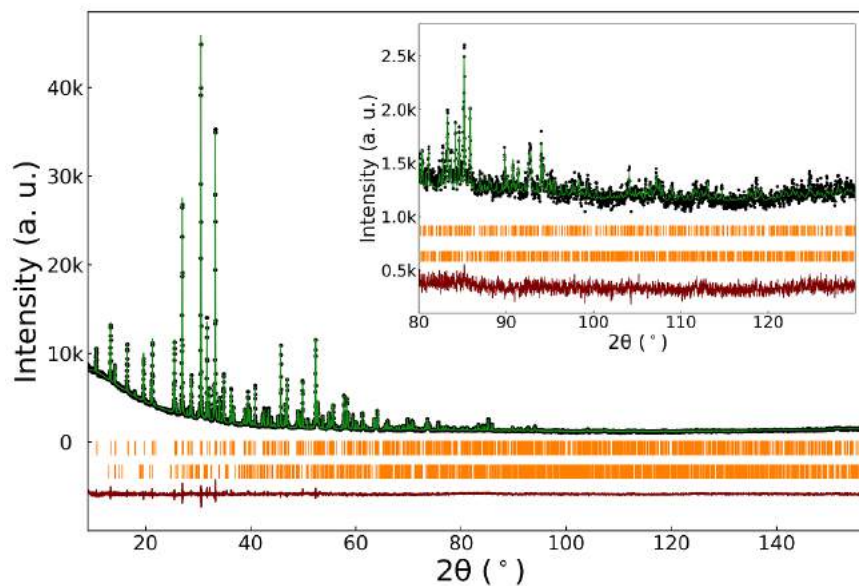
Figure A.4: Illustration of the Rietveld refinement of Ca$_{9.67}$Ni$_{0.83}$(VO$_4$)$_7$ sample. R factors are: Rp = 2.32%, Rwp = 3.05% and Rexp = 2.15%
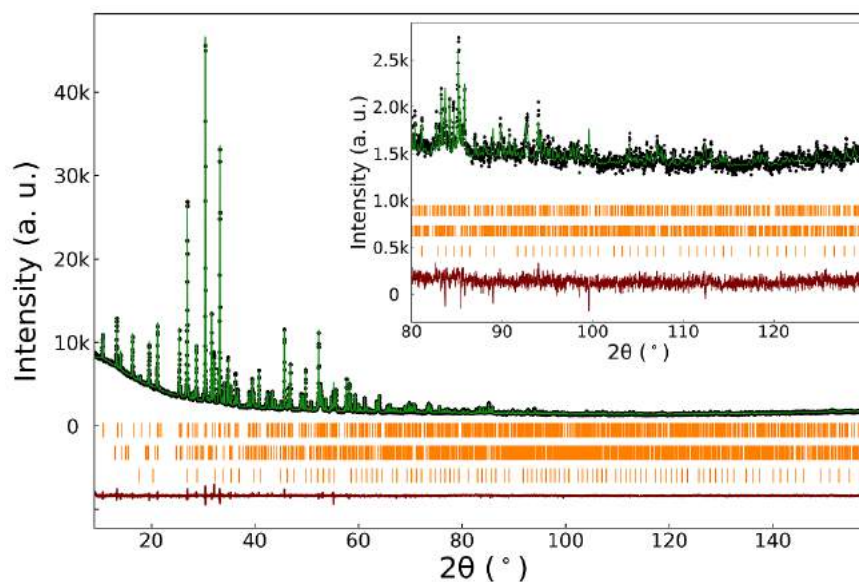
Figure A.5: Illustration of the Rietveld refinement of Ca$_{9.5}$Co(VO$_4$)$_7$ sample.The upper orange vertical bars represent peak position of Ca$_{9.5}$Co(VO$_4$)$_7$ - main phase, the middle vertical bars represent peak position of Ca$_2$V$_2$O$_7$ and the lower vertical green bars represent peak position of Ca$_{2.5}$Co$_2$(VO$_4$)$_3$- minor phases. R factors are: Rp = 2.18%, Rwp = 2.91% and Rexp = 2.04%
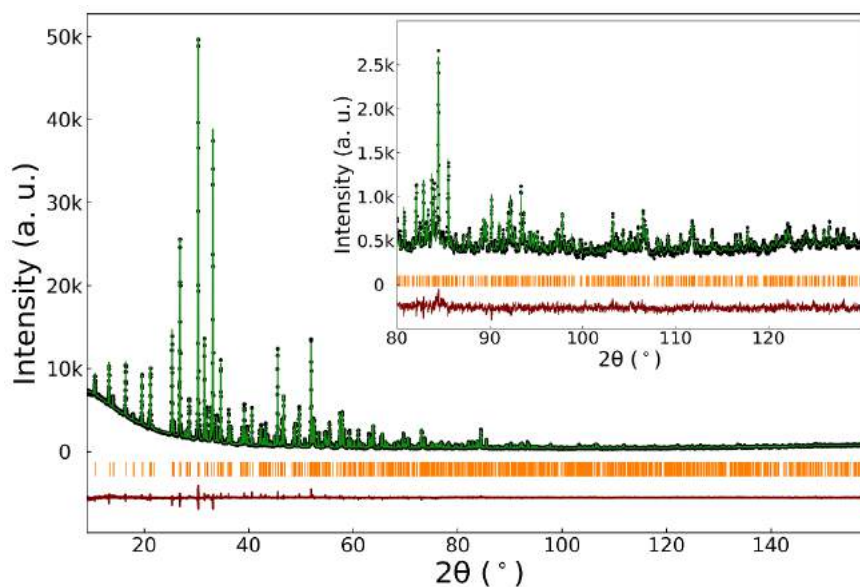
Figure A.6: Illustration of the Rietveld refinement of $Ca_{10.34}Ni_{0.16}(VO_4)_7$ sample. The refinement results are quantified by the R factors, with values of Rp = 3.3%, Rwp = 4.40% and Rexp = 2.82%
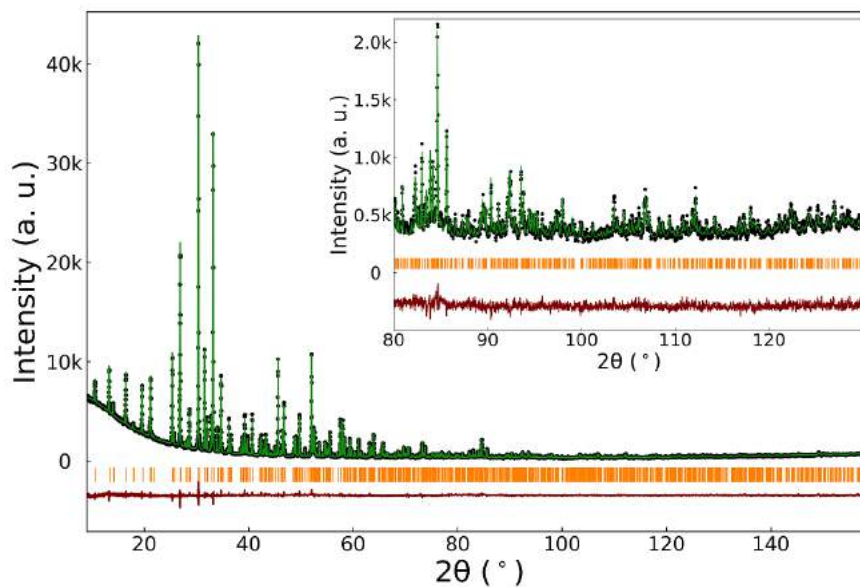
Figure A.7: Illustration of the Rietveld refinement of $Ca_{10.17}Ni_{0.33}(VO_4)_7$ sample. R factors are: Rp = 3.33%, Rwp = 4.56% and Rexp = 3.06%
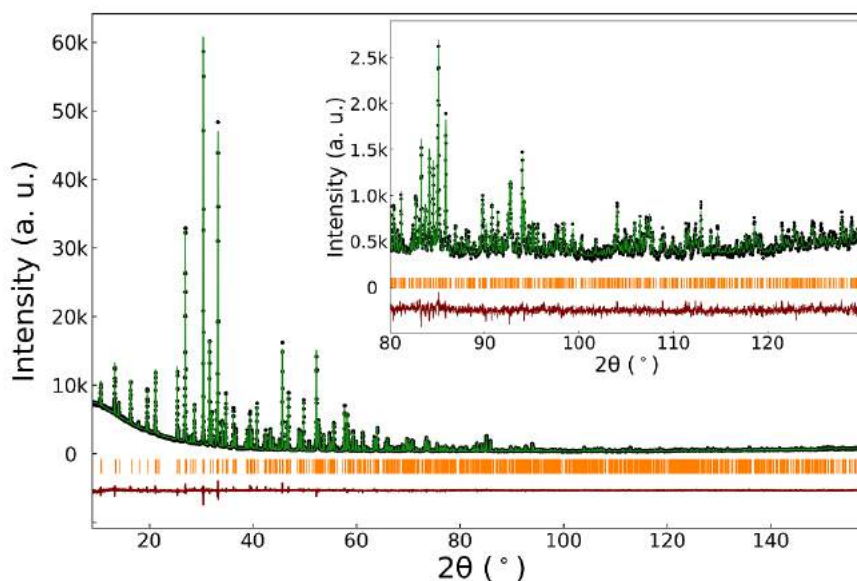
Figure A.8: Illustration of the Rietveld refinement of Ca$_{9.84}$Ni$_{0.66}$(VO$_4$)$_7$ sample. R factors are: Rp = 3.33%, Rwp = 4.51% and Rexp = 2.79%
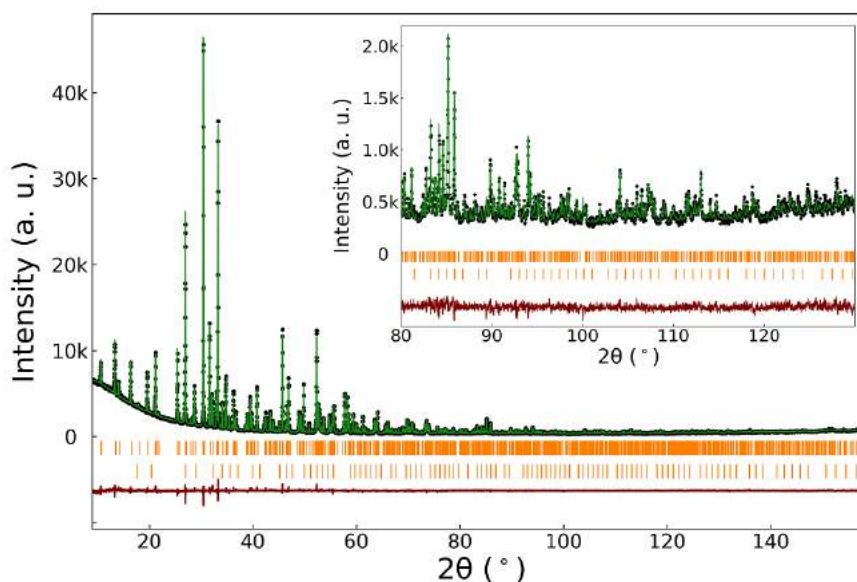
Figure A.9: Illustration of the Rietveld refinement of Ca$_{9.67}$Ni$_{0.83}$(VO$_4$)$_7$ sample. The upper green vertical bars represent Ca$_{9.67}$Ni$_{0.83}$(VO$_4$)$_7$ - main phase and lower vertical bars represent Ca$_{2.5}$Ni$_2$(VO$_4$)$_3$- minor phase. R factors are: Rp = 3.42%, Rwp = 4.66% and Rexp = 2.98%
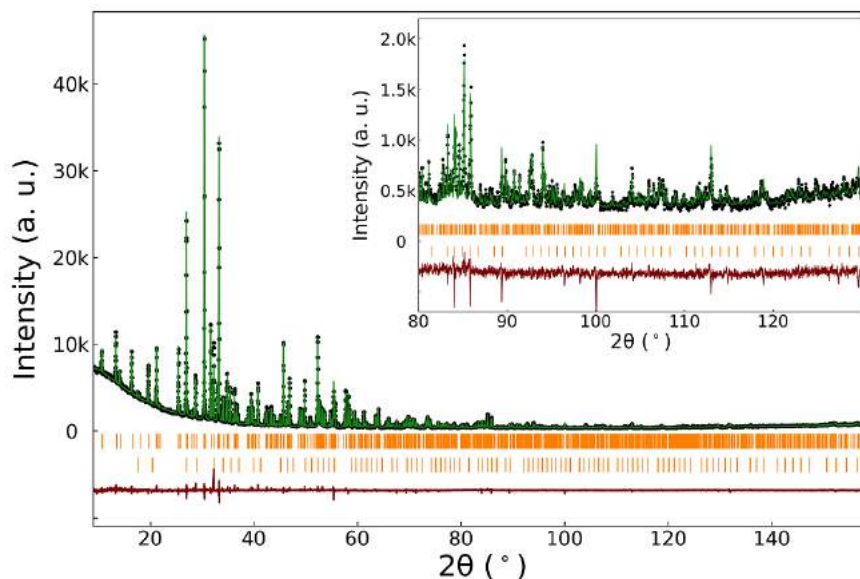
Figure A.10: Illustration of the Rietveld refinement of $Ca_{9.5}Ni(VO_4)_7$ sample. The upper orange vertical bars represent $Ca_{9.5}Ni(VO_4)_7$ - main phase and lower vertical bars represent $Ca_{2.5}Ni_2(VO_4)_3$- minor phase. R factors are: Rp = 3.58%, Rwp = 5.34% and Rexp = 2.86%
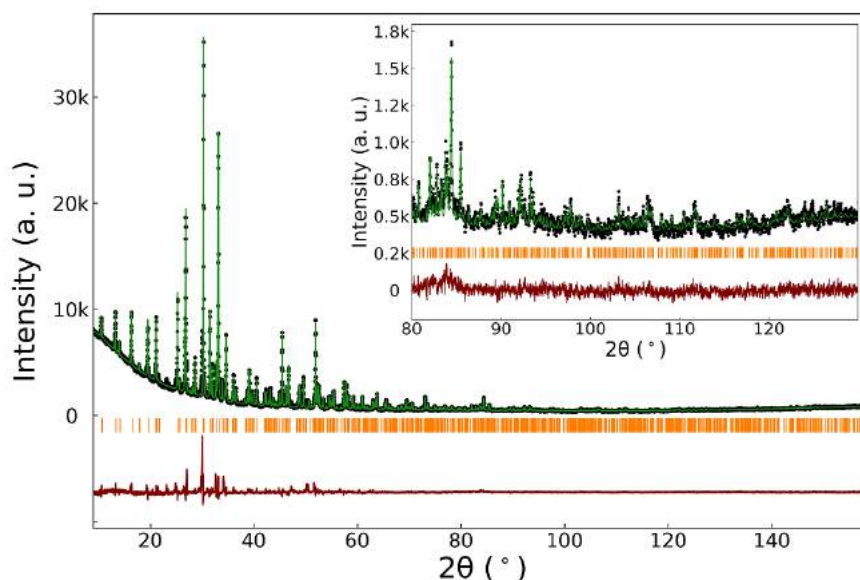
Figure A.11: Illustration of the Rietveld refinement of $Ca_{10.34}Cu_{0.16}(VO_4)_7$ sample. R factors are: Rp = 4.84%, Rwp = 8.30% and Rexp = 2.74%
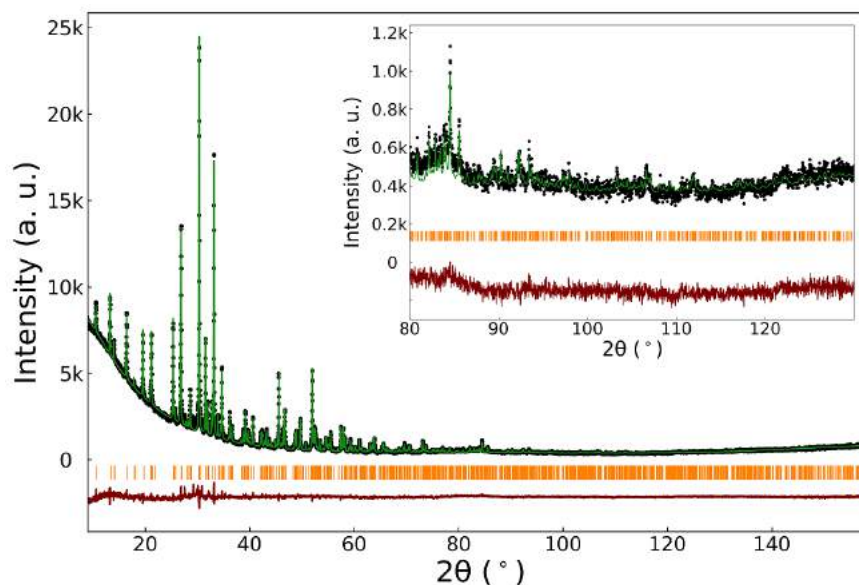
Figure A.12: Illustration of the Rietveld refinement of $Ca_{10.17}Cu_{0.33}(VO_4)_7$ sample. R factors are: Rp = 3.60%, Rwp = 5.28% and Rexp = 2.90%
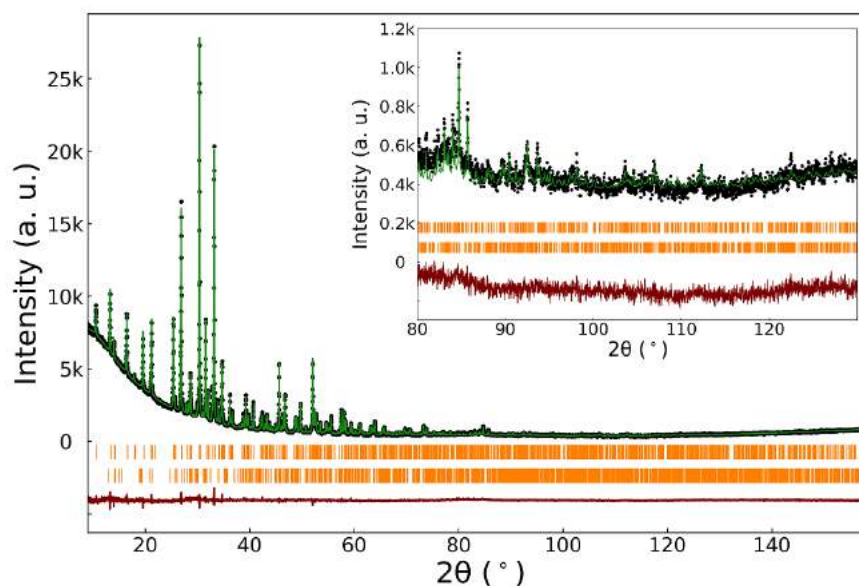
Figure A.13: Illustration of the Rietveld refinement of $Ca_{9.84}Cu_{0.66}(VO_4)_7$ sample. The upper orange vertical bars represent peak position of $Ca_{9.84}Cu_{0.65}(VO_4)_7$ - main phase and the lower vertical bars represent peak position of $Ca_2V_2O_7$- minor phase. R factors are: Rp = 3.25%, Rwp = 4.67% and Rexp = 2.86%
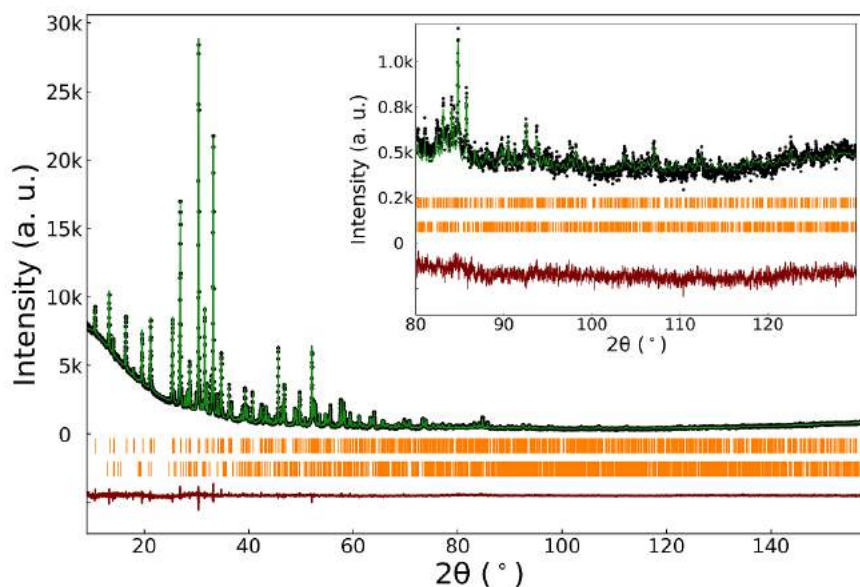
Figure A.14: Illustration of the Rietveld refinement of $Ca_{9.67}Cu_{0.83}(VO_4)_7$ sample. The upper orange vertical bars represent peak position of $Ca_{9.67}Cu_{0.83}(VO_4)_7$ - main phase and the lower vertical bars represent peak position of $Ca_2V_2O_7$- minor phase. R factors are: Rp = 3.01%, Rwp = 4.22% and Rexp = 2.80%
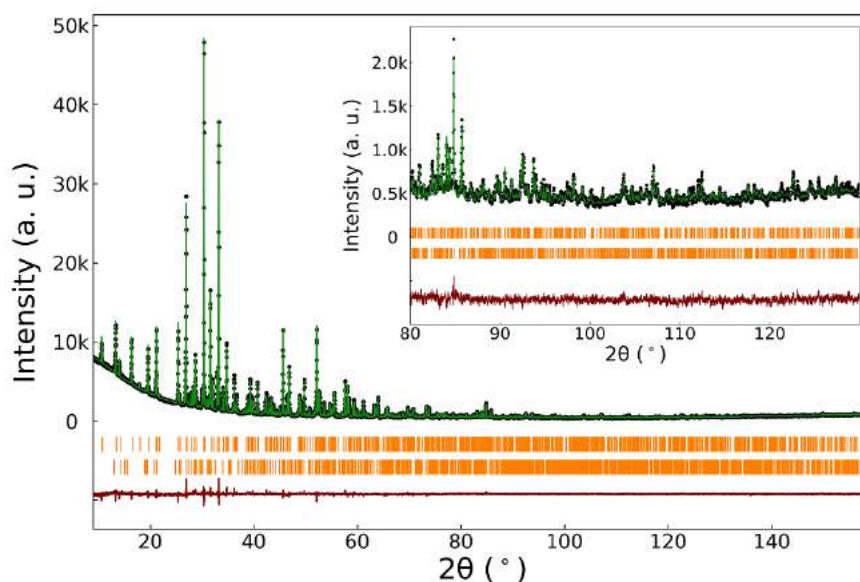
Figure A.15: Illustration of the Rietveld refinement of $Ca_{9.5}Cu(VO_4)_7$ sample. The upper orange vertical bars represent peak position of $Ca_{9.5}Cu(VO_4)_7$ - main phase and the lower vertical bars represent peak position of $Ca_2V_2O_7$- minor phase. R factors are: Rp = 3.47%, Rwp = 4.71% and Rexp = 2.71%
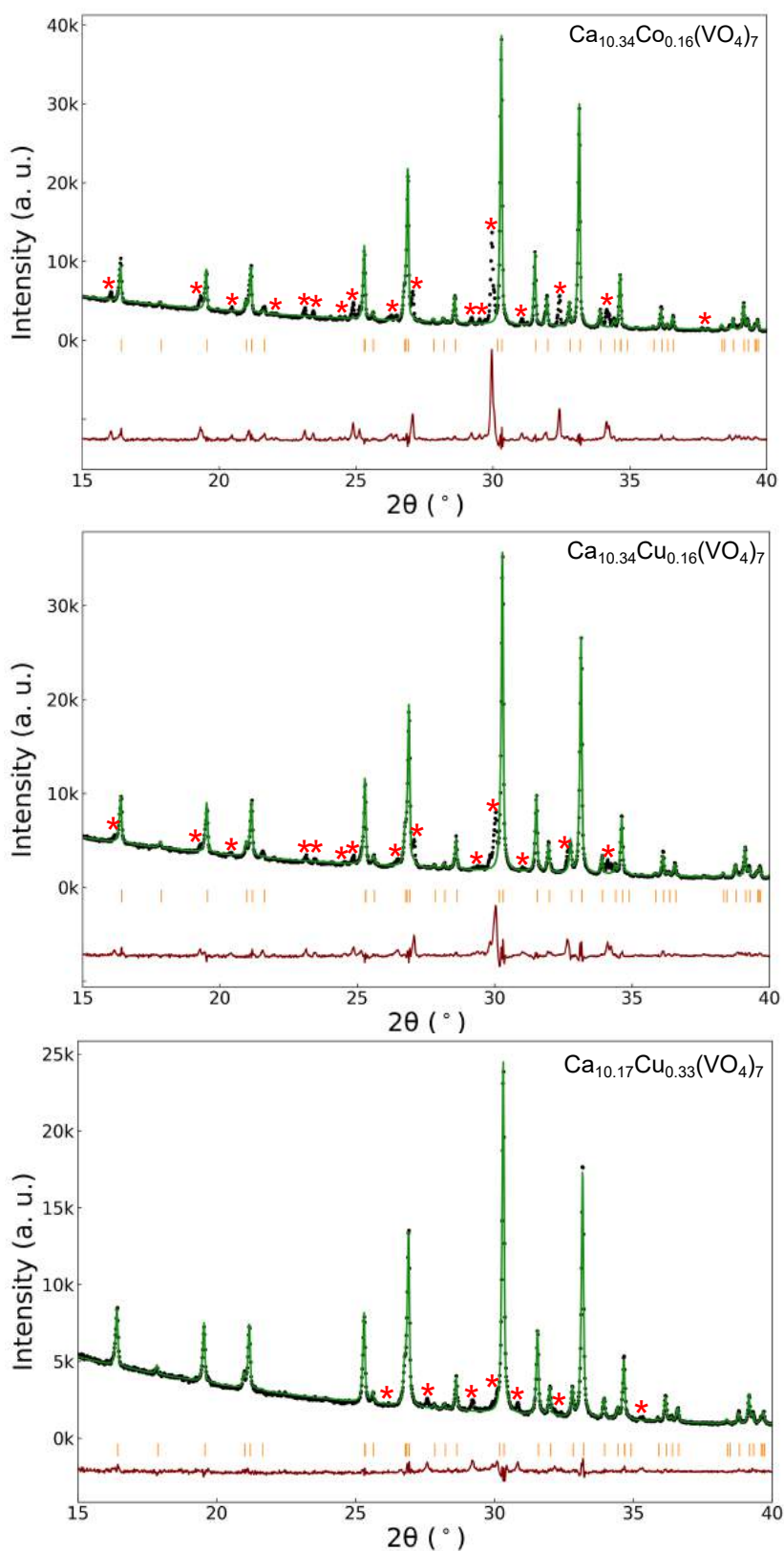
Figure A.16: Illustration of Rietveld refinements of Ca$_{10.34}$Co$_{0.16}$(VO$_4$)$_7$, Ca$_{10.34}$Cu$_{0.16}$(VO$_4$)$_7$ and Ca$_{10.17}$Ni$_{0.33}$(VO$_4$)$_7$ samples containing foreign peaks which marked by star at low angles.
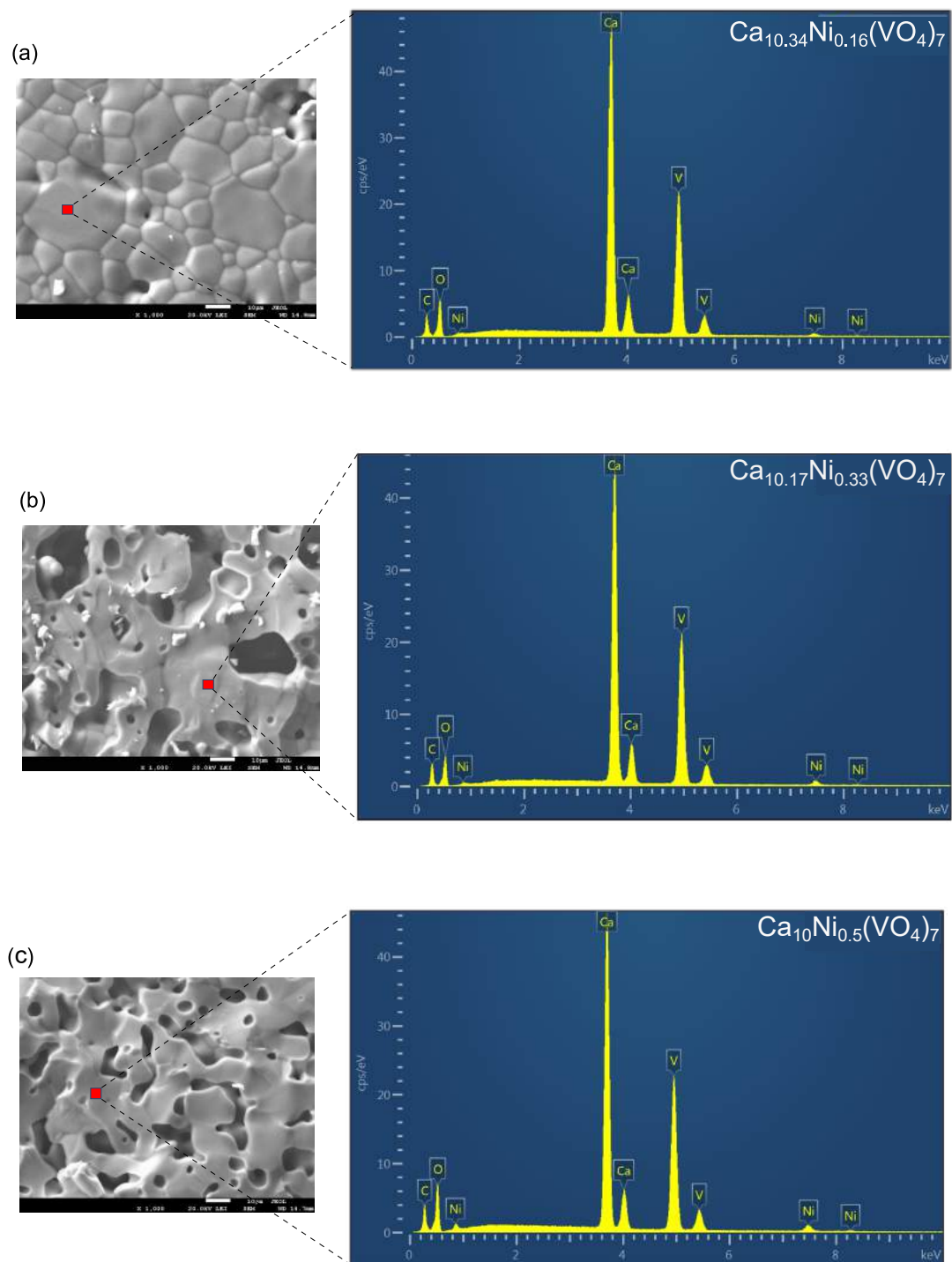
Figure A.17: SEM image and EDX spectrum of the surface of $Ca_{10.34}Co_{0.16}(VO_4)_7$ sample (a), $Ca_{10.17}Co_{0.33}(VO_4)_7$ sample (b) and $Ca_{10}Co_{0.5}(VO_4)_7$ (c).
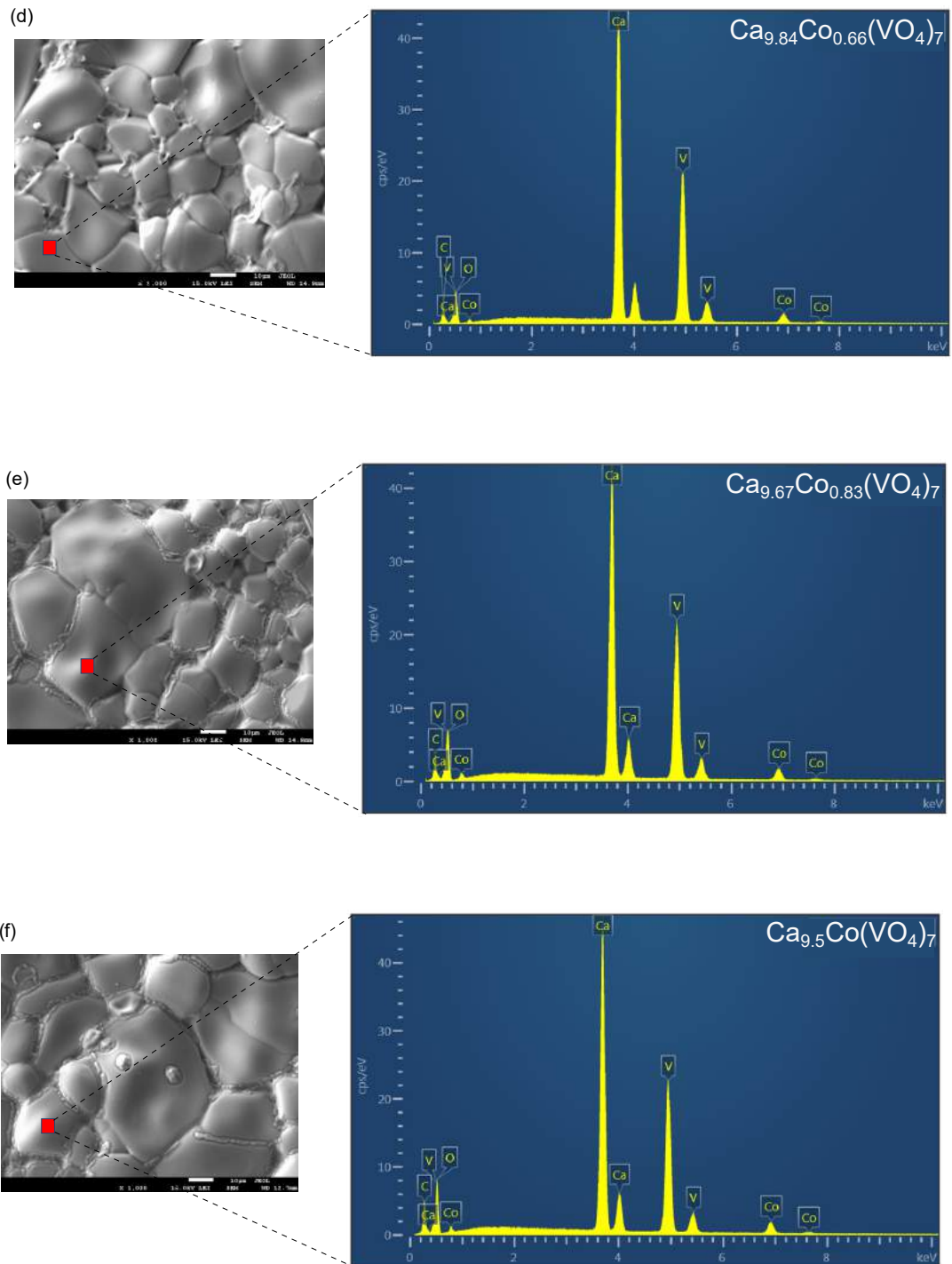
Figure A.18: SEM image and EDX spectrum of the surface of $Ca_{9.84}Co_{0.66}(VO_4)_7$ sample (d), $Ca_{9.67}Co_{0.83}(VO_4)_7$ sample (e) and $Ca_{9.5}Co(VO_4)_7$ (f).
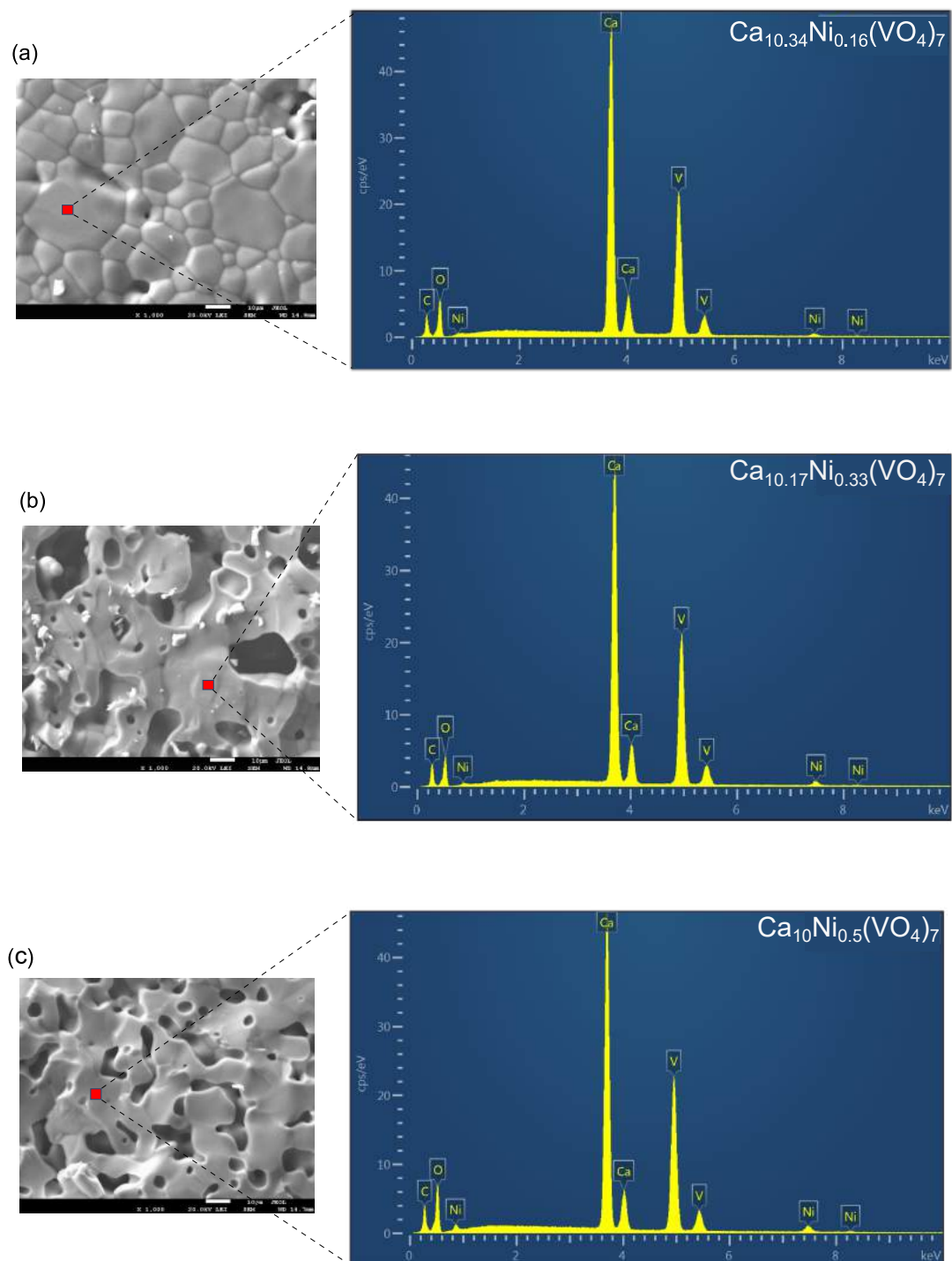
Figure A.19: SEM image and EDX spectrum of the surface of $Ca_{10.34}Ni_{0.16}(VO_4)_7$ sample (a) [P3], $Ca_{10.17}Ni_{0.33}(VO_4)_7$ sample (b) and $Ca_{10}Ni_{0.5}(VO_4)_7$ (c).
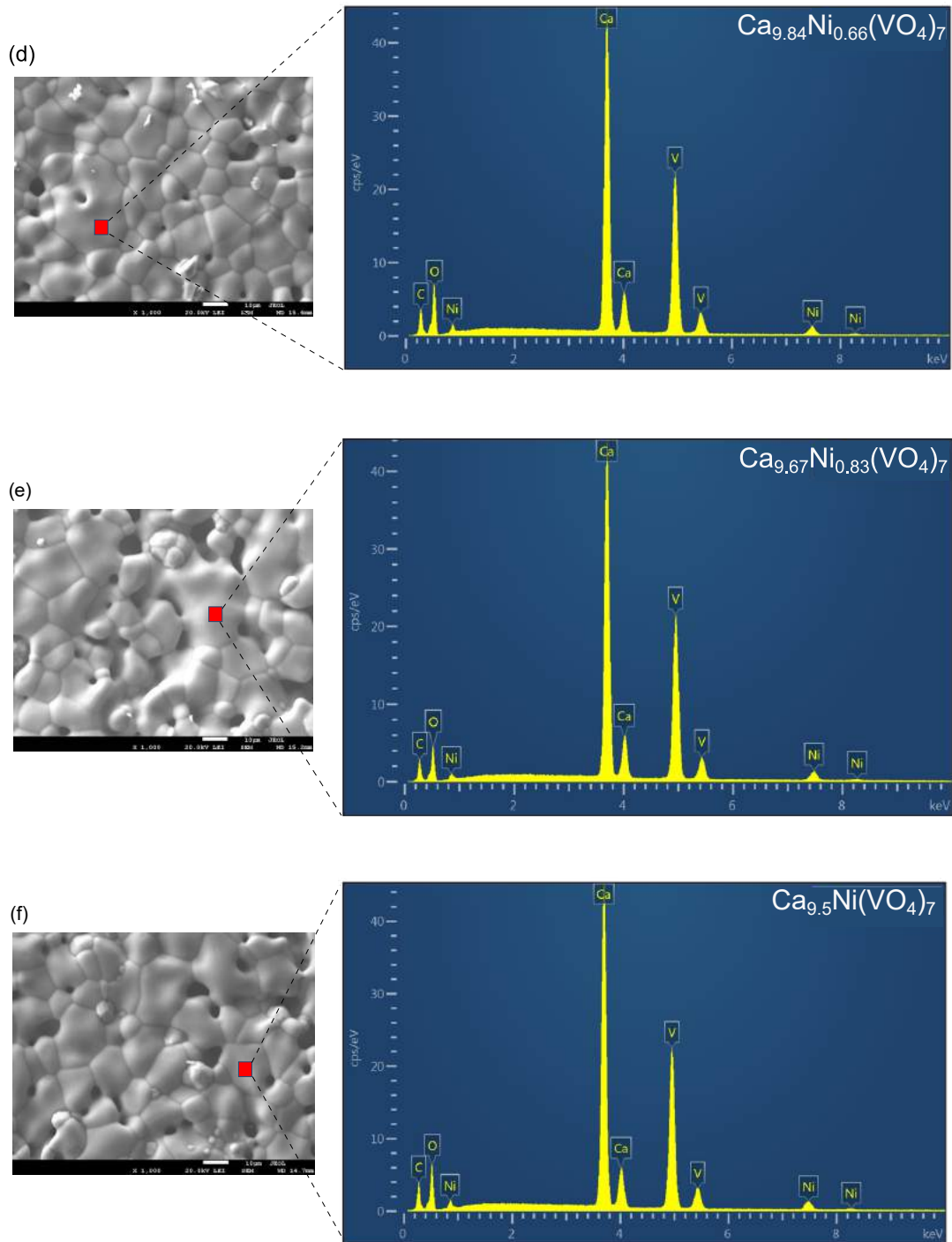
Figure A.20: SEM image and EDX spectrum of the surface of Ca$_{9.84}$Ni$_{0.66}$(VO$_4$)$_7$ sample (d), Ca$_{9.67}$Ni$_{0.83}$(VO$_4$)$_7$ sample (e) [P3] and Ca$_{9.5}$Ni(VO$_4$)$_7$ (f).
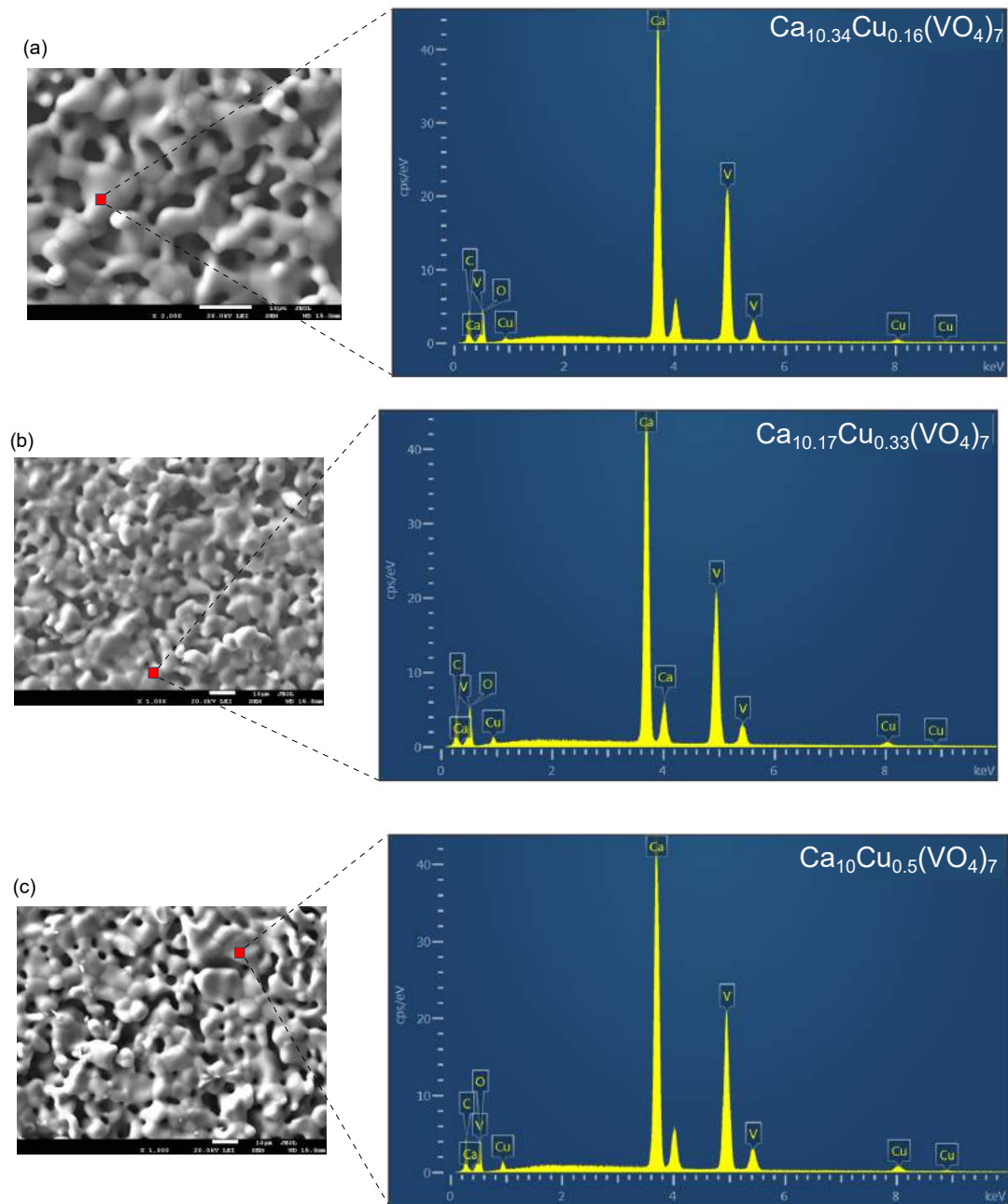
Figure A.21: SEM image and EDX spectrum of the surface of $Ca_{10.34}Cu_{0.16}(VO_4)_7$ sample (a), $Ca_{10.17}Cu_{0.33}(VO_4)_7$ sample (b) and $Ca_{10}Cu_{0.5}(VO_4)_7$ (c).
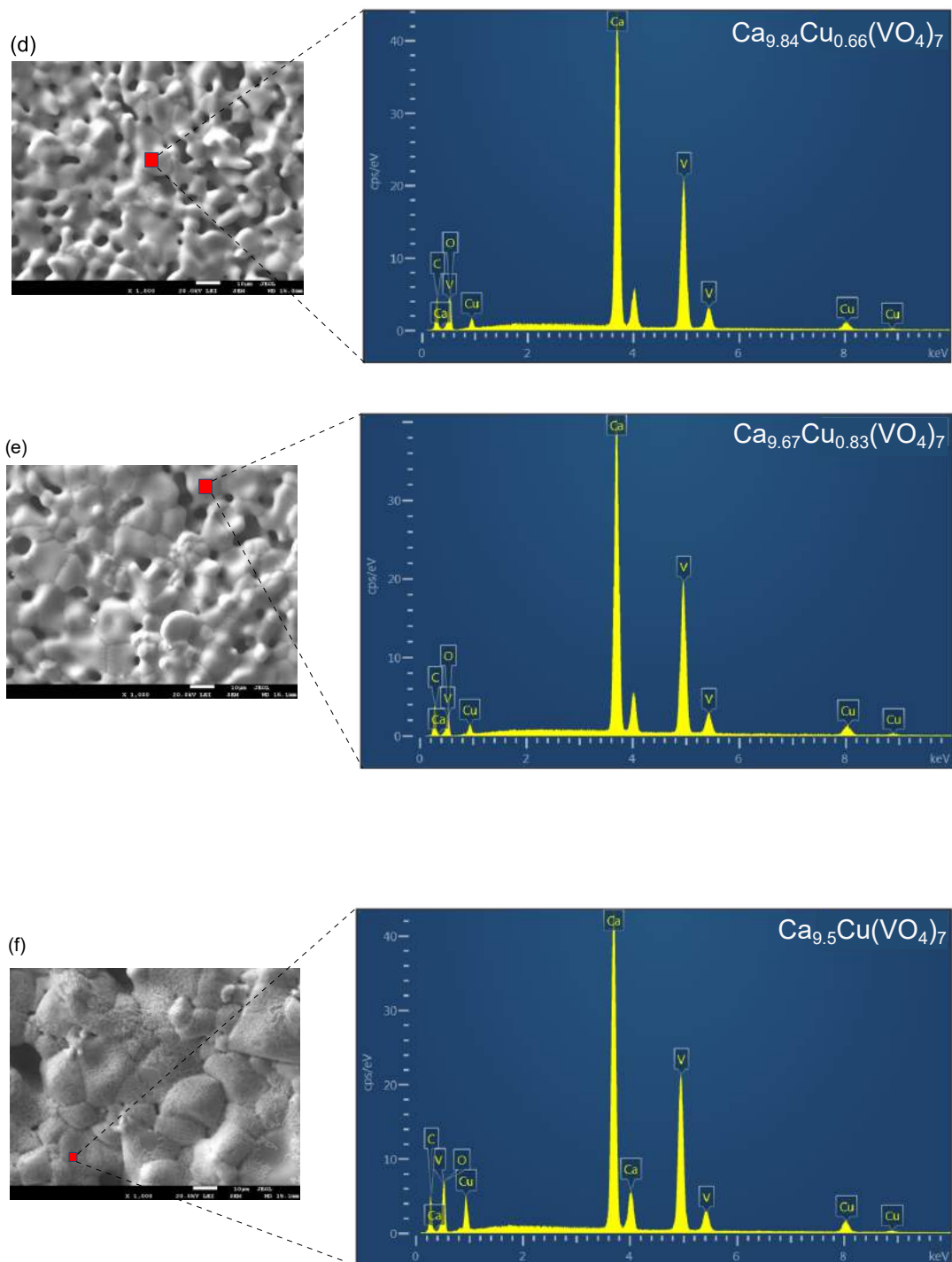
Figure A.22: SEM image and EDX spectrum of the surface of Ca$_{9.84}$Cu$_{0.66}$(VO$_4$)$_7$ sample (d), Ca$_{9.67}$Cu$_{0.83}$(VO$_4$)$_7$ sample (e) and Ca$_{9.5}$Cu(VO$_4$)$_7$ (f).

Table A.1: Unit cell size of $Ca_{10.5-x}TM_x(VO_4)_7$.

TM	x_{nom}	a (Å)	c (Å)	V (Å³)	ρ (g/cm³)
Co	0	10.81221(8)	38.0262(3)	3849.84(5)	3.171
	0.16	10.80015(23)	37.94714(87)	3833.269(147)	3.192
	0.33	10.79058(7)	37.89653(27)	3821.373(46)	3.211
	0.5	10.78074(6)	37.81965(23)	3806.668(38)	3.236
	0.66	10.77185(8)	37.73976(31)	3792.368(52)	3.250
	0.83	10.76554(8)	37.67800(29)	3781.723(49)	3.262
	1	10.76606(8)	37.67582(31)	3781.870(52)	3.262
Ni	0.16	10.80110(5)	37.96817(20)	3836.069(33)	3.191
	0.33	10.78838(5)	37.89214(21)	3819.375(34)	3.213
	0.5	10.77604(5)	37.80588(21)	3801.967(34)	3.237
	0.66	10.76527(4)	37.71474(15)	3785.225(25)	3.258
	0.83	10.76215(4)	37.68755(18)	3780.305(28)	3.264
	1	10.76226(6)	37.68798(24)	3780.420(38)	3.264
Cu	0.16	10.80307(18)	37.98879(68)	3839.551(113)	3.195
	0.33	10.79366(18)	37.93847(66)	3827.792(111)	3.211
	0.5	10.78708(7)	37.89966(27)	3819.211(45)	3.223
	0.66	10.78061(14)	37.86170(53)	3810.814(88)	3.236
	0.83	10.77581(14)	37.83003(51)	3804.230(85)	3.247
	1	10.77555(6)	37.82238(25)	3803.283(40)	3.245

Table A.2: Results of the structure refinement for Ca$_{10.5-x}$Co$_x$(VO$_4$)$_7$ for x = 0.16-0.83

site	Wyckoff position	coordination			x		
			0.16	0.33	0.5	0.66	0.83
M1	18b	x	0.20300(120)	0.19855(44)	0.19940(40)	0.19861(48)	0.19865(45)
		y	0.39490(112)	0.39479(44)	0.39503(40)	0.39515(50)	0.39588(46)
		z	0.00171(45)	0.00282(15)	0.00223(13)	0.00191(17)	0.00177(15)
M2	18b	x	0.16116(143)	0.15807(48)	0.15913(41)	0.15971(50)	0.16010(50)
		y	0.28142(124)	0.27995(38)	0.27981(33)	0.27949(42)	0.27988(41)
		z	0.19993(45)	0.20132(15)	0.20129(13)	0.20153(16)	0.20191(15)
M3	18b	x	0.18901(130)	0.18746(42)	0.18709(36)	0.18569(43)	0.18628(44)
		y	0.39510(92)	0.39678(31)	0.39854(28)	0.39728(35)	0.39674(33)
		z	0.10880(43)	0.11047(14)	0.10984(12)	0.10934(15)	0.10978(14)
M4	6a	x	0.0	0.0	0.0	0.0	0.0
		y	0.0	0.0	0.0	0.0	0.0
		z	0.07465(181)	0.07222(73)	0.07667(56)	0.07414(80)	0.07627(59)
M5	6a	x	0.0	0.0	0.0	0.0	0.0
		y	0.0	0.0	0.0	0.0	0.0
		z	0.26577(66)	0.26523(19)	0.26578(17)	0.26513(21)	0.26493(20)
V1	6a	x	0.0	0.0	0.0	0.0	0.0
		y	0.0	0.0	0.0	0.0	0.0
		z	0.0	0.0	0.0	0.0	0.0
V2	18b	x	0.30748(96)	0.31047(28)	0.31142(25)	0.31138(31)	0.30913(31)
		y	0.13353(122)	0.13665(36)	0.13810(29)	0.13809(37)	0.13613(39)
		z	0.13142(41)	0.13242(13)	0.13192(12)	0.13173(15)	0.13143(14)
V3	18b	x	0.34946(98)	0.34738(37)	0.34768(33)	0.34893(41)	0.34653(36)
		y	0.15290(108)	0.14921(39)	0.14843(35)	0.14933(43)	0.14880(38)
		z	0.23416(39)	0.23492(12)	0.23522(11)	0.23519(13)	0.23548(13)
O1	18b	x	0.15100(299)	0.15330(94)	0.15290(86)	0.15226(105)	0.15330(99)
		y	0.01469(359)	0.01215(122)	0.00652(121)	0.00729(146)	0.00781(136)
		z	0.00910(102)	0.01031(33)	0.01343(33)	0.01146(37)	0.01254(38)
O2	6a	x	0.0	0.0	0.0	0.0	0.0
		y	0.0	0.0	0.0	0.0	0.0
		z	0.45490(157)	0.45441(49)	0.45475(46)	0.45540(55)	0.45605(54)
O3	18b	x	0.26760(356)	0.26866(117)	0.25487(101)	0.26107(12)	0.25707(116)
		y	0.07878(293)	0.07064(93)	0.06459(79)	0.07032(10)	0.07151(92)
		z	0.08988(99)	0.09272(29)	0.09124(26)	0.09182(31)	0.09008(32)
O4	18b	x	0.23354(443)	0.23049(147)	0.22845(128)	0.22647(15)	0.22715(139)
		y	0.22832(419)	0.22190(139)	0.21802(124)	0.21610(14)	0.22644(137)
		z	0.14511(90)	0.14435(29)	0.14288(26)	0.14395(32)	0.14363(31)
O5	18b	x	0.27948(432)	0.28277(134)	0.28027(120)	0.28261(14)	0.28426(138)
		y	0.01241(340)	0.00952(108)	0.00821(96)	0.00574(11)	0.00750(108)
		z	0.15439(88)	0.15531(28)	0.15533(25)	0.15575(32)	0.15593(31)
O5	18b	x	0.08862(390)	0.08638(135)	0.08891(130)	0.09185(15)	0.08175(142)
		y	0.17663(355)	0.18556(111)	0.18287(98)	0.18683(11)	0.17654(119)
		z	0.30887(96)	0.30360(34)	0.30110(31)	0.30254(39)	0.30114(36)
O7	18b	x	0.38696(385)	0.40039(114)	0.40090(102)	0.40206(122)	0.40893(119)
		y	0.02553(345)	0.03365(109)	0.03090(94)	0.02853(108)	0.03040(103)
		z	0.22529(108)	0.22508(33)	0.22471(30)	0.22402(37)	0.22565(36)
O8	18b	x	0.03003(356)	0.02130(124)	0.01453(112)	0.01586(136)	0.02720(110)
		y	0.24377(390)	0.23812(137)	0.23260(117)	0.23938(140)	0.23777(133)
		z	0.37887(93)	0.37953(30)	0.37978(27)	0.38019(33)	0.37942(33)
O9	18b	x	0.16929(364)	0.16909(102)	0.16647(91)	0.16012(108)	0.16548(116)
		y	0.08722(477)	0.07784(149)	0.07343(131)	0.07253(166)	0.07103(148)
		z	0.22964(102)	0.22290(34)	0.22394(30)	0.22531(39)	0.22601(37)
O10	18b	x	0.38197(320)	0.37669(94)	0.37815(81)	0.38196(103)	0.37785(97)
		y	0.17716(392)	0.18014(122)	0.18228(107)	0.18206(126)	0.18231(123)
		z	0.27634(96)	0.27933(28)	0.27978(26)	0.28120(31)	0.27913(32)

Table A.3: Results of the structure refinement for Ca$_{10.5-x}$Ni$_x$(VO$_4$)$_7$ for x = 0.16-0.83

site	Wyckoff position	coordination			x		
			0.16	0.33	0.5	0.66	0.83
M1	18b	x	0.1974(3)	0.1975(3)	0.1993(3)	0.1975(3)	0.19716(30)
		y	0.3938(3)	0.3944(3)	0.3954(3)	0.3955(3)	0.39466(30)
		z	0.0028(1)	0.0025(1)	0.0022(1)	0.00275(9)	0.00211(10)
M2	18b	x	0.1582(3)	0.1590(3)	0.1600(3)	0.1589(30)	0.15904(3)
		y	0.2808(3)	0.2813(3)	0.2808(3)	0.2805(2)	0.28021(26)
		z	0.2009(1)	0.20119(11)	0.2014(1)	0.20241(9)	0.20209(9)
M3	18b	x	0.1873(3)	0.1864(3)	0.1874(3)	0.1860(3)	0.18580(28)
		y	0.3988(2)	0.3974(2)	0.3973(2)	0.3960(2)	0.39616(22)
		z	0.1097(1)	0.10983(11)	0.1099(1)	0.11087(9)	0.11032(9)
M4	6a	x	0.0	0.0	0.0	0.0	0.0
		y	0.0	0.0	0.0	0.0	0.0
		z	0.074(5)	0.0766(5)	0.0749(5)	0.0766(3)	0.07610(40)
M5	6a	x	0.0	0.0	0.0	0.0	0.0
		y	0.0	0.0	0.0	0.0	0.0
		z	0.2658(2)	0.2655(1)	0.2651(1)	0.2654(1)	0.26523(13)
V1	6a	x	0.0	0.0	0.0	0.0	0.0
		y	0.0	0.0	0.0	0.0	0.0
		z	0.0	0.0	0.0	0.0	0.0
V2	18b	x	0.3103(2)	0.3109(2)	0.3119(2)	0.3109(2)	0.31132(20)
		y	0.1371(3)	0.1371(3)	0.1382(3)	0.1378(2)	0.13777(24)
		z	0.1323(1)	0.1324(1)	0.13213(1)	0.1324(1)	0.13225(9)
V3	18b	x	0.3484(3)	0.3479(3)	0.3471(3)	0.3466(2)	0.34634(25)
		y	0.1498(3)	0.1498(3)	0.1483(3)	0.1484(2)	0.14874(25)
		z	0.2347(1)	0.2350(1)	0.2352(1)	0.2361(1)	0.23570(8)
O1	18b	x	0.1558(8)	0.1565(8)	0.1542(7)	0.1557(6)	0.15514(69)
		y	0.0093(10)	0.0106(10)	0.0090(9)	0.0121(8)	0.01033(89)
		z	0.0123(3)	0.0119(3)	0.0110(3)	0.0121(2)	0.01201(24)
O2	6a	x	0.0	0.0	0.0	0.0	0.0
		y	0.0	0.0	0.0	0.0	0.0
		z	0.4546(4)	0.4543(4)	0.4550(4)	0.4555(3)	0.45561(36)
O3	18b	x	0.2683(9)	0.2680(9)	0.2624(9)	0.2565(7)	0.25642(79)
		y	0.0692(7)	0.0715(7)	0.0689(7)	0.0665(6)	0.06585(66)
		z	0.0911(2)	0.0911(2)	0.0916(2)	0.09154(19)	0.09081 (21)
O4	18b	x	0.2306(11)	0.2304(11)	0.2320(10)	0.2308(8)	0.22895(91)
		y	0.2257(10)	0.2256(10)	0.2235(10)	0.2310(8)	0.22928(88)
		z	0.1446(2)	0.1445(2)	0.1444(2)	0.14583(19)	0.14539(21)
O5	18b	x	0.2805(10)	0.2818(10)	0.2825(10)	0.2801(8)	0.28095(89)
		y	-0.0114(9)	-0.0105(8)	-0.0085(8)	-0.0089(7)	0.00961(73)
		z	0.1561(2)	0.1565(2)	0.1559(2)	0.15765(19)	0.15819(21)
O6	18b	x	0.0873(10)	0.0857(10)	0.0852(10)	0.0808(8)	0.08264(93)
		y	0.1843(8)	0.1806(9)	0.1792(8)	0.1722(7)	0.17572(78)
		z	0.3045(3)	0.3032(3)	0.3022(3)	0.3025(2)	0.30255(23)
O7	18b	x	0.3998(9)	0.3998(9)	0.3999(8)	0.4006(7)	0.40023(81)
		y	0.0329(8)	0.0309(8)	0.0308(8)	0.0300(7)	0.02886(73)
		z	0.2240(3)	0.2246(3)	0.2252(3)	0.2254(2)	0.22506(24)
O8	18b	x	0.0189(10)	0.0223(9)	0.0225(9)	0.0275(7)	0.02550(75)
		y	0.2331(10)	0.2357(10)	0.2361(10)	0.2365(8)	0.23795(86)
		z	0.3804(2)	0.3800(2)	0.3795(2)	0.37923(20)	0.37894(21)
O9	18b	x	0.1705(8)	0.1701(8)	0.1697(8)	0.1696(7)	0.16738(78)
		y	0.0762(11)	0.0749(11)	0.0752(11)	0.0717(8)	0.07076(94)
		z	0.2219(3)	0.2227(3)	0.2249(3)	0.2252(2)	0.22601(23)
O10	18b	x	0.3752(7)	0.3757(7)	0.3785(7)	0.3788(6)	0.37823(64)
		y	0.1826(10)	0.1824(10)	0.1831(9)	0.1836(8)	0.18285(84)
		z	0.2794(2)	0.2797(2)	0.2794(2)	0.27974(19)	0.28022(20)

Table A.4: Results of the structure refinement for Ca$_{10.5-x}$Cu$_x$(VO$_4$)$_7$ for x = 0.16-0.83

site	Wyckoff position	coordination	x				
			0.16	0.33	0.5	0.66	0.83
M1	18b	x	0.20400(87)	0.20311(74)	0.19913(39)	0.19975(63)	0.20041(54)
		y	0.39463(90)	0.39512(81)	0.39599(39)	0.39323(68)	0.39487(60)
		z	0.00226(31)	0.00162(29)	0.00153(14)	0.00052(24)	0.00050(20)
M2	18b	x	0.16085(90)	0.16250(77)	0.15918(42)	0.15955(68)	0.16088(58)
		y	0.28102(81)	0.28264(70)	0.28139(35)	0.28008(57)	0.28111(49)
		z	0.20025(29)	0.19955(27)	0.20022(13)	0.19961(23)	0.19988(19)
M3	18b	x	0.18868(98)	0.18971(75)	0.18706(37)	0.18691(57)	0.18647(49)
		y	0.39699(69)	0.39868(59)	0.39776(29)	0.39821(47)	0.39814(40)
		z	0.10871(29)	0.10874(26)	0.10892(13)	0.10858(21)	0.10861(19)
M4	6a	x	0.0	0.0	0.0	0.0	0.0
		y	0.0	0.0	0.0	0.0	0.0
		z	0.07546(124)	0.07296(106)	0.07619(64)	0.06982(116)	0.07243(92)
M5	6a	x	0.0	0.0	0.0	0.0	0.0
		y	0.0	0.0	0.0	0.0	0.0
		z	0.26548(45)	0.26398(33)	0.26494(17)	0.26380(27)	0.26398(23)
V1	6a	x	0.0	0.0	0.0	0.0	0.0
		y	0.0	0.0	0.0	0.0	0.0
		z	0.0	0.0	0.0	0.0	0.0
V2	18b	x	0.30895(64)	0.31086(51)	0.31161(26)	0.31277(41)	0.31262(35)
		y	0.13384(80)	0.13424(65)	0.13797(32)	0.13736(49)	0.13841(42)
		z	0.13171(27)	0.13115(24)	0.13124(12)	0.13077(19)	0.13051(17)
V3	18b	x	0.34822(82)	0.34818(71)	0.34884(34)	0.34866(58)	0.34773(51)
		y	0.15433(88)	0.15138(74)	0.15021(35)	0.14994(60)	0.15038(52)
		z	0.23438(27)	0.23495(23)	0.23424(11)	0.23394(18)	0.23392(15)
O1	18b	x	0.14989(208)	0.15121(174)	0.15403(91)	0.15629(145)	0.15313(122)
		y	0.00789(256)	0.00554(213)	0.00795(122)	0.00721(191)	0.00630(166)
		z	0.00919(73)	0.00777(56)	0.01159(33)	0.00926(50)	0.00966(43)
O2	6a	x	0.0	0.0	0.0	0.0	0.0
		y	0.0	0.0	0.0	0.0	0.0
		z	0.45103(110)	0.45300(86)	0.45348(48)	0.45288(74)	0.45268(66)
O3	18b	x	0.25564(248)	0.26955(220)	0.26840(111)	0.26469(177)	0.26502(151)
		y	0.07136(203)	0.06666(170)	0.07319(90)	0.07053(140)	0.06886(119)
		z	0.09112(69)	0.08939(57)	0.09158(28)	0.09074(43)	0.09139(37)
O4	18b	x	0.22423(315)	0.23097(247)	0.22312(129)	0.23247(209)	0.22702(177)
		y	0.22377(301)	0.19674(205)	0.20931(120)	0.20610(188)	0.20474(156)
		z	0.14396(66)	0.14437(54)	0.14246(28)	0.14270(45)	0.14234(38)
O5	18b	x	0.28686(303)	0.29115(239)	0.28194(126)	0.28187(197)	0.28397(170)
		y	0.00478(249)	0.00082(191)	0.00850(102)	0.00290(159)	0.00167(136)
		z	0.15293(64)	0.15382(55)	0.15435(26)	0.15396(44)	0.15442(37)
O6	18b	x	0.08516(272)	0.09116(216)	0.09040(127)	0.09600(204)	0.09473(177)
		y	0.18633(251)	0.19788(178)	0.18816(97)	0.19368(154)	0.18903(134)
		z	0.30819(72)	0.30275(63)	0.30187(33)	0.30142(53)	0.29952(45)
O7	18b	x	0.39283(278)	0.39716(204)	0.40329(105)	0.39709(167)	0.39638(144)
		y	0.02534(238)	0.02939(185)	0.03182(101)	0.02887(153)	0.02810(131)
		z	0.22314(74)	0.22427(58)	0.22413(31)	0.22378(50)	0.22339(42)
O8	18b	x	0.02177(276)	0.00488(256)	0.00899(127)	0.00065(201)	0.00104(176)
		y	0.23691(297)	0.23780(227)	0.23627(121)	0.23164(193)	0.23287(166)
		z	0.38138(70)	0.38065(57)	0.37927(28)	0.37926(47)	0.37933(40)
O9	18b	x	0.16981(263)	0.16191(166)	0.16535(91)	0.16314(141)	0.16676(123)
		y	0.06834(297)	0.07309(264)	0.07376(138)	0.07499(225)	0.07531(192)
		z	0.22590(83)	0.22397(68)	0.22198(32)	0.22396(55)	0.22210(43)
O10	18b	x	0.37551(214)	0.37918(172)	0.37850(91)	0.38054(141)	0.37942(117)
		y	0.17194(264)	0.17612(209)	0.17798(115)	0.18060(178)	0.17980(152)
		z	0.27814(67)	0.27769(54)	0.27846(27)	0.27869(42)	0.27825(36)

Appendix B

Structures of $Ca_{10.5-x}TM_x(VO_4)_7$ compounds at high temperature
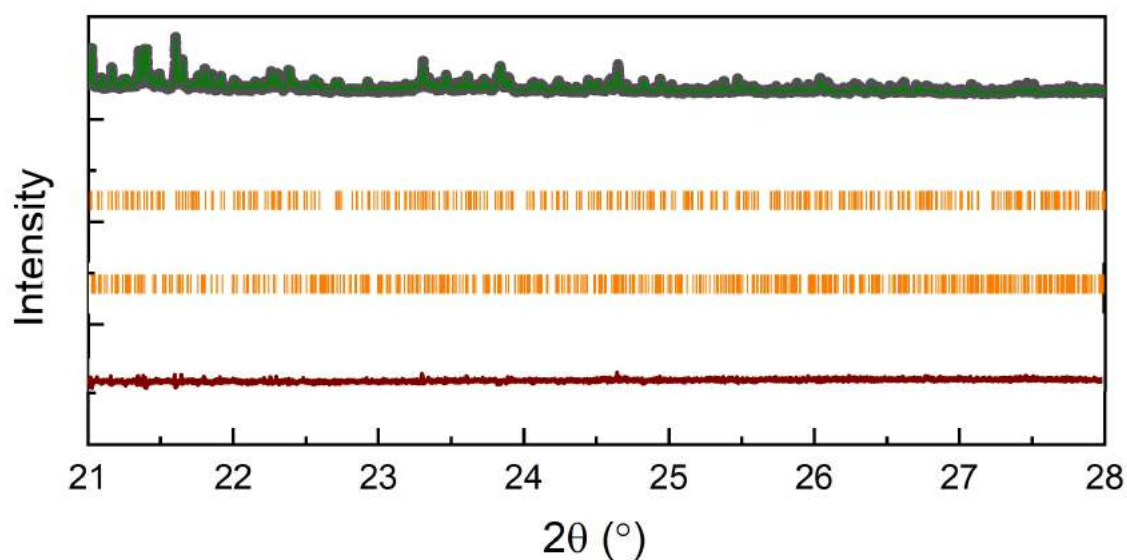
Figure B.1: Illustration of Rietveld refinement at the angles between $20°$ and $40°$ (2θ) for $Ca_{10}TM_{0.5}(VO_4)_7$ at 850 K.

Table B.1: Unit cell size of $Ca_{10}Co_{0.5}(VO_4)_7$.

T (K)	a (Å)	c (Å)	V (Å³)
300	10.78647(1)	37.83710 (5)	3812.476(8)
500	10.82000(1)	37.94221(5)	3846.872(8)
800	10.87358(1)	38.11081(5)	3902.330(9)
850	10.88250(1)	38.14127(5)	3911.857(8)
900	10.89106(1)	38.17179(5)	3921.148(7)
950	10.89953(1)	38.20309(4)	3930.471(7)
1000	10.90776(1)	38.23421(4)	3939.619(6)
1100	10.92431(1)	38.29881(4)	3958.254(6)

Table B.2: Unit cell size of $Ca_{10}Cu_{0.5}(VO_4)_7$.

T (K)	a (Å)	c (Å)	V (Å³)
300	10.79239(2)	37.91392(7)	3824.412(12)
400	10.80824(2)	37.96552(8)	3840.876(12)
650	10.84306(2)	38.08073(7)	3877.395(12)
750	10.86863(2)	38.16288(8)	3904.105(13)
850	10.88708(2)	38.22654(6)	3923.905(10)
950	10.90857(1)	38.30824(5)	3947.827(8)
1150	10.95303(1)	38.47176(4)	3997.065(6)

Appendix C

Structures of Ca$_{10.5-x}$TM$_x$(VO$_4$)$_7$ compounds at low temperature
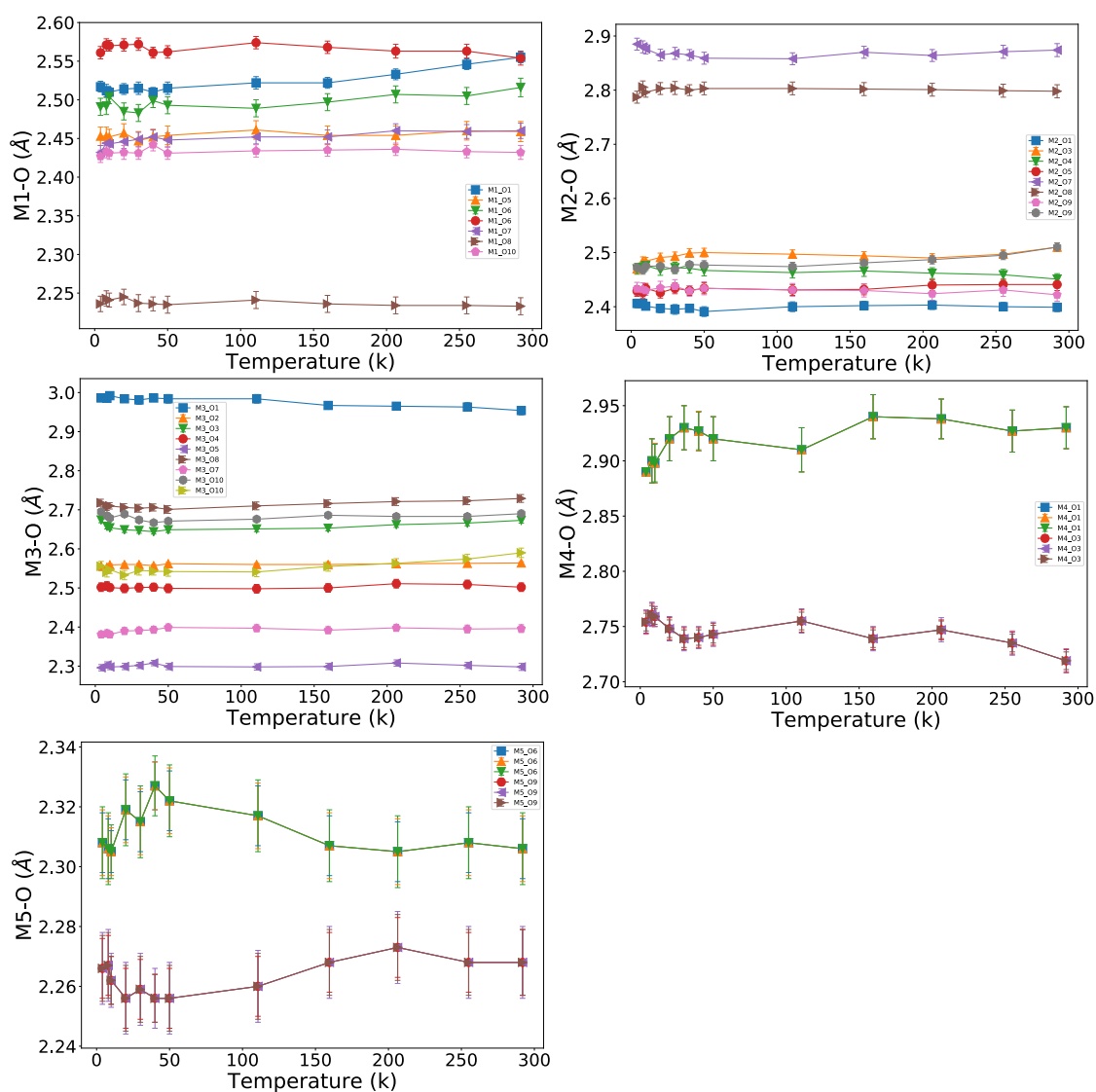
Ca$_3$(VO$_4$)$_2$

Figure C.1: Temperature evolution of M-O distances for Ca$_3$(VO$_4$)$_2$.

Table C.1: Results of the structure refinement for Ca$_3$(VO$_4$)$_2$ at low temperature

site	Wyckoff position	coordination	T (K)			
			4	50	100	200
M1	18b	x	0.19677(26)	0.19620(27)	0.19619(27)	0.19655(28)
		y	0.39265(26)	0.39238(26)	0.39268(26)	0.39311(27)
		z	0.00273(9)	0.00255(10)	0.00254(10)	0.00274(10)
M2	18b	x	0.15770(28)	0.15681(30)	0.15661(30)	0.15726(30)
		y	0.27893(25)	0.27893(26)	0.27884(26)	0.27917(27)
		z	0.20013(9)	0.19997(10)	0.19998(10)	0.20020(10)
M3	18b	x	0.18629(28)	0.18580(28)	0.18597(28)	0.18611(29)
		y	0.39669(22)	0.39662(23)	0.39667(23)	0.39675(23)
		z	0.10917(9)	0.10896(9)	0.10903(9)	0.10919(9)
M4	6a	x	0.0	0.0	0.0	0.0
		y	0.0	0.0	0.0	0.0
		z	0.07567(57)	0.07620(60)	0.07621(58)	0.07651(54)
M5	6a	x	0.0	0.0	0.0	0.0
		y	0.00000(0)	0.00000(0)	0.00000(0)	0.00000(0)
		z	0.26530(14)	0.26509(14)	0.26507(14)	0.26528(15)
V1	6a	x	0.0	0.0	0.0	0.0
		y	0.0	0.0	0.0	0.0
		z	0.0	0.0	0.0	0.0
V2	18b	x	0.31071(19)	0.31079(20)	0.31100(20)	0.31098(20)
		y	0.13602(23)	0.13666(24)	0.13680(24)	0.13650(24)
		z	0.13175(8)	0.13158(9)	0.13164(8)	0.13186(8)
V3	18b	x	0.34903(23)	0.34961(23)	0.34954(24)	0.34930(24)
		y	0.15078(23)	0.15078(24)	0.15059(24)	0.15090(24)
		z	0.23442(8)	0.23417(8)	0.23425(8)	0.23448(8)
O1	18b	x	0.15201(70)	0.15379(72)	0.15291(71)	0.15300(71)
		y	0.00896(94)	0.01028(96)	0.01023(95)	0.01101(94)
		z	0.01210(24)	0.01197(25)	0.01196(25)	0.01162(24)
O2	6a	x	0.0	0.0	0.0	0.0
		y	0.0	0.0	0.0	0.0
		z	0.45277(36)	0.45335(37)	0.45313(36)	0.45331(37)
O3	18b	x	0.27925(80)	0.27775(83)	0.27900(82)	0.27834(83)
		y	0.08070(74)	0.07872(77)	0.07904(77)	0.07941(76)
		z	0.09175(22)	0.09208(22)	0.09207(22)	0.09207(22)
O4	18b	x	0.22580(89)	0.22456(92)	0.22405(91)	0.22451(93)
		y	0.22041(86)	0.22045(89)	0.22033(88)	0.21984(89)
		z	0.14301(22)	0.14288(23)	0.14305(22)	0.14342(23)
O5	18b	x	0.28157(90)	0.28232(92)	0.28180(91)	0.28265(93)
		y	0.01674(81)	0.01540(84)	0.01571(83)	0.01502(85)
		z	0.15277(20)	0.15253(20)	0.15247(20)	0.15279(20)
O6	18b	x	0.08744(89)	0.08836(92)	0.08765(91)	0.08866(92)
		y	0.18276(74)	0.18403(76)	0.18420(75)	0.18343(76)
		z	0.30620(26)	0.30622(27)	0.30588(26)	0.30576(26)
O7	18b	x	0.40643(81)	0.40404(84)	0.40402(83)	0.40364(84)
		y	0.04063(79)	0.04079(82)	0.04020(81)	0.04067(82)
		z	0.22463(22)	0.22437(23)	0.22452(23)	0.22480(23)
O8	18b	x	0.01856(93)	0.01762(98)	0.01863(96)	0.01852(98)
		y	0.23896(85)	0.23817(88)	0.23883(87)	0.23844(89)
		z	0.38022(21)	0.38026(22)	0.38026(22)	0.38024(22)
O9	18b	x	0.17324(76)	0.17298(78)	0.17283(77)	0.17370(78)
		y	0.07717(96)	0.07793(99)	0.07786(98)	0.07904(100)
		z	0.22358(27)	0.22373(28)	0.22346(27)	0.22352(27)
O10	18b	x	0.37626(77)	0.38016(79)	0.37984(79)	0.37739(79)
		y	0.18287(89)	0.18396(92)	0.18416(92)	0.18225(92)
		z	0.27727(20)	0.27741(21)	0.27727(21)	0.27730(21)

Ca$_{10}$Ni$_{0.5}$(VO$_4$)$_7$
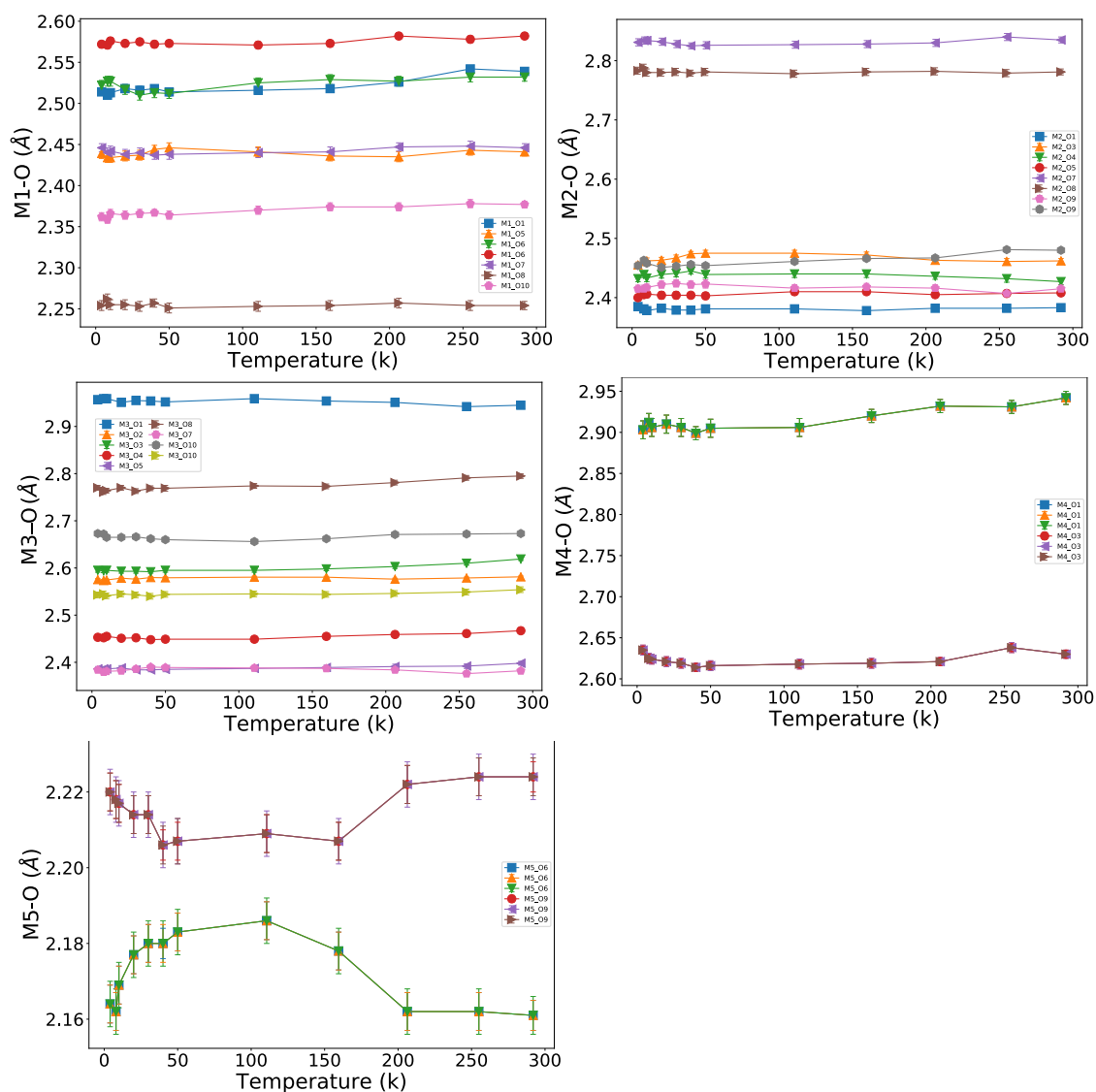
Figure C.2: Temperature evolution of M-O distances for Ca$_{10}$Ni$_{0.5}$(VO$_4$)$_7$.

Table C.2: Results of the structure refinement for Ca$_{10}$Ni$_{0.5}$(VO$_4$)$_7$ for selected temperatures at low temperature range

site	Wyckoff position	coordination	T (K)			
			4	50	100	200
M1	18b	x	0.19791(15)	0.19748(16)	0.19767(15)	0.19786(15)
		y	0.39501(15)	0.39452(16)	0.39428(15)	0.39494(15)
		z	0.00226(5)	0.00186(5)	0.00189(5)	0.00226(5)
M2	18b	x	0.15906(15)	0.15872(16)	0.15887(15)	0.15895(15)
		y	0.27990(14)	0.27992(14)	0.27988(14)	0.28019(14)
		z	0.20173(5)	0.20131(5)	0.20132(5)	0.20165(5)
M3	18b	x	0.18570(15)	0.18593(15)	0.18624(15)	0.18631(15)
		y	0.39581(12)	0.39564(13)	0.39557(13)	0.39591(12)
		z	0.10991(5)	0.10953(5)	0.10950(5)	0.10987(5)
M4	6a	x	0.0	0.0	0.0	0.0
		y	0.0	0.0	0.0	0.0
		z	0.07643(26)	0.07596(26)	0.07622(25)	0.07707(23)
M5	6a	x	0.0	0.0	0.0	0.0
		y	0.00000(0)	0.00000(0)	0.00000(0)	0.00000(0)
		z	0.26527(6)	0.26492(7)	0.26491(6)	0.26520(6)
V1	6a	x	0.0	0.0	0.0	0.0
		y	0.00000(0)	0.00000(0)	0.00000(0)	0.00000(0)
		z	0.00000(0)	0.00000(0)	0.00000(0)	0.00000(0)
V2	18b	x	0.31126(11)	0.31153(11)	0.31151(11)	0.31129(11)
		y	0.13691(13)	0.13737(13)	0.13740(13)	0.13687(12)
		z	0.13199(4)	0.13171(5)	0.13170(5)	0.13200(4)
V3	18b	x	0.34859(13)	0.34925(13)	0.34912(13)	0.34854(13)
		y	0.14953(13)	0.15009(14)	0.15022(13)	0.15026(13)
		z	0.23524(4)	0.23486(5)	0.23488(4)	0.23526(4)
O1	18b	x	0.15442(42)	0.15487(43)	0.15475(42)	0.15478(41)
		y	0.00876(54)	0.00963(55)	0.00965(54)	0.01001(53)
		z	0.01246(13)	0.01203(14)	0.01218(14)	0.01232(13)
O2	6a	x	0.0	0.0	0.0	0.0
		y	0.0	0.0	0.0	0.0
		z	0.45655(20)	0.45650(21)	0.45654(20)	0.45643(20)
O3	18b	x	0.26635(45)	0.26408(46)	0.26425(45)	0.26517(44)
		y	0.06993(40)	0.06926(42)	0.06916(41)	0.06947(40)
		z	0.09158(12)	0.09146(12)	0.09149(12)	0.09151(11)
O4	18b	x	0.22834(49)	0.22804(51)	0.22766(50)	0.22854(49)
		y	0.22792(48)	0.22745(50)	0.22712(49)	0.22746(48)
		z	0.14468(11)	0.14413(12)	0.14410(12)	0.14470(11)
O5	18b	x	0.28108(49)	0.28084(51)	0.28113(50)	0.28192(49)
		y	0.01072(42)	0.01019(44)	0.01000(43)	0.01063(42)
		z	0.15586(11)	0.15527(11)	0.15516(11)	0.15577(11)
O6	18b	x	0.08524(50)	0.08522(52)	0.08620(51)	0.08480(50)
		y	0.17626(42)	0.17732(43)	0.17801(42)	0.17614(41)
		z	0.30265(13)	0.30276(14)	0.30265(13)	0.30242(13)
O7	18b	x	0.40401(45)	0.40412(47)	0.40381(46)	0.40394(45)
		y	0.03331(42)	0.03347(44)	0.03363(43)	0.03299(42)
		z	0.22487(12)	0.22423(12)	0.22428(12)	0.22480(12)
O8	18b	x	0.02471(46)	0.02404(48)	0.02431(47)	0.02518(46)
		y	0.23866(46)	0.23903(48)	0.23927(47)	0.23961(46)
		z	0.37974(11)	0.37935(12)	0.37929(12)	0.37962(11)
O9	18b	x	0.17055(41)	0.16965(43)	0.16965(42)	0.17085(41)
		y	0.07557(53)	0.07502(55)	0.07557(54)	0.07648(53)
		z	0.22422(13)	0.22417(14)	0.22412(13)	0.22426(13)
O10	18b	x	0.37888(41)	0.38033(42)	0.38065(42)	0.37927(40)
		y	0.18368(46)	0.18399(48)	0.18427(47)	0.18416(46)
		z	0.27888(11)	0.27852(12)	0.27843(11)	0.27867(11)

Ca$_{10}$Cu$_{05}$(VO$_4$)$_7$
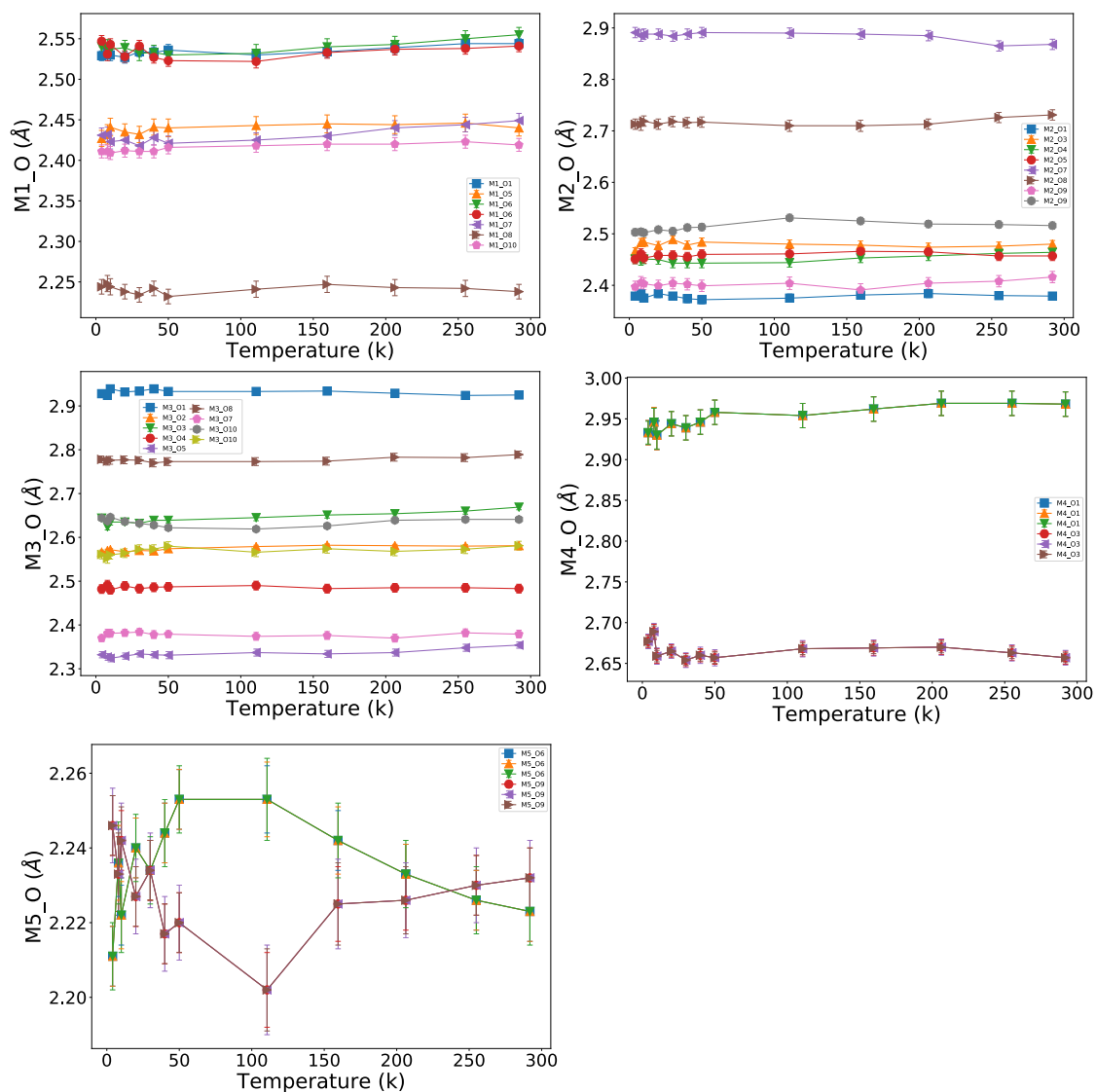
Figure C.3: Temperature evolution of M-O distances for Ca$_{10}$Cu$_{05}$(VO$_4$)$_7$.

Table C.3: Results of the structure refinement for Ca$_{10}$Cu$_{05}$(VO$_4$)$_7$ for selected temperatures at low temperature range

site	Wyckoff position	coordination	T (K)			
			4	50	100	200
M1	18b	x	0.19820(23)	0.19819(24)	0.19824(26)	0.19827(25)
		y	0.39400(23)	0.39386(24)	0.39373(26)	0.39420(25)
		z	0.00182(8)	0.00163(8)	0.00155(9)	0.00178(9)
M2	18b	x	0.16060(25)	0.16045(26)	0.16021(27)	0.16025(27)
		y	0.28033(23)	0.28017(23)	0.28017(25)	0.28060(24)
		z	0.20046(8)	0.20027(8)	0.20017(9)	0.20049(9)
M3	18b	x	0.18753(23)	0.18780(24)	0.18792(25)	0.18758(25)
		y	0.39666(19)	0.39668(19)	0.39647(20)	0.39606(20)
		z	0.10932(8)	0.10916(8)	0.10902(8)	0.10920(8)
M4	6a	x	0.0	0.0	0.0	0.0
		y	0.0	0.0	0.0	0.0
		z	0.07609(41)	0.07696(42)	0.07657(44)	0.07696(41)
M5	6a	x	0.0	0.0	0.0	0.0
		y	0.0	0.0	0.0	0.0
		z	0.26467(10)	0.26445(11)	0.26449(11)	0.26465(11)
V1	6a	x	0.00000(0)	0.00000(0)	0.00000(0)	0.00000(0)
		y	0.00000(0)	0.00000(0)	0.00000(0)	0.00000(0)
		z	0.00000(0)	0.00000(0)	0.00000(0)	0.00000(0)
V2	18b	x	0.31162(17)	0.31214(17)	0.31248(18)	0.31208(18)
		y	0.13678(20)	0.13752(21)	0.13791(21)	0.13733(21)
		z	0.13136(7)	0.13118(7)	0.13114(8)	0.13133(8)
V3	18b	x	0.34908(21)	0.34976(21)	0.35015(23)	0.34932(22)
		y	0.15067(22)	0.15114(23)	0.15157(24)	0.15152(23)
		z	0.23428(7)	0.23411(7)	0.23407(7)	0.23430(7)
O1	18b	x	0.15416(63)	0.15465(65)	0.15458(68)	0.15400(66)
		y	0.01080(81)	0.01164(85)	0.01108(89)	0.01115(86)
		z	0.01117(21)	0.01133(22)	0.01114(23)	0.01097(22)
O2	6a	x	0.0	0.0	0.0	0.0
		y	0.0	0.0	0.0	0.0
		z	0.45554(31)	0.45640(32)	0.45657(33)	0.45634(33)
O3	18b	x	0.27140(72)	0.26972(74)	0.27076(78)	0.27115(76)
		y	0.07478(62)	0.07384(65)	0.07474(68)	0.07583(66)
		z	0.09139(19)	0.09151(19)	0.09141(20)	0.09157(20)
O4	18b	x	0.22537(78)	0.22425(80)	0.22377(84)	0.22364(81)
		y	0.22105(77)	0.22014(79)	0.21945(82)	0.21961(80)
		z	0.14331(18)	0.14336(19)	0.14331(20)	0.14333(20)
O5	18b	x	0.28277(81)	0.28209(85)	0.28186(88)	0.28224(86)
		y	0.01271(67)	0.01175(70)	0.01110(73)	0.01141(71)
		z	0.15326(17)	0.15272(18)	0.15260(18)	0.15284(18)
O6	18b	x	0.08825(79)	0.08971(82)	0.08980(86)	0.08952(83)
		y	0.17874(66)	0.18031(69)	0.18043(72)	0.18005(70)
		z	0.30310(22)	0.30406(24)	0.30411(25)	0.30355(24)
O7	18b	x	0.40747(70)	0.40768(74)	0.40761(77)	0.40684(75)
		y	0.03844(68)	0.03914(71)	0.03923(74)	0.03843(73)
		z	0.22427(19)	0.22377(20)	0.22378(21)	0.22429(20)
O8	18b	x	0.02141(78)	0.01962(82)	0.02008(86)	0.02114(83)
		y	0.24316(73)	0.24232(76)	0.24349(79)	0.24374(77)
		z	0.37895(18)	0.37871(19)	0.37873(19)	0.37882(19)
O9	18b	x	0.17299(65)	0.17163(69)	0.17142(73)	0.17207(70)
		y	0.07925(89)	0.07912(94)	0.07976(99)	0.07963(95)
		z	0.22343(22)	0.22382(24)	0.22451(25)	0.22404(24)
O10	18b	x	0.37957(64)	0.38009(68)	0.38200(71)	0.38045(69)
		y	0.18289(76)	0.18123(78)	0.18304(82)	0.18314(80)
		z	0.27715(17)	0.27689(18)	0.27695(19)	0.27705(18)
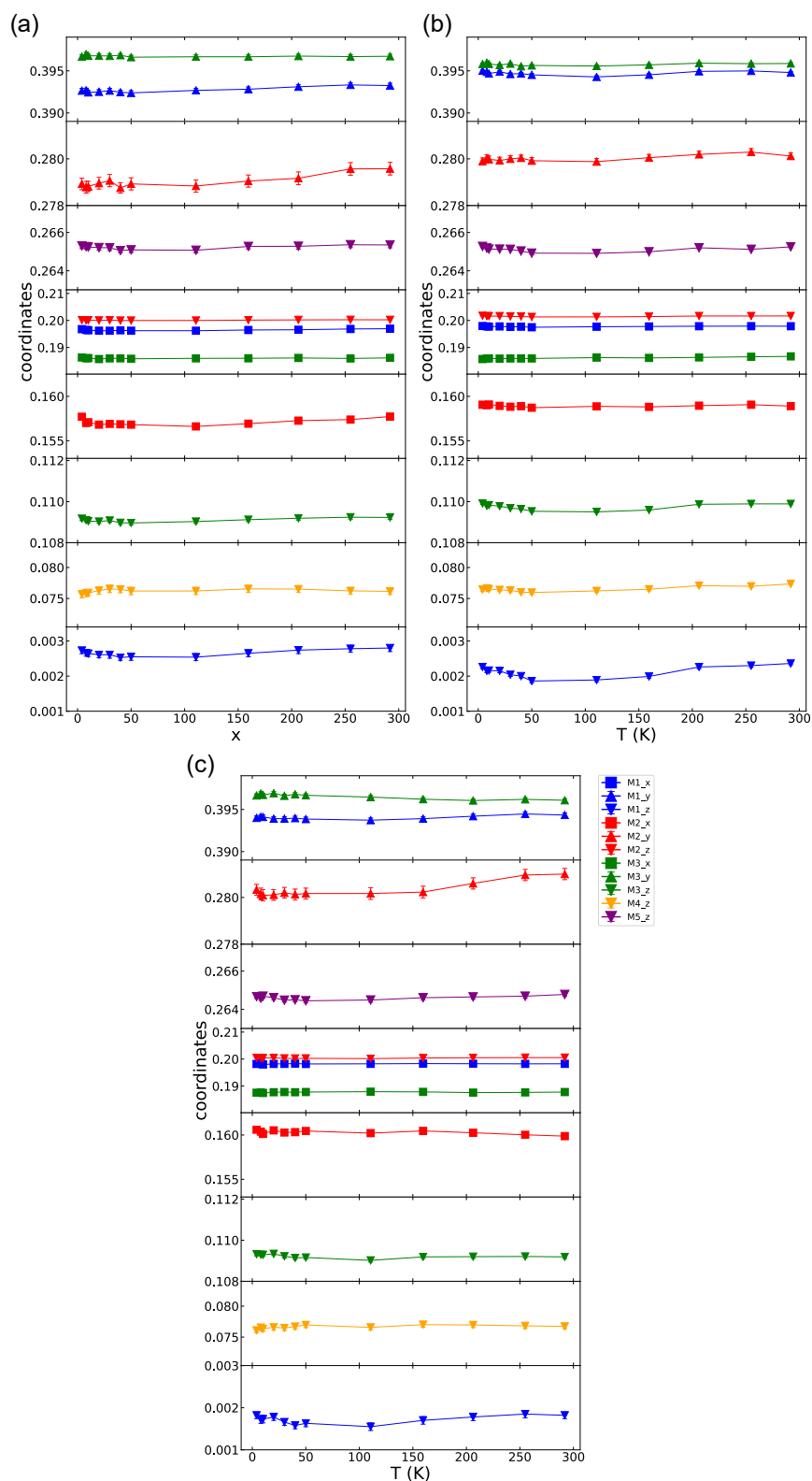
Figure C.4: temperature dependence of atomic coordinates of the 5 Ca-sites of (a) $Ca_3(VO_4)_2$, (b) $Ca_{10}Ni_{0.5}(VO_4)_7$ and (c) $Ca_{10}Cu_{0.5}(VO_4)_7$.

Bibliography

[1] L. H. Brixner and P. A. Flournoy. "Calcium Orthovanadate $Ca_3(VO_4)_2$ -A New Laser Host Crystal". In: *J. Electrochem. Soc.* 112 (1965), p. 303. DOI: 10.1016/j.saa.2019.03.041.

[2] R. Gopal and C. Calvo. "The structure of $Ca_3(VO_4)_2$". In: *Z. Krist.* 137.1 (1973), pp. 67–85. DOI: 10.1524/zkri.1973.137.1.67.

[3] V. A. Morozov, A. A. Belik, R. N. Kotov, I. A. Presnyakov, S. S. Khasanov, and B. I. Lazoryak. "Crystal structures of double calcium and alkali metal phosphates $Ca_{10}M(PO_4)_7$ (M = Li, Na, K)". In: *Crystallogr. Rep* 45.1 (2000), pp. 13–20. DOI: 10.1134/1.171129.

[4] S. Sun, L. Zhang, Y. Huang, Z. Lin, and G. Wang. "Flux-Czochralski growth of $Ca_9Y(PO_4)_7$ crystal". In: *J. Cryst. Growth* 392 (2014), pp. 98–101. DOI: 10.1016/j.jcrysgro.2014.01.057.

[5] G. Renaudin, S. Gomes, and J. M. Nedelec. "First-row transition metal doping in calcium phosphate bioceramics: A detailed crystallographic study". In: *Materials (Basel).* 10.1 (2017), pp. 1–22. DOI: 10.3390/ma10010092.

[6] Z. Leng, R. Li, L. Li, D. Xue, D. Zhang, G. Li, X. Chen, and Y. Zhang. "Preferential neighboring substitution-triggered full visible spectrum emission in single-phased $Ca_{10.5-x}Mg_x(PO_4)_7$:Eu^{2+} phosphors for high color-rendering white LEDs". In: *ACS Appl. Mater. Interfaces* 10.39 (2018), pp. 33322–33334. DOI: 10.1021/acsami.8b11879.

[7] K. Yoshida, H. Hyuga, N. Kondo, H. Kita, M. Sasaki, M. Mitamura, K. Hashimoto, and Y. Toda. "Substitution model of monovalent (Li, Na, and K), divalent (Mg), and trivalent (Al) metal ions for β-tricalcium phosphate". In: *J. Am. Ceram. Soc.* 89.2 (2006), pp. 688–690. DOI: 10.1111/j.1551-2916.2005.00727.x.

[8] K. Spaeth, F. Goetz-Neunhoeffer, and K. Hurle. "Cu^{2+} doped β-tricalcium phosphate: Solid solution limit and crystallographic characterization by rietveld refinement". In: *J. Solid State Chem.* 285.February (2020), p. 121225. DOI: 10.1016/j.jssc.2020.121225.

[9] M. Neuburger. "Disorder in crystal structures: new approaches in finding the best model". PhD Thesis. Universität Basel, 2012, p. 12.

[10] B. Dickens, L. W. Schroeder, and W. E. Brown. "Crystallographic studies of the role of Mg as a stabilizing impurity in β-Ca$_3$(PO$_4$)$_2$. The crystal structure of pure β-Ca$_3$(PO$_4$)$_2$". In: *J. Solid State Chem.* 10.3 (1974), pp. 232–248. DOI: 10.1016/0022-4596(74)90030-9.

[11] M. Yashima, A. Sakai, T. Kamiyama, and A. Hoshikawa. "Crystal structure analysis of β-tricalcium phosphate Ca$_3$(PO$_4$)$_2$ by neutron powder diffraction". In: *J. Solid State Chem.* 175.2 (2003), pp. 272–277.

[12] P. Bechthold, J. Liebertz, and U. Deserno. "Linear and nonlinear optical properties of Ca$_3$(VO$_4$)$_2$". In: *Opt. Commun.* 27.3 (1978), pp. 393–398. DOI: 10.1016/0030-4018(78)90407-8.

[13] L. H. Andrade, D. R. Ardila, J. P. Andreeta, and M. S. Li. "Optical properties of Nd^{3+}-doped Ca$_3$(VO$_4$)$_2$ single crystal fiber". In: *Opt. Mater. (Amst).* 22.4 (2003), pp. 369–375. DOI: 10.1016/S0925-3467(02)00371-3.

[14] X. Chen, N. Zhuang, X. Hu, F. Zhuang, and J. Chen. "Growth and spectral properties of self-frequency doubling crystal, Nd:Ca$_{9.03}$Na$_{1.08}$La$_{0.62}$(VO$_4$)$_7$". In: *Appl. Phys. B* 88.3 (2007), pp. 449–455. DOI: 10.1007/s00340-007-2736-1.

[15] L. Li, G. Wang, Y. Huang, L. Zhang, Z. Lin, and G. Wang. "Crystal growth and spectral properties of Nd^{3+}:Ca$_9$Gd(VO$_4$)$_7$ crystal". In: *J. Cryst. Growth* 314.1 (2011), pp. 331–335. DOI: 10.1016/j.jcrysgro.2010.11.114.

[16] J. Fan, G. Wang, and F. Yuan. "Growth and characterization of new laser crystal Nd^{3+}:Ca$_{2.85}$Gd$_{0.1}$(VO$_4$)$_2$". In: *J. Rare Earths* 30.4 (2012), pp. 335–338. DOI: 10.1016/S1002-0721(12)60048-9.

[17] Z. Lin, F. Yuan, S. Sun, W. Zhao, L. Zhang, Y. Huang, and G. Wang. "Growth, thermal and spectral properties of Nd^{3+}:YCa$_9$i(VO$_4$)$_7$ crystal". In: *J. Cryst. Growth* 372 (2013), pp. 78–81. DOI: 10.1016/j.jcrysgro.2013.03.019.

[18] P. A. Loiko, A. S. Yasukevich, A. E. Gulevich, M. P. Demesh, M. B. Kosmyna, B. P. Nazarenko, V. M. Puzikov, A. N. Shekhovtsov, A. A. Kornienko, E. B. Dunina, N. V. Kuleshov, and K. V. Yumashev. "Growth, spectroscopic and thermal properties of Nd-doped disordered Ca$_9$(La/Y)(VO$_4$)$_7$ and Ca$_{10}$(Li/K)(VO$_4$)$_7$crystals". In: *J. Lumin.* 137 (2013), pp. 252–258. DOI: 10.1016/j.jlumin.2013.01.013.

[19] S. Sun, Z. Lin, L. Zhang, Y. Huang, and G. Wang. "Growth and spectral properties of a new nonlinear laser crystal of Nd^{3+}:Ca$_9$Y$_{0.5}$(VO$_4$)$_7$". In: *J. Alloys Compd.* 551 (2013), pp. 229–232. DOI: 10.1016/j.jallcom.2012.09.146.

[20] N. Zhuang, X. Liu, Q. Xu, X. Chen, B. Zhao, X. Hu, and J. Chen. "Crystal growth, nonlinear frequency-doubling and spectral characteristic of Nd:Ca$_9$La(VO$_4$)$_7$ crystal". In: *J. Alloys Compd.* 595 (2014), pp. 113–119. DOI: 10.1016/j.jallcom.2014.01.144.

[21] M. B. Kosmyna, B. P. Nazarenko, V. M. Puzikov, A. N. Shekhovtsov, W. Paszkow-
icz, A. Behrooz, P. Romanowski, A. S. Yasukevich, N. V. Kuleshov, M. P. Demesh,
W. Wierzchowski, K. Wieteska, and C. Paulmann. "$Ca_{10}Li(VO_4)_7$:Nd^{3+}, a promis-
ing laser material: Growth, structure and spectral characteristics of a Czochralski-
grown single crystal". In: *J. Cryst. Growth* 445 (2016), pp. 101–107. DOI: 10.1016/
j.jcrysgro.2016.04.002.

[22] Z. Zhang, P. Loiko, H. Wu, X. Mateos, J. M. Serres, H. F. Lin, W. D. Chen, G. Zhang,
L. Z. Zhang, F. Díaz, M. Aguiló, V. Petrov, U. Griebner, Y. C. Wang, E. Vilejshikova,
K. Yumashev, and Z. B. Lin. "Disordered Tm:Ca_9La(VO_4)_7: a novel crystal with
potential for broadband tunable lasing". In: *Opt. Mater. Express* 7.2 (2017), p. 484.
DOI: 10.1364/OME.7.000484.

[23] L. Ivleva, E. Dunaeva, I. Voronina, M. Doroshenko, and A. Papashvili. "$Ca_3(VO_4)_2$:Tm^{3+}
- A new crystalline medium for 2-μm lasers". In: *J. Cryst. Growth* 501.June (2018),
pp. 18–21. DOI: 10.1016/j.jcrysgro.2018.08.019.

[24] L. Ivleva, E. Dunaeva, I. Voronina, M. Doroshenko, A. Papashvili, J. Sulc, J. Kra-
tochvíl, and H. Jelinkova. "Impact of Tm^{3+}/Ho^{3+} co-doping on spectroscopic and
laser properties of $Ca_3(VO_4)_2$ single crystal". In: *J. Cryst. Growth* 513.November
2018 (2019), pp. 10–14. DOI: 10.1016/j.jcrysgro.2019.02.054.

[25] P. N. Hu and G. F. Wang. "Growth and spectral properties of Er^{3+}:$Ca_9La(VO_4)_7$crystal".
In: *Mater. Res. Innov.* 15.1 (2011), pp. 75–77. DOI: 10.1179/143307511X12922272564067.

[26] S. Cao, Y. Ma, C. Quan, W. Zhu, K. Yang, W. Yin, G. Zheng, M. Wu, and Z. Sun.
"Photoluminescence properties of $Ca_9Y(PO_4)_7$ and $Ca_9Y_{0.95}Ln_{0.05}(VO_4)_7$ (Ln^{3+}=Eu^{3+},
Sm^{3+}, Pr^{3+})". In: *J. Alloys Compd.* 487.1-2 (2009), pp. 346–350. DOI: 10.1016/j.
jallcom.2009.07.139.

[27] X. Wu, Y. Huang, L. Shi, and H. J. Seo. "Spectroscopy characteristics of vanadate
$Ca_9Dy(VO_4)_7$ for application of white-light-emitting diodes". In: *Mater. Chem. Phys.*
116.2-3 (2009), pp. 449–452. DOI: 10.1016/j.matchemphys.2009.04.002.

[28] L. Han, Y. Wang, J. Zhang, and Y. Wang. "Enhancement of red emission intensity of
$Ca_9Y(PO_4)_7$:Eu^{3+} phosphor via Bi co-doping for the application to white LEDs".
In: *Mater. Chem. Phys.* 139.1 (2013), pp. 87–91. DOI: 10.1016/j.matchemphys.2012.
12.048.

[29] J. Zhao, C. Guo, J. Yu, and R. Yu. "Spectroscopy properties of Eu^{3+} doped $Ca_9R(VO_4)_7$
(R=Bi, La, Gd and Y) phosphors by sol–gel method". In: *Opt. Laser Technol.* 45.1
(2013), pp. 62–68. DOI: 10.1016/j.optlastec.2012.07.032.

[30] X. Mi, K. Du, K. Huang, P. Zhou, D. Geng, Y. Zhang, M. Shang, and J. Lin. "Synthe-
sis and luminescence of $Ca_9Eu_{1-x}Ln_x(VO_4)_7$ (Ln = Y, La, Gd, Lu) phosphors". In:
Mater. Res. Bull. 60 (2014), pp. 72–78. DOI: 10.1016/j.materresbull.2014.08.017.

[31] M. Dai, K. Qiu, W. Zhang, and Q. Tang. "Synthesis and photoluminescence enhancement of $Ca_9La(VO_4)_7$:Eu^{3+} red phosphors by Mg^{2+} co-doping for white LEDs". In: *J. Mater. Sci. Mater. Electron.* 29.17 (2018), pp. 15052–15059. DOI: 10.1007/s10854-018-9644-5.

[32] M. Dai, K. Qiu, P. Zhang, and W. Zhang. "Synthesis and luminescence properties of orange–red-emitting $Ca_9La(VO_4)_7$:Sm^{3+} phosphors co-doped with alkali metal ions". In: *J. Mater. Sci. Mater. Electron.* 30.10 (2019), pp. 9184–9193. DOI: 10.1007/s10854-019-01247-7.

[33] X. Wu, Y. Huang, and H. J. Seo. "The luminescence spectroscopy and thermal stability of red-emitting phosphor $Ca_9Eu(VO_4)_7$". In: *Ceram. Int.* 37.7 (2011), pp. 2323–2328. DOI: 10.1016/j.ceramint.2011.03.031.

[34] S. K. Sharma, T. Tingberg, I. Carrasco, M. Bettinelli, D. Kuylenstierna, and M. Karlsson. "Photoluminescence properties and fabrication of red-emitting LEDs based on $Ca_9Eu(VO_4)_7$ phosphor". In: *ECS J. Solid State Sci. Technol.* 9.1 (2020), p. 016004. DOI: 10.1149/2.0052001JSS.

[35] M. A. Pogosova, F Azarmi, A. A. Eliseev, and P. E. Kazin. "Dyes and Pigments Eu and Cu co-substituted calcium vanadated The crystal structure, luminescence and color". In: *Dye. Pigment.* 148.6 (2018), pp. 219–223. DOI: 10.1016/j.dyepig.2017.09.017.

[36] H. Ji, Z. Huang, Z. Xia, M. S. Molokeev, V. V. Atuchin, M. Fang, and S. Huang. "New yellow-emitting whitlockite-type structure $Sr_{1.75}Ca_{1.25}(PO_4)_2$:$Eu^{2+}$ phosphor for near-UV pumped white light-emitting devices". In: *Inorg. Chem.* 53.10 (2014), pp. 5129–5135.

[37] L. Li, X. Tang, Z. Wu, Y. Zheng, S. Jiang, X. Tang, G. Xiang, and X. Zhou. "Simultaneously tuning emission color and realizing optical thermometry via efficient $Tb^{3+} \rightarrow Eu^{3+}$ energy transfer in whitlockite-type phosphate multifunctional phosphors". In: *J. Alloys Compd.* 780 (2019), pp. 266–275.

[38] N. Guo, S. Li, J. Chen, J. Li, Y. Zhao, L. Wang, C. Jia, R. Ouyang, and W. Lü. "Photoluminescence properties of whitlockite-type $Ca_9MgK(VO_4)_7$:Eu^{2+},Mn^{2+} phosphor". In: *J. Lumin.* 179 (2016), pp. 328–333. DOI: 10.1016/j.jlumin.2016.07.015.

[39] A. A. Belik, V. A. Morozov, D. V. Deyneko, A. E. Savon, O. V. Baryshnikova, E. S. Zhukovskaya, N. G. Dorbakov, Y. Katsuya, M. Tanaka, S. Y. Stefanovich, J. Hadermann, and B. I. Lazoryak. "Antiferroelectric properties and site occupations of R^{3+} cations in $Ca_9MgR(PO_4)_7$ luminescent host materials". In: *J. Alloys Compd.* 699.2017 (2017), pp. 928–937. DOI: 10.1016/j.jallcom.2016.12.288.

[40] Y. Dikhtyar, D. Spassky, V. Morozov, D. Deyneko, A. Belik, O. Baryshnikova, I. Nikiforov, and B. Lazoryak. "Site occupancy, luminescence and dielectric properties of β-$Ca_3(PO_4)_2$-type $Ca_8ZnLn(PO_4)_7$ host materials". In: *J. Alloys Compd.* 908 (2022), p. 164521. DOI: 10.1016/j.jallcom.2022.164521.

[41] V. Paterlini, A. El Khouri, M. Bettinelli, D. M. Trucchi, and F. Capitelli. "Spectroscopic and structural properties of β-tricalcium phosphates $Ca_9RE(PO_4)_7$ (RE = Nd, Gd, Dy)". In: *Crystals* 11.10 (2021). DOI: 10.3390/cryst11101269.

[42] T. Peters. *Advanced X-Ray Crystallography*. Ed. by K. Rissanen. Vol. 315. Topics in Current Chemistry. Berlin, Heidelberg: Springer Berlin Heidelberg, 2012. DOI: 10.1007/978-3-642-27407-7.

[43] P. Duthil. "Material properties at low temperature". In: *CAS-CERN Accel. Sch. Supercond. Accel. - Proc.* (2015), pp. 77–95. DOI: 10.5170/CERN-2014-005.77. arXiv: 1501.07100.

[44] A. E. Goeta and J. A. K. Howard. "Low temperature single crystal X-ray diffraction: advantages, instrumentation and applications". In: *Chem. Soc. Rev.* 33.8 (2004), p. 490. DOI: 10.1039/b312763j.

[45] S. Chénais, F. Druon, S. Forget, F. Balembois, and P. Georges. "On thermal effects in solid-state lasers: The case of ytterbium-doped materials". In: *Prog. Quantum Electron.* 30.4 (2006), pp. 89–153. DOI: 10.1016/j.pquantelec.2006.12.001.

[46] I. A. Leonidov, L. L. Surat, and O. N. Leonidova. "Whitlockite solid solutions in the $Ca_3(VO_4)_2$-K_3VO_4-$NdVO_4$ system". In: *Russ. J. Inorg. Chem.* 56.11 (2011), pp. 1706–1712. DOI: 10.1134/S0036023611110167.

[47] W. Paszkowicz, A. Shekhovtsov, M. Kosmyna, P. Loiko, E. Vilejshikova, R. Minikayev, P. Romanowski, W. Wierzchowski, K. Wieteska, C. Paulmann, E. Bryleva, K. Belikov, and A. Fitch. "Structure and thermal expansion of $Ca_9Gd(VO_4)_7$: A combined powder-diffraction and dilatometric study of a Czochralski-grown crystal". In: *Nucl. Instrum. Meth. Phys. Res. Sect. B Beam Interact. with Matt Atoms* 411 (2017), pp. 100–111. DOI: 10.1016/j.nimb.2017.07.026.

[48] B. I. Lazoryak, V. A. Morozov, A. A. Belik, S. Y. Stefanovich, V. V. Grebenev, I. A. Leonidov, E. B. Mitberg, S. A. Davydov, O. I. Lebedev, and G. Van Tendeloo. "Ferroelectric phase transition in the whitlockite-type $Ca_9Fe(PO_4)_7$; Crystal structure of the paraelectric phase at 923 K". In: *Solid State Sci.* 6.2 (2004), pp. 185–195. DOI: 10.1016/j.solidstatesciences.2003.12.007.

[49] R. A. Benhamou, A. Bessière, G. Wallez, B. Viana, M. Elaatmani, M. Daoud, and A. Zegzouti. "New insight in the structure–luminescence relationships of $Ca_9Eu(PO_4)_7$". In: *J. Solid State Chem.* 182.8 (2009), pp. 2319–2325. DOI: 10.1016/j.jssc.2009.06.018.

[50] V. A. Morozov, A. A. Belik, S. Y. Stefanovich, V. V. Grebenev, O. I. Lebedev, G. Van Tendeloo, and B. I. Lazoryak. "High-temperature phase transition in the whitlockite-type phosphate $Ca_9In(PO_4)_7$". In: *J. Solid State Chem.* 165.2 (2002), pp. 278–288. DOI: 10.1006/jssc.2001.9521.

[51] A. A. Belik, V. A. Morozov, D. V. Deyneko, A. E. Savon, O. V. Baryshnikova, E. S. Zhukovskaya, N. G. Dorbakov, Y. Katsuya, M. Tanaka, S. Y. Stefanovich, J. Hadermann, and B. I. Lazoryak. "Antiferroelectric properties and site occupations of R^{3+} cations in $Ca_9MgR(PO_4)_7$ luminescent host materials". In: *J. Alloys Compd.* 699.2017 (2017), pp. 928–937. DOI: 10.1016/j.jallcom.2016.12.288.

[52] O. Schrandt and H. Müller-Buschbaum. "K^+ auf einer mit Ca^{2+} unterbesetzten Punktlage in $Ca_3(VO_4)_2$: Ein Beitrag über $KCa_10V_7O_28$ / K^+ at an Deficient Ca^{2+} Point Position in $Ca_3(VO_4)_2$: On $KCa_10V_7O_28$". In: *Zeitschrift für Naturforsch. B* 51.4 (1996), pp. 473–476. DOI: 10.1515/znb-1996-0405.

[53] I. A. Khodasevich, S. V. Voitikov, V. A. Orlovich, M. B. Kosmyna, and A. N. Shekhovtsov. "Raman Spectra of Crystalline Double Calcium Orthovanadates $Ca_{10}M(VO_4)_7$ (M = Li, K, Na) and Their Interpretation Based on Deconvolution Into Voigt Profiles". In: *J. Appl. Spectrosc.* 83.4 (2016), pp. 555–561. DOI: 10.1007/s10812-016-0327-9.

[54] I. S. Voronina, E. E. Dunaeva, A. G. Papashvili, L. D. Iskhakova, M. E. Doroshenko, and L. I. Ivleva. "High-temperature diffusion doping as a method of fabrication of $Ca_3(VO_4)_2$:Mn single crystals". In: *J. Cryst. Growth* 563.February (2021), p. 126104. DOI: 10.1016/j.jcrysgro.2021.126104.

[55] G. M. Kuz'micheva, L. I. Ivleva, I. A. Kaurova, V. A. Lazarenko, and E. V. Khramov. "Effect of cobalt content on point defects and local structure in activated $Ca_3(VO_4)_2$ single-crystal solid solutions". In: *J. Solid State Chem.* 318 (2023), p. 123776.

[56] B. D. Cullity. *Elements of X-ray Diffraction*. Addison-Wesley Publishing, 1956.

[57] C. Kittel. *Introduction to solid state physics*. Vol. 6. 1. 1957, p. 83.

[58] E. Prince. *Mathematical techniques in crystallography and materials science*. Springer Science & Business Media, 2004.

[59] N. W. Ashcroft and N. D. Mermin. *Solid state physics*. Cengage Learning, 2022.

[60] W. H. Bragg and W. L. Bragg. "The reflection of X-rays by crystals". In: *Proc. R. Soc. London. Ser. A, Contain. Pap. a Math. Phys. Character* 88.605 (1913), pp. 428–438.

[61] F. Peyrin. "Investigation of bone with synchrotron radiation imaging: from micro to nano". In: *Osteoporos. Int.* 20.6 (2009), pp. 1057–1063. DOI: 10.1007/s00198-009-0855-8.

[62] H. Wiedemann. *Partide Accelerator Physics I & II*. 1. 2003, p. 952. arXiv: arXiv:1011.1669v3.

[63] S. Mobilio, F. Boscherini, and C. Meneghini. *Synchrotron Radiation*. Ed. by S. Mobilio, F. Boscherini, and C. Meneghini. Berlin, Heidelberg: Springer Berlin Heidelberg, 2015, pp. 1–799. DOI: 10.1007/978-3-642-55315-8.

[64] P. Willmott. *An introduction to synchrotron radiation: techniques and applications*. John Wiley & Sons, 2019.

[65] R. E. Dinnebier and S. J. L. Billinge. *Powder diffraction: theory and practice*. Royal society of chemistry, 2008.

[66] W. Paszkowicz. "Application of a powder diffractometer equipped with a strip detector and Johansson monochromator to phase analysis and structure refinement". In: *Nucl. Instruments Methods Phys. Res. Sect. A Accel. Spectrometers, Detect. Assoc. Equip.* 551.1 (2005), pp. 162–177. DOI: 10.1016/j.nima.2005.07.068.

[67] H. M. Rietveld. "A profile refinement method for nuclear and magnetic structures". In: *J. Appl. Crystallogr.* 2.2 (1969), pp. 65–71. DOI: 10.1107/S0021889869006558.

[68] B. O. Loopstra and H. M. Rietveld. "The structure of some alkaline-earth metal uranates". In: *Acta Crystallogr. Sect. B Struct. Crystallogr. Cryst. Chem.* 25.4 (1969), pp. 787–791. DOI: 10.1107/S0567740869002974.

[69] Y. Fei. "Thermal Expansion". In: *Miner. Phys. Crystallogr. a Handb. Phys. Constants*. Ed. by T. J. Ahrens. Vol. 2. American Geophysical Union, 1995, pp. 29–44. DOI: 10.1029/RF002p0029.

[70] M. Born, K. Huang, and M Lax. "Dynamical theory of crystal lattices". In: *Am. J. Phys.* 23.7 (1955), p. 474.

[71] D. C. Wallace. "Thermodynamics of crystals". In: *Am. J. Phys.* 40.11 (1972), pp. 1718–1719.

[72] L. Vočadlo, K. S. Knight, G. D. Price, and I. G. Wood. "Thermal expansion and crystal structure of FeSi between 4 and 1173 K determined by time-of-flight neutron powder diffraction". In: *Phys. Chem. Miner.* 29.2 (2002), pp. 132–139. DOI: 10.1007/s002690100202.

[73] A. M. Glass, S. C. Abrahams, A. A. Ballman, and G. Loiacono. "Calcium orthovanadate, $Ca_3(VO_4)_2$-a new high-temperature ferroelectric". In: *Ferroelectrics* 17.1 (1977), pp. 579–582. DOI: 10.1080/00150197808236782.

[74] P. A. Popov, S. A. Skrobov, A. V. Matovnikov, M. B. Kosmyna, V. M. Puzikov, B. P. Nazarenko, A. N. Shekhovtsov, A. Behrooz, W. Paszkowicz, I. A. Khodasevich, N. N. Shereshovets, S. V. Voitikov, and V. A. Orlovich. "Thermal Conductivity Investigation of $Ca_9RE(VO_4)_7$ (RE = La, Nd, Gd) and $Ca_{10}M(VO_4)_7$ (M = Li, Na, K) Single Crystals". In: *Int. J. Thermophys.* 38.1 (2017), pp. 1–13. DOI: 10.1007/s10765-016-2135-0.

[75] L. Andrade, D. Reyes Ardila, J. Andreeta, and M. Siu Li. "Optical properties of Nd^{3+}-doped $Ca_3(VO_4)_2$ single crystal fiber". In: *Opt. Mater. (Amst).* 22.4 (2003), pp. 369–375. DOI: 10.1016/S0925-3467(02)00371-3.

[76] N. G. Dorbakov, O. V. Baryshnikova, V. A. Morozov, A. A. Belik, Y. Katsuya, M. Tanaka, S. Y. Stefanovich, and B. I. Lazoryak. "Tuning of nonlinear optical and ferroelectric properties via the cationic composition of $Ca_{9.5-1.5x}Bi_xCd(VO_4)_7$ solid solutions". In: *Mater. Des.* 116 (2017), pp. 515–523. DOI: 10.1016/j.matdes.2016.11.107.

[77] N. G. Dorbakov, V. V. Titkov, S. Y. Stefanovich, O. V. Baryshnikova, V. A. Morozov, A. A. Belik, and B. I. Lazoryak. "Barium-induced effects on structure and properties of β-$Ca_3(PO_4)_2$-type $Ca_9Bi(VO_4)_7$". In: *J. Alloys Compd.* 793 (2019), pp. 56–64. DOI: 10.1016/j.jallcom.2019.03.365.

[78] J. Rodríguez-Carvajal. "Recent advances in magnetic structure determination by neutron powder diffraction". In: *Phys. B Condens. Matter* 192.1-2 (1993), pp. 55–69.

[79] A. N. Fitch. "The high resolution powder diffraction beam line at ESRF". In: *J. Res. Natl. Inst. Stand. Technol.* 109.1 (2004), p. 133.

[80] Y.-P. Tong, G.-T. Luo, Z. Jin, and Y.-W. Lin. "Synthesis, structure, and theoretical investigations of an alkaline earth vanadate oxide compound (Ca4V4O14): electronic, optical, and chemical bond properties". In: *Aust. J. Chem.* 64.7 (2011), pp. 973–977.

[81] K. M. Kosyl, W. Paszkowicz, R. Minikayev, M. Berkowski, M. Czech, A. Reszka, and L. Kilanski. "Thermal expansion of calcium cobalt vanadate garnet,$Ca_{2.5}Co_2V_3O_{12}$". In: *J. Alloys Compd.* 779 (2019), pp. 863–869. DOI: 10.1016/j.jallcom.2018.11.258.

[82] N. Wang, Z. He, M. Cui, W. Guo, S. Zhang, M. Yang, and Y. Tang. "Syntheses, structure and magnetic properties of two vanadate garnets $Ca_5M_4V_6O_{24}$ (M=Co, Ni)". In: *J. Solid State Chem.* 228 (2015), pp. 245–249. DOI: 10.1016/j.jssc.2015.05.004.

[83] R. D. Shannon. "Revised effective ionic radii and systematic studies of interatomic distances in halides and chalcogenides". In: *Acta Crystallogr. Sect. A* 32.5 (1976), pp. 751–767. DOI: 10.1107/S0567739476001551.

[84] A. A. Belik, O. V. Yanov, and B. I. Lazoryak. "Synthesis and crystal structure of $Ca_9Cu_{1.5}(PO_4)_7$ and reinvestigation of $Ca_{9.5}Cu(PO_4)_7$". In: *Mater. Res. Bull.* 36 (2001), pp. 1863–1871.

[85] S. Kannan, F. Goetz-Neunhoeffer, J. Neubauer, and J. M. Ferreira. "Synthesis and structure refinement of zinc-doped β-Tricalcium phosphate powders". In: *J. Am. Ceram. Soc.* 92.7 (2009), pp. 1592–1595. DOI: 10.1111/j.1551-2916.2009.03093.x.

[86] R. Enderle, F. Götz-Neunhoeffer, M. Göbbels, F. Müller, and P. Greil. "Influence of magnesium doping on the phase transformation temperature of β-TCP ceramics examined by Rietveld refinement". In: *Biomaterials* 26.17 (2005), pp. 3379–3384. DOI: 10.1016/j.biomaterials.2004.09.017.

[87] N. G. Dorbakov, V. V. Grebenev, V. V. Titkov, E. S. Zhukovskaya, S. Y. Stefanovich, O. V. Baryshnikova, D. V. Deyneko, V. A. Morozov, A. A. Belik, and B. I. Lazoryak. "Influence of magnesium on dielectric properties of $Ca_{9-x}Mg_xBi(VO_4)_7$ ceramics". In: *J. Am. Ceram. Soc.* 101.9 (2018), pp. 4011–4022. DOI: 10.1111/jace.15545.

[88] A. Bessière, A. Lecointre, R. A. Benhamou, E. Suard, G. Wallez, and B. Viana. "How to induce red persistent luminescence in biocompatible $Ca_3(PO_4)_2$". In: *J. Mater. Chem. C* 1.6 (2013), pp. 1252–1259. DOI: 10.1039/C2TC00138A.

[89] A. A. Belik, V. A. Morozov, S. S. Khasanov, and B. I. Lazoryak. "Crystal structures of new triple $Ca_9CoM(PO_4)_7$ (M = Li, Na, K) phosphates". In: *Mater. Res. Bull.* 34.6 (1999), pp. 883–893. DOI: 10.1016/S0025-5408(99)00087-2.

[90] A. Altomare, R. Rizzi, M. Rossi, A. El Khouri, M. Elaatmani, V. Paterlini, G. Della Ventura, and F. Capitelli. "New $Ca_{2.90}(Me^{2+})_{0.10}(PO_4)_2$ β-tricalcium phosphates with Me^{2+}= Mn, Ni, Cu: Synthesis, crystal-chemistry, and luminescence properties". In: *Crystals* 9.6 (2019), p. 288.

[91] T. Debroise, E. Colombo, G. Belletti, J. Vekeman, Y. Su, R. Papoular, N. S. Hwang, D. Bazin, M. Daudon, P. Quaino, and F. Tielens. "One step further in the elucidation of the crystallographic structure of whitlockite". In: *Cryst. Growth Des.* 20.4 (2020), pp. 2553–2561. DOI: 10.1021/acs.cgd.9b01679.

[92] I. Mayer, S. Cohen, S. Gdalya, O. Burghaus, and D. Reinen. "Crystal structure and EPR study of Mn-doped β-tricalcium phosphate". In: *Mater. Res. Bull.* 43.2 (2008), pp. 447–452. DOI: 10.1016/j.materresbull.2007.02.031.

[93] I. Mayer, F. J. G. Cuisinier, I. Popov, Y. Schleich, S. Gdalya, O. Burghaus, and D. Reinen. "Phase Relations Between β-Tricalcium Phosphate and Hydroxyapatite with Manganese(II): Structural and Spectroscopic Properties". In: *Eur. J. Inorg. Chem.* 2006.7 (2006), pp. 1460–1465. DOI: 10.1002/ejic.200501009.

[94] A. A. Belik, V. A. Morozov, R. N. Kotov, S. S. Khasanov, and B. I. Lazoryak. "Crystal structure of double vanadates $Ca_9R(VO_4)_7$. II. R = Tb, Dy, Ho, and Y". In: *Crystallogr. Rep* 45.3 (2000), pp. 389–394. DOI: 10.1134/1.171204.

[95] A. A. Belik, V. A. Morozov, S. V. Grechkin, S. S. Khasanov, B. I. Lazoryak, L. O. Dmitrienko, V. A. Morozov, S. S. Khasanov, and B. I. Lazoryak. "Crystal structures of double vanadates, $Ca_9R(VO_4)_7$. III. R = Nd, Sm, Gd, or Ce". In: *Kristallografiya* 45.6 (2000), pp. 976–981. DOI: 10.1134/1.1312910.

[96] A. Altomare, N. Corriero, C. Cuocci, A. Falcicchio, A. Moliterni, and R. Rizzi. "OChemDb: The free online open chemistry database portal for searching and analyzing crystal structure information". In: *J. Appl. Crystallogr.* 51 (2018), pp. 1229–1236. DOI: 10.1107/S1600576718008166.

[97] K. Kosyl. "Structure and disorder in rare earth borates $Ca_3RE_2(BO_3)_4$: diffraction studies under ambient conditions and as a function of temperature". PhD thesis. Polish academy of sciences, 2022.

[98] K. M. Kosyl, W. Paszkowicz, A. N. Shekhovtsov, M. B. Kosmyna, J. Antonowicz, A. Olczak, and A. N. Fitch. "Variation of cation distribution with temperature and its consequences on thermal expansion for Ca 3 Eu 2 (BO 3) 4". In: *Acta Crystallogr. Sect. B Struct. Sci. Cryst. Eng. Mater.* 76.4 (2020), pp. 554–562. DOI: 10.1107/S2052520620006757.

[99] Z. Sun, B. Sun, X. Zhang, D. Wen, and P. Dai. "Superb thermal stability purple-blue phosphor through synergistic effect of emission compensation and nonradiative transition restriction of Eu^{2+}". In: *Mater. Today Chem.* 24 (2022), p. 100877. DOI: 10.1016/j.mtchem.2022.100877.

[100] X. Pan, L. Mei, Y. Zhuang, T. Seto, Y. Wang, M. Plyaskin, W. Xi, C. Li, Q. Guo, and L. Liao. "Anti-Defect engineering toward high luminescent efficiency in whitlockite phosphors". In: *Chem. Eng. J.* 434.January (2022), p. 134652. DOI: 10.1016/j.cej.2022.134652.

[101] N. Khan, V. A. Morozov, S. S. Khasanov, and B. I. Lazoryak. "Synthesis and crystal structure of calcium copper phosphate, $s-Ca_{19}Cu_2(PO_4)_14$". In: *Mater. Res. Bull.* 32.9 (1997), pp. 1211–1220. DOI: 10.1016/S0025-5408(97)00098-6.

[102] F. Junmei, W. Guofu, and Y. Fangli. "Growth and characterization of new laser crystal $Nd^{3+}:Ca_{2.85}Gd_{0.1}(VO_4)_2$". In: *Journal of Rare Earths* 30.4 (2012), pp. 335–338.

[103] X Chen, N. Zhuang, X. Hu, F. Zhuang, and J. Chen. "Growth and spectral properties of self-frequency doubling crystal, $Ca_{9.03}Na_{1.08}La_{0.62}(VO_4)_7:Nd$". In: *Applied Physics B* 88 (2007), pp. 449–455.